Monthly Notices
of the
ROYAL ASTRONOMICAL SOCIETY

MNRAS **494,** 3828–3860 (2020)
Advance Access publication 2020 April 2

doi:10.1093/mnras/staa769

# An ALMA survey of the SCUBA-2 CLS UDS field: physical properties of 707 sub-millimetre galaxies

U. Dudzevičiūtė ,[1]★ Ian Smail ,[1] A. M. Swinbank ,[1] S. M. Stach,[1] O. Almaini ,[2] E. da Cunha,[3,4,5] Fang Xia An,[6] V. Arumugam,[7] J. Birkin,[1] A. W. Blain,[8] S. C. Chapman,[9] C.-C. Chen ,[10] C. J. Conselice,[2] K. E. K. Coppin,[11] J. S. Dunlop,[12] D. Farrah,[13,14] J. E. Geach ,[11] B. Gullberg ,[1] W. G. Hartley,[15] J. A. Hodge,[16] R. J. Ivison ,[10,12] D. T. Maltby,[2] D. Scott,[17] C. J. Simpson,[18] J. M. Simpson,[1] A. P. Thomson,[19] F. Walter,[20] J. L. Wardlow,[21] A. Weiss[22] and P. van der Werf[16]

*Affiliations are listed at the end of the paper*

Accepted 2020 March 11. Received 2020 March 11; in original form 2019 September 30

## ABSTRACT

We analyse the physical properties of a large, homogeneously selected sample of ALMA-located sub-millimetre galaxies (SMGs). This survey, AS2UDS, identified 707 SMGs across the $\sim$1 deg$^2$ field, including $\sim$17 per cent, which are undetected at $K \gtrsim 25.7$ mag. We interpret their ultraviolet-to-radio data using MAGPHYS and determine a median redshift of $z = 2.61 \pm 0.08$ ($1\sigma$ range of $z = 1.8$–$3.4$) with just $\sim$6 per cent at $z > 4$. Our survey provides a sample of massive dusty galaxies at $z \gtrsim 1$, with median dust and stellar masses of $M_{\rm d} = (6.8 \pm 0.3) \times 10^8\,{\rm M}_\odot$ (thus, gas masses of $\sim 10^{11}\,{\rm M}_\odot$) and $M_* = (1.26 \pm 0.05) \times 10^{11}\,{\rm M}_\odot$. We find no evolution in dust temperature at a constant far-infrared luminosity across $z \sim 1.5$–$4$. The gas mass function of our sample increases to $z \sim 2$–$3$ and then declines at $z > 3$. The space density and masses of SMGs suggest that almost all galaxies with $M_* \gtrsim 3 \times 10^{11}\,{\rm M}_\odot$ have passed through an SMG-like phase. The redshift distribution is well fit by a model combining evolution of the gas fraction in haloes with the growth of halo mass past a critical threshold of $M_{\rm h} \sim 6 \times 10^{12}\,{\rm M}_\odot$, thus SMGs may represent the highly efficient collapse of gas-rich massive haloes. We show that SMGs are broadly consistent with simple homologous systems in the far-infrared, consistent with a centrally illuminated starburst. Our study provides strong support for an evolutionary link between the active, gas-rich SMG population at $z > 1$ and the formation of massive, bulge-dominated galaxies across the history of the Universe.

**Key words:** galaxies: high-redshift – galaxies: starburst – submillimetre: galaxies.

## 1 INTRODUCTION

Analysis of the relative brightness of the extragalactic background in the ultraviolet (UV)/optical and far-infrared/sub-millimetre suggest that around half of all of the star formation that has occurred over the history of the Universe was obscured by dust (e.g. Puget et al. 1996). This far-infrared/sub-millimetre emission is expected to primarily comprise the reprocessing of UV emission from young, massive stars by dust grains in the interstellar medium (ISM) of distant galaxies, which is re-emitted in the form of far-infrared/sub-millimetre photons as the grains cool. Understanding the nature, origin, and evolution of this dust-obscured activity in galaxies is therefore crucial for obtaining a complete understanding of their formation and growth (see Casey, Narayanan & Cooray 2014 for a review).

In the local Universe, the most dust-obscured galaxies are also some of the most actively star-forming systems: ultraluminous infrared galaxies (ULIRGs; Sanders & Mirabel 1996) with star-formation rates (SFR) of $\gtrsim 100\,{\rm M}_\odot\,{\rm yr}^{-1}$. These radiate $\gtrsim$95 per cent of their bolometric luminosity in the mid-infrared/far-infrared as a result of strong dust obscuration of their star-forming regions. These galaxies have relatively faint luminosities in UV/optical wavebands, but far-infrared luminosities of $L_{\rm IR} \geq 10^{12}\,L_\odot$ and hence they are most easily identified locally through surveys in the far-infrared waveband (e.g. *IRAS* 60 $\mu$m). It has been suggested that the high star-formation rates of ULIRGs arise from the concentration of massive molecular gas reservoirs (and thus, high ISM densities and strong dust absorption) in galaxies that are

★ E-mail: ugne.dudzeviciute2@durham.ac.uk

undergoing tidal interactions as a result of mergers (Sanders et al. 1988).

The far-infrared ($\gtrsim$ 100 $\mu$m) spectral energy distribution (SED) of the dust-reprocessed emission from ULIRGs can be roughly approximated by a modified blackbody. The rapid decline in the brightness of the source at wavelengths beyond the SED peak on the Rayleigh–Jeans tail creates a strong negative *k*-correction for observations of this population at high redshifts (Franceschini et al. 1991; Blain & Longair 1993). Hence, a dusty galaxy with a fixed far-infrared luminosity and temperature will have an almost constant apparent flux density in the sub-millimetre waveband (which traces rest-frame emission beyond the redshifted peak of the SED) from $z \sim 1$ to 7 (see Casey, Narayanan & Cooray 2014). As a result, surveys in the sub-millimetre waveband, in principle, allow us to construct luminosity-limited samples of obscured, star-forming galaxies over a very wide range of cosmic time, spanning the expected peak activity in galaxy formation at $z \gtrsim$ 1–3 (e.g. Chapman et al. 2005; Casey et al. 2012; Weiß et al. 2013; Simpson et al. 2014; Strandet et al. 2016; Brisbin et al. 2017).

Sub-millimetre galaxies (SMGs) with 850-$\mu$m flux densities of $S_{850} \gtrsim$ 1–10 mJy were first uncovered over 20 years ago using the atmospheric window around 850 $\mu$m with the SCUBA instrument on the James Clerk Maxwell Telescope (JCMT) (Smail, Ivison & Blain 1997; Barger et al. 1998; Hughes et al. 1998; Eales et al. 1999). Subsequent studies have suggested they represent a population of particularly dusty, high infrared luminosity systems ($>10^{12}\,L_{\odot}$) that are typically found at high redshift ($z \sim$ 1–4). They have large gas reservoirs (Frayer et al. 1998; Greve et al. 2005; Bothwell et al. 2013), stellar masses of the order of $10^{11}\,M_{\odot}$ and can reach very high star-formation rates up to (and in some cases in excess of) $\sim$1,000 $M_{\odot}\,yr^{-1}$. SMGs have some observational properties that appear similar to those of local ULIRGs, such as high far-infrared luminosities and star-formation rates; however, their space densities are a factor of $\sim$1,000 times higher than the comparably luminous local population (e.g. Smail et al. 1997; Chapman et al. 2005; Simpson et al. 2014). Thus, in contrast to the local Universe, these luminous systems are a non-negligible component of the star-forming population at high redshift. Very wide-field surveys with the Spectral and Photometric Imaging Receiver (SPIRE) instrument on *Herschel* have traced this dusty luminous population, using very large samples, to lower redshifts and lower far-infrared luminosities (e.g. Bourne et al. 2016). However, the modest angular resolution of *Herschel*/SPIRE and resulting bright confusion limit, at longer far-infrared wavelengths limits its ability to select all but the very brightest (unlensed) sources at the era of peak activity in the obscured population at $z \gtrsim$ 1–2 (Symeonidis, Page & Seymour 2011). Such low-resolution far-infrared-selected samples are also more challenging to analyse owing to the ambiguities in source identification that results from a ground-based follow-up to locate counterparts, which is necessarily undertaken at longer wavelengths than the original far-infrared selection.

With such high star-formation rates, SMGs can rapidly increase their (apparently already significant) stellar masses on a timescale of just $\sim$100 Myr (e.g. Bothwell et al. 2013). High star-formation rates and high stellar masses of this population, along with the high metallicities suggested by the significant dust content, have therefore been used to argue that they may be an important phase in the formation of the stellar content of the most massive galaxies in the Universe, being the progenitors of local luminous spheroids and elliptical galaxies (Lilly et al. 1999; Chapman et al. 2005; Simpson et al. 2014). There have also been suggestions of an evolutionary link with quasi-stellar objects (QSOs) (e.g. Swinbank et al. 2006; Wall, Pope & Scott 2008; Hickox et al. 2012; Simpson et al. 2012) due to the similarities in their redshift distributions. More recently these systems have been potentially linked to the formation of compact quiescent galaxies seen at $z \sim$ 1–2 (e.g. Whitaker et al. 2012; Simpson et al. 2014; Toft et al. 2014) as a result of their short gas depletion timescales. This connection has been strengthened by recent observations in the rest-frame far-infrared that suggest very compact extents of the star-forming regions (Toft et al. 2014; Ikarashi et al. 2015; Simpson et al. 2015a; Gullberg et al. 2019). Thus several lines of evidence suggest that SMGs are an important element for constraining the models of massive galaxy formation and evolution.

The pace of progress of our understanding of the nature and properties of the SMG population has accelerated in the last five years, owing to the commissioning of the Atacama Large Millimetre/Submillimetre Telescope (ALMA). ALMA has enabled high-sensitivity ($\ll$1-mJy rms) and high-angular resolution [$\lesssim$1 arcsec full width at half-maximum (FWHM)] observations in the sub-millimetre wavebands of samples of dust-obscured galaxies at high redshifts, including SMGs. In the first few years of operations, ALMA has been used to undertake a number of typically deep continuum surveys of small contiguous fields (Hatsukade et al. 2016; Walter et al. 2016; Dunlop et al. 2017; Franco et al. 2018; Hatsukade et al. 2018; Muñoz Arancibia et al. 2018; Umehata et al. 2018), with areas of tens of arcmin$^2$ (including lensing clusters and protocluster regions). These small field studies typically contain sources at flux limits of $S_{870} \simeq$ 0.1–1 mJy [corresponding to star-formation rates of $\sim$10–100 $M_{\odot}\,yr^{-1}$ or farr-infrared luminosities of $\sim(0.5–5) \times 10^{11}\,L_{\odot}$] and so provide a valuable link between the bright SMGs seen in the panoramic single-dish surveys and the populations of typically less actively star-forming galaxies studied in UV/optical-selected surveys. However, owing to their small areas they do not contain more than a few examples of the brighter SMGs. To efficiently study the brighter sources requires targeted follow-up of sources from panoramic single-dish surveys. Hence, ALMA has also been employed to study the dust continuum emission from samples of $\lesssim$100 SMGs selected from single-dish surveys at 870 or 1100 $\mu$m (e.g. Hodge et al. 2013; Brisbin et al. 2017; Cowie et al. 2018). The primary goal of these studies has been to first precisely locate the galaxy or galaxies responsible for the sub-millimetre emission in the (low-resolution) single-dish source and to then understand their properties (e.g. Simpson et al. 2014; Brisbin et al. 2017).

The first ALMA follow-up of a single-dish sub-millimetre survey was the ALESS survey (Hodge et al. 2013; Karim et al. 2013) of a sample of 122 sources with $S_{870} \geq$ 3.5 mJy selected from the 0.25 deg$^2$ LABOCA 870-$\mu$m map of the Extended Chandra Deep Field South (ECDFS) by Weiß et al. (2009). The multiwavelength properties of 99 SMGs from the robust main sample were analysed using the MAGPHYS SED modelling code by da Cunha et al. (2015) (see also the MAGPHYS analysis of a similar-sized sample of 1.1-mm selected SMGs in the COSMOS field by Miettinen et al. 2017). This approach of using a single consistent approach to model the UV/optical and far-infrared emission provides several significant benefits for these dusty and typically very faint galaxies, over previous approaches of independently modelling the UV/optical and far-infrared emission (e.g. Clements et al. 2008; Cowie et al. 2018). In particular, the use in MAGPHYS of an approximate energy balance formulation between the energy absorbed by dust from the UV/optical and that re-emitted in the far-infrared provides more reliable constraints on the photometric redshifts for the SMGs (e.g. da Cunha et al. 2015; Miettinen et al. 2017). This is particularly critical in order to derive complete and unbiased redshift distributions for flux-limited samples of SMGs, as $\sim$20 per

cent of SMGs are typically too faint to be detected at wavelengths shortward of the near-infrared (e.g. Simpson et al. 2014; Franco et al. 2018) and hence are frequently missing from such analyses. The energy balance coupling is also expected to improve the derivation of physical properties of these optically faint systems, such as stellar masses and dust attenuation, which are otherwise typically poorly constrained (Dunlop 2011; Hainline et al. 2011).

While the studies by da Cunha et al. (2015) and Miettinen et al. (2017) have provided improved constraints on the physical parameters of samples of ∼100 SMGs, the modest size of these samples does not allow for robust analysis of the evolutionary trends in these parameters within the population (da Cunha et al. 2015), or to study subsets of SMGs, such as the highest redshift examples (Coppin et al. 2009; Swinbank et al. 2012) or those that show signatures of both star formation and active galactic nucleus (AGN) activity (Wang et al. 2013). To fully characterize the population of SMGs and interpret their role in the overall galaxy evolution requires a large, homogeneously selected sample with precisely located sub-millimetre emission from sub-/millimetre interferometers. We have therefore just completed an ALMA study of a complete sample of 716 single-dish sources selected from the SCUBA-2 Cosmology Legacy Survey (S2CLS) 850-$\mu$m map of the UKIRT Infrared Deep Sky Survey (UKIDSS) UDS field (S2CLS is presented in Geach et al. 2017). This targetted ALMA study – called AS2UDS (Stach et al. 2019) – used sensitive 870-$\mu$m continuum observations obtained in Cycles 1, 3, 4, and 5 to precisely locate (to within $\ll 0.1$ arcsec) 707 SMGs across the ∼0.9 deg$^2$ S2CLS–UDS field. AS2UDS provides the largest homogeneously selected sample of ALMA-identified SMGs currently available, ∼6 times larger than the largest existing ALMA surveys (Hodge et al. 2013; Miettinen et al. 2017).

In this paper, we construct the UV-to-radio SEDs of our sample of 707 ALMA-identified SMGs from the AS2UDS survey using a physically motivated model, MAGPHYS (da Cunha et al. 2015; Battisti et al. 2019). We use the model to interpret the SEDs and so investigate the rest-frame optical (stellar) and infrared (dust) properties of the SMGs. This sample allows us to both improve the statistics to search for trends within the population (e.g. Stach et al. 2018, 2019) and to understand the influence of selection biases on our results and the conclusions of previous studies. With a statistically well constrained and complete understanding of their redshift distribution and physical properties, we are able to address what place the SMG phase takes in the evolution of massive galaxies. Through our paper, we compare our results to samples of both local ULIRGs and near-infrared selected high-redshift field galaxies, which we analyse in a consistent manner to our SMG sample to avoid any systematic uncertainties affecting our conclusions.

Our paper is structured as follows. In Section 2, we describe the multiwavelength observations of the AS2UDS SMGs. In Section 3, we describe the SED fitting procedure using MAGPHYS and test its robustness. We present the results including the redshift distribution, multiwavelength properties and evolutionary trends of the whole AS2UDS SMG population in Section 4. We discuss the implications of our results in Section 5 and present our conclusions in Section 6. Unless stated otherwise, we use ΛCDM cosmology with $H_0 = 70\,\mathrm{km\,s^{-1}\,Mpc^{-1}}$, $\Omega_\Lambda = 0.7$, and $\Omega_\mathrm{m} = 0.3$. The AB photometric magnitude system is used throughout.

## 2 OBSERVATIONS AND SAMPLE SELECTION

In this section, we describe the multiwavelength photometric data, we use to derive the SED from the UV-to-radio wavelengths for each galaxy in our sample. From these SEDs, we aim to derive the physical properties of each SMG (such as their photometric redshift, star-formation rate, stellar, dust, and gas masses). To aid the interpretation of our results, we also exploit the ∼300,000 *K*-selected field galaxies in the UKIDSS UDS (Almaini et al. in preparation). We measure the photometry and SEDs for the field galaxies and SMGs in a consistent manner and describe the sources of these data and any new photometric measurements below.

### 2.1 ALMA

A detailed description of the ALMA observations, data reduction and construction of the catalogue for the SMGs in our sample can be found in Stach et al. (2019). Briefly, the AS2UDS (defined in Section 1) comprises an ALMA follow-up survey of a complete sample of 716 SCUBA-2 sources that are detected at $> 4\sigma$ ($S_{850} \geq 3.6$ mJy) in the S2CLS map of the UKIDSS UDS field (Geach et al. 2017). The S2CLS map of the UDS covers an area of 0.96 deg$^2$ with a noise level below 1.3 mJy and a median depth of $\sigma_{850} = 0.88\,\mathrm{mJy\,beam^{-1}}$. All 716 SCUBA-2 sources detected in the map were observed in ALMA Band 7 (344 GHz or 870 $\mu$m) between Cycles 1, 3, 4, and 5 (a pilot study of 27 of the brightest sources observed in Cycle 1 is discussed in Simpson et al. 2015b, 2017). Due to configuration changes between cycles, the spatial resolution of the data varies in the range 0.15–0.5 arcsec FWHM, although all of the maps are tapered to 0.5 arcsec FWHM for detection purposes (see Stach et al. 2019, for details). The final catalogue contains 708 individual ALMA-identified SMGs spanning $S_{870} = 0.6$–$13.6$ mJy ($>4.3\sigma$) corresponding to a 2 per cent false-positive rate. We remove one bright, strongly lensed source (Ikarashi et al. 2011) from our analysis and the remaining 707 ALMA-identified SMGs are the focus of this study of the physical properties.

### 2.2 Optical and near-/mid-infrared imaging

#### 2.2.1 *Optical* U-*band to* K-*band photometry*

At the typical redshift of SMGs, $z \sim 2.5$ (e.g. Chapman et al. 2005; Simpson et al. 2014; Brisbin et al. 2017; Danielson et al. 2017), the observed optical to mid-infrared corresponds to the rest-frame UV/optical/near-IR, which is dominated by the (dust-attenuated) stellar continuum emission, emission lines, and any possible AGN emission. The rest-frame UV/optical/near-IR also includes spectral features that are important for deriving photometric redshift, in particular, the photometric redshifts have sensitivity to the Lyman break, Balmer and/or 4000Å break and, the (rest-frame) 1.6-$\mu$m stellar 'bump'.

To measure the optical/near-infrared photometry for the galaxies in the UDS, we exploit the panchromatic photometric coverage of this field. In particular, we utilize the UKIDSS (Lawrence et al. 2007) UDS data release 11 (UKIDSS DR11), which is a *K*-band selected photometric catalogue (Almaini et al., in preparation) covering an area of 0.8 deg$^2$ with a $3\sigma$ point-source depth of $K = 25.7$ mag (all photometry in this section is measured in 2 arcsec diameter apertures and has been aperture corrected, unless otherwise stated). This *K*-band selected catalogue has 296,007 sources, of which more than 90 per cent are flagged as galaxies with reliable *K*-band photometry. For any subsequent analysis, we restrict our analysis to 205 910 sources that have no contamination flags. The UKIDSS survey imaged the UDS field with the UKIRT WFCAM camera in the *K*, *H*, and *J* bands and the DR11 catalogue also

includes the matched photometry in the $J$ and $H$ bands to $3\sigma$ depths of $J = 26.0$ and $H = 25.5$.

In addition, the $Y$-band photometry was also obtained from the VISTA/VIDEO survey, which has a $3\sigma$ depth of 25.1 mag and the $BVRi'z'$-band photometry was obtained from *Subaru*/Suprimecam imaging, which has $3\sigma$ depths of 28.2, 27.6, 27.5, 27.5, and 26.4 mag, respectively. Finally, the $U$-band photometry of the UDS field from the Canada–France–Hawaii Telescope/Megacam survey is also included in the DR11 catalogue. This $U$-band imaging reaches a $3\sigma$ point-source depth of 27.1 mag.

To derive the photometry of the ALMA SMGs in the optical/near-infrared, first, we align the astrometry between the UKIDSS DR11 catalogue with the ALMA astrometry by matching the positions of the ALMA SMGs to the $K$-band catalogue, identifying and removing an offset of $\Delta$RA $= 0.1$ arcsec and $\Delta$Dec. $= 0.1$ arcsec in the $K$ band. We find that 634/707 SMGs lie within the deep regions of the $K$-band image, after excluding regions masked due to noisy edges, artefacts, and bright stars. The two catalogues are then matched using a radius of 0.6 arcsec (which has a false match rate of 3.5 per cent; see An et al. 2018 for details). This results in 526/634 SMGs with $K$-band detections (83 per cent). We note that 43 of these sources are within a $K$-band region flagged with possibly contaminated photometry; however, the inclusion of these sources in our analysis does not change any of our conclusions of this study, thus we retain then and flag then in our catalogue.

Our detection fraction is comparable to, but slightly higher than, the fraction identified in smaller samples of SMGs in other fields, which is likely due to the very deep near-IR coverage available in the UDS. For example, in the ALMA survey of the ECDFS, ALESS – Simpson et al. (2014) show that 61/99 (60 per cent) of the ALMA SMGs have $K$-band counterparts to a limit of $K = 24.4$. This is significantly lower than the detection rate in our UDS survey, although cutting our UDS catalogue at the same $K$-band limit as the ECDFS results in a detected fraction of 68 per cent. Similarly, 65 per cent of the ALMA SMGs in the CDFS from Cowie et al. (2018) (which have a median 870-$\mu$m flux of $S_{870} = 1.8$ mJy) are brighter than $K = 24.4$. Finally, Brisbin et al. (2017) identify optical counterparts to 97/152 (64 per cent) of ALMA-identified SMGs from a Band 6 (1.2 mm) survey of AzTEC sources using the public COSMOS2015 catalogue (Laigle et al. 2016), which is equivalent to $K \lesssim 24.7$, for the deepest parts. Thus, our detection rate of 83 per cent of ALMA SMGs with $K$-band counterparts is consistent with previous surveys but also demonstrates that even with extremely deep near-infrared imaging, a significant number (17 per cent or 108 galaxies) are faint or undetected in the near-infrared at $K \geq 25.7$.

Since SMGs are dominated by high redshift, dusty highly star-forming galaxies, their observed optical/near-infrared colours are typically red (e.g. Smail et al. 1999, 2004), and so the detection rate as a function of wavelength drops at shorter wavelengths, reaching just 26 per cent in the $U$ band (Table 1). We will return to a discussion of the detected fraction of SMGs as a function of wavelength, their colours, and implications on derived quantities in Section 3.3.

### 2.2.2 Spitzer *IRAC and MIPS observations*

Next, we turn to the mid-infrared coverage of the UDS, in particular from *Spitzer* IRAC and MIPS observations. At these wavelengths, the observed 3.6–8.0 $\mu$m emission samples the rest-frame near-infrared at the expected redshifts of the SMGs. These wavelengths are less dominated by the youngest stellar populations, and significantly less affected by dust than the rest-frame optical or UV. Observations of the UDS in the mid-infrared were taken with IRAC onboard the *Spitzer* telescope as part of the *Spitzer* Legacy Program (SpUDS; PI: J. Dunlop).

**Table 1.** Photometric coverage and detection fractions for AS2UDS SMGs in representative photometric bands.

| Band | $N_{\rm covered}$ | $N_{\rm detected}$ | $\%_{\rm detected}$ | Depth ($3\sigma$) |
|---|---|---|---|---|
| $U$ | 634 | 162 | 26 | 27.1 AB |
| $V$ | 590 | 330 | 56 | 27.6 AB |
| $K$ | 634 | 526 | 83 | 25.7 AB |
| 3.6 $\mu$m | 644 | 580[a] | 90[b] | 23.5 AB |
| 24 $\mu$m | 628 | 304 | 48 | 60 $\mu$Jy |
| 350 $\mu$m | 707 | 417 | 59 | 8.0 mJy |
| 1.4 GHz | 705 | 272 | 39 | 18 $\mu$Jy |

[a]Including 109 potentially contaminated sources (see Section 2.2.2).
[b]73% if excluding 109 potentially contaminated sources. $N_{\rm covered}$ – number of SMGs covered by imaging; $N_{\rm detected}$ – number of SMGs detected above $3\sigma$ ; and $\%_{\rm detected}$ – percentage of total sample detected.

We obtained reduced SpUDS images of the UDS from the *Spitzer* Science Archive. These IRAC observations at 3.6, 4.5, 5.8, and 8.0 $\mu$m reach $3\sigma$ depths of 23.5, 23.3, 22.3, and 22.4 mag, respectively. The astrometry of all four IRAC images was aligned to the ALMA maps by stacking the IRAC thumbnails of the ALMA positions of 707 AS2UDS sources and corrections in RA/Dec. of (+0.″00, +0.″15), (+0.″08, +0.″12), (+0.″08, +0.″00), and (+0.″60, −0.″08) were applied to the 3.6-, 4.5-, 5.8-, and 8.0-$\mu$m images, respectively. To measure the photometry, and minimize the effect of blending, we extract 2-arcsec-diameter aperture photometry for all of the ALMA SMGs, as well as for all 205 910 galaxies in the UKIDSS DR11 catalogue, and calculate aperture corrections to total magnitudes from point sources in the images. The UKIDSS DR11 catalogue contains aperture-corrected magnitudes measured in the 3.6- and 4.5-$\mu$m bands and we confirm our photometry at these wavelengths by comparing the respective magnitudes, with relative offsets of just $\Delta[3.6]/[3.6]_{\rm DR11} = 0.001^{+0.007}_{-0.005}$ and $\Delta[4.5]/[4.5]_{\rm DR11} = 0.002^{+0.009}_{-0.003}$.

Due to the relatively large point spread function of the IRAC images (typically ∼2 arcsec FWHM), blending with nearby sources is a potential concern (see Fig. 1). We, therefore, identify all of the ALMA SMGs that have a second, nearby $K$-band detected, galaxy within 2.5 arcsec and calculate the possible level of contamination assuming that the flux ratio of the ALMA SMG and its neighbour is the same in the IRAC bands, as observed in the higher resolution $K$-band images. This is conservative as the SMGs are expected to be typically redder than any contaminating field galaxies. For any ALMA SMG, if the contamination from the nearby source is likely to be more than 50 per cent of the total flux, the respective IRAC magnitudes are treated as $3\sigma$ upper limits. This transformation of detected fluxes into upper limits affects 109 sources.

From the photometry of the ALMA SMGs in the IRAC bands, we determine that 581 645 or 90 per cent of the SMGs covered by IRAC are detected at 3.6 $\mu$m, or 73 per cent when we apply the conservative blending criterion from above. The increased fraction of the sample that is detected in the IRAC bands, compared to the $K$ band, most likely reflects the (rest-frame) 1.6-$\mu$m stellar 'bump' that is redshifted to $\gtrsim$3 $\mu$m for an SMG at $z \gtrsim 1$. We will return to a discussion of the mid-infrared colours in Section 2.4.

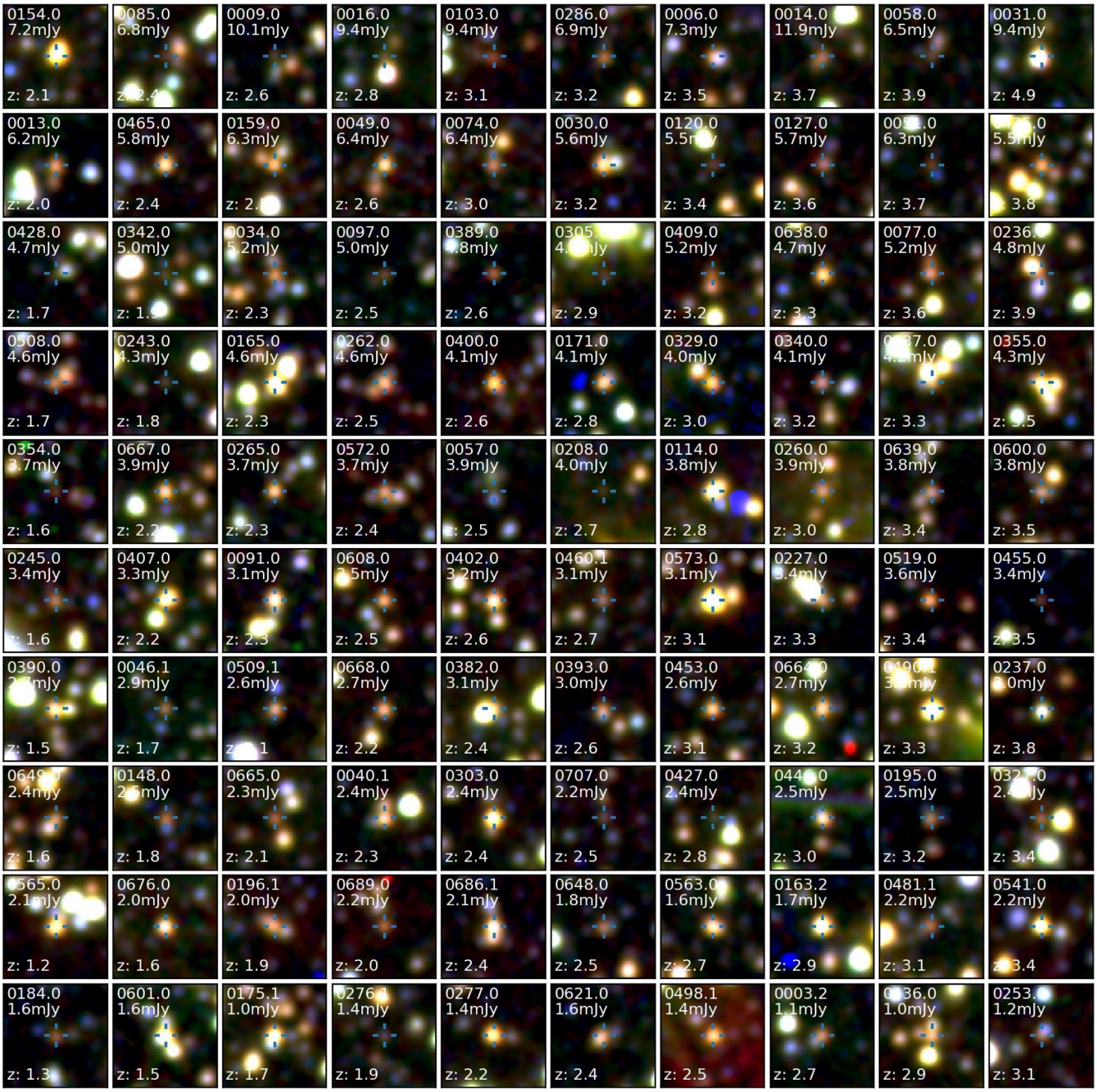


**Figure 1.** Examples of 100 of the AS2UDS ALMA-identified SMGs from our sample. The 25 × 25 arcsec$^2$ ($\sim$200-kpc square at their typical redshifts) colour images are composed of *K*, and IRAC 3.6- and IRAC 4.5-$\mu$m bands with the ALMA position of the source given by the open cross. The sources are selected to be representative of the near-infrared properties of the full sample: thumbnails are ranked in deciles of flux (each row) and deciles of $z_{\rm phot}$ within each flux range (each column). We see that SMGs are in general redder than the neighbouring field galaxies. There is a weak trend for SMGs to become fainter and/or redder with redshift, but there is no clear trend of observed properties with $S_{870}$ flux density.

To demonstrate the typically red colour of the SMGs (in particular compared to the foreground field galaxy population), in Fig. 1 we show colour images (composed of *K*, IRAC 3.6- and 4.5-$\mu$m bands) for 100 representative AS2UDS SMGs ranked in terms of $S_{870}$ and photometric redshift (see Section 4.1 for the determination of the photometric redshifts). This figure demonstrates that SMGs generally have redder near-/mid-infrared colours than neighbouring field galaxies and also that on average higher redshift SMGs are fainter and/or redder in the near-infrared bands than low redshift ones for each of the ALMA flux bins. We see no strong trends in observed properties with 870-$\mu$m flux density in any redshift bin.

Mid-infrared observations of the UDS were also taken at 24 $\mu$m with the Multiband Imaging Photometer (MIPS) on board *Spitzer* as part of SpUDS. The 24-$\mu$m emission provides useful constraints on the star formation and AGN content of bright SMGs since at the typical redshift of our sample, the filter samples continuum emission from heated dust grains. This spectral region also includes broad emission features associated with polycyclic aromatic hydrocarbons

(PAHs) – the most prominent of which appear at rest-frame 6.2, 7.7, 8.6, 11.3, and 12.7 $\mu$m, as well as absorption by amorphous silicates centred at 9.7 and 18 $\mu$m (Pope et al. 2008; Menéndez-Delmestre et al. 2009). This MIPS 24-$\mu$m imaging is also employed to provide a constraint on the positional prior catalogue that is used to deblend the *Herschel* far-infrared maps (e.g. Roseboom et al. 2012; Magnelli et al. 2013; Swinbank et al. 2014). We obtained the reduced SpUDS/MIPS 24-$\mu$m image from the NASA Infrared Astronomy Archive. This imaging covers the entire UDS survey area and reaches a 3$\sigma$ (aperture corrected) limit of 60 $\mu$Jy. From the 24-$\mu$m image, we identify ∼35,000 sources, and cross-matching the >3$\sigma$ detections in the 24-$\mu$m catalogue with our ALMA catalogue with a 2 arcsec matching radius, we determine that 48 per cent of the SMGs are detected. This detected fraction is also consistent with that of other fields with similar ALMA and MIPS coverage (e.g. 41 per cent in ALESS from Simpson et al. 2014).

### 2.3 Far-infrared and radio imaging

#### *2.3.1* Herschel *SPIRE and PACS)observations*

To measure reliable far-infrared luminosities for the ALMA SMGs, we exploit observations using the SPIRE and the Photodetector Array Camera and Spectrometer (PACS) on board the Herschel Space Observatory. These observations were taken as part of the Herschel Multi-tiered Extragalactic Survey (HerMES; Oliver et al. 2012) and cover the observed wavelength range from 100–500 $\mu$m. These wavelengths are expected to span the dust-peak of the SED, which (in local ULIRGs) peak around 100 $\mu$m, corresponding to a characteristic dust temperature of $T_{\rm d} \simeq 35$ K (e.g. Symeonidis et al. 2013; Clements et al. 2018). At $z \sim 2.5$, the dust SED is expected to peak around an observed wavelength of 350 $\mu$m (e.g. see Casey, Narayanan & Cooray 2014 for a review).

Due to the coarse resolution of the *Herschel*/SPIRE maps (∼ 18-, 25-, and 36-arcsec FWHM at 250, 350, and 500 $\mu$m, respectively), we need to account for the effect of source blending (Roseboom et al. 2012; Magnelli et al. 2013). We, therefore, follow the same procedure as Swinbank et al. (2014). Briefly, the ALMA SMGs, together with *Spitzer*/MIPS 24-$\mu$m and 1.4-GHz radio sources, are used as positional priors in the deblending of the SPIRE maps. A Monte Carlo algorithm is used to deblend the SPIRE maps by fitting the observed flux distribution with beam-sized components at the position of a given source in the prior catalogue. To avoid 'overblending' the method is first applied to the 250-$\mu$m data, and only sources that are either (i) ALMA SMGs, or (ii) detected at $> 2\sigma$ at 250 $\mu$m are propagated to the prior list for the 350-$\mu$m deblending. Similarly, only the ALMA SMGs and/or those detected at $> 2\sigma$ at 350 $\mu$m are used to deblend the 500-$\mu$m map. The uncertainties on the flux densities (and limits) are found by attempting to recover fake sources injected into the maps (see Swinbank et al. 2014 for details), and the typical 3$\sigma$ detection limits are 7.0, 8.0, and 10.6 mJy at 250, 350, and 500 $\mu$m, respectively. The same method is applied to the PACS 100- and 160-$\mu$m imaging, with the final 3$\sigma$ depths of 5.5 mJy at 100 $\mu$m and 12.1 mJy at 160 $\mu$m.

Given the selection of our sources at 870 $\mu$m, the fraction of ALMA SMGs that are detected in the PACS and/or SPIRE bands is a strong function of 870-$\mu$m flux density, but we note that 69 per cent (486/707) of the ALMA SMGs are detected in at least one of the PACS or SPIRE bands. This will be important in Section 4 when deriving useful constraints on the far-infrared luminosities and dust temperatures.

In terms of the field galaxies, just 3.6 per cent of the *K*-band sample have a MIPS 24-$\mu$m counterpart, and of these only 2396 (out of a total of 205 910 galaxies in DR11) are detected at 250 $\mu$m, with 1,497 and 500 detected at 350 and 500 $\mu$m, respectively. Thus, the majority of the field population are not detected in the far-infrared (in contrast to the ALMA SMGs, where the majority of the galaxies are detected).

#### *2.3.2 VLA 1.4 -GHz radio observations*

Finally, we turn to radio wavelengths. Prior to ALMA, high-resolution (∼ 1 arcsec) radio maps had often been employed to identify likely counterparts of single-dish sub-millimetre sources (e.g. Ivison et al. 1998). Although the radio emission does not benefit from the negative *k*-correction experienced in the sub-millimetre waveband, the lower redshift ($z \lesssim 2.5$) ALMA SMGs tend to be detectable as $\mu$Jy radio sources due to the strong correlation between the non-thermal radio and far-infrared emission in galaxies (e.g. Yun, Reddy & Condon 2001; Ivison et al. 2002, 2007; Vlahakis, Eales & Dunne 2007; Biggs et al. 2011; Hodge et al. 2013). The standard explanation of this relationship is that both the far-infrared emission and the majority of the radio emission traces the same population of high-mass stars ($\gtrsim 5\,{\rm M}_{\odot}$). These stars both heat the dust (which then emits far-infrared emission) and produce the relativistic electrons responsible for synchrotron radiation when they explode as supernovae (e.g. Helou, Soifer & Rowan-Robinson 1985; Condon 1992). However, the lack of a negative *k*-correction in the radio waveband means that at higher redshifts ($z \gtrsim 2.5$), where a large fraction of the SMGs lie, their radio flux densities are often too faint to be detectable, for example, Hodge et al. (2013) show that up to 45 per cent of ALMA SMGs in their ALESS survey are not detected at 1.4 GHz.

The UDS was imaged at 1.4 GHz with the Very Large Array (VLA) using ∼160 h of integration. The resulting map has an rms of $\sigma_{1.4{\rm GHz}} \simeq 6\,\mu{\rm Jy\,beam}^{-1}$ (Arumugam et al. in preparation; for a brief summary, see Simpson et al. 2013). In total, 6,861 radio sources are detected at signal-to-noise ratio (S/N) > 4, and 706/707 of the ALMA SMGs are covered by the map. Matching the ALMA and radio catalogues using a 1.6 arcsec search radius (∼1 per cent false-positive matches) yields 273 matches at a 3$\sigma$ level, corresponding to a radio detection fraction of 39 per cent (see also An et al. 2018), which is similar to the detected radio fraction in other comparable SMG surveys (∼ 30–50 per cent; e.g. Hodge et al. 2013; Biggs et al. 2011; Brisbin et al. 2017, although see Lindner et al. 2011). In Section 4.1, we will discuss the redshift distribution of the radio-detected versus non-detected fractions, as well as the influence of the radio emission on the SED modelling we perform.

### 2.4 Photometric properties of SMGs in comparison to the field population

To illustrate the broad photometric properties of our SMG sample and the constraints available on their SEDs, we list the number of SMGs detected (above 3$\sigma$) in a range of representative optical and infrared photometric bands in Table 1. It is clear that fewer detections are observed in the bluer optical wavebands, while ∼70–80 per cent of the sample (which are covered by the imaging) are detected in the *K* or the IRAC bands; this drops to 56 per cent in the *V* band. In the far-infrared, 69 per cent of the ALMA SMGs are detected in at least one of the PACS or SPIRE bands. Thus. we have good photometric coverage for the bulk of the sample longward of

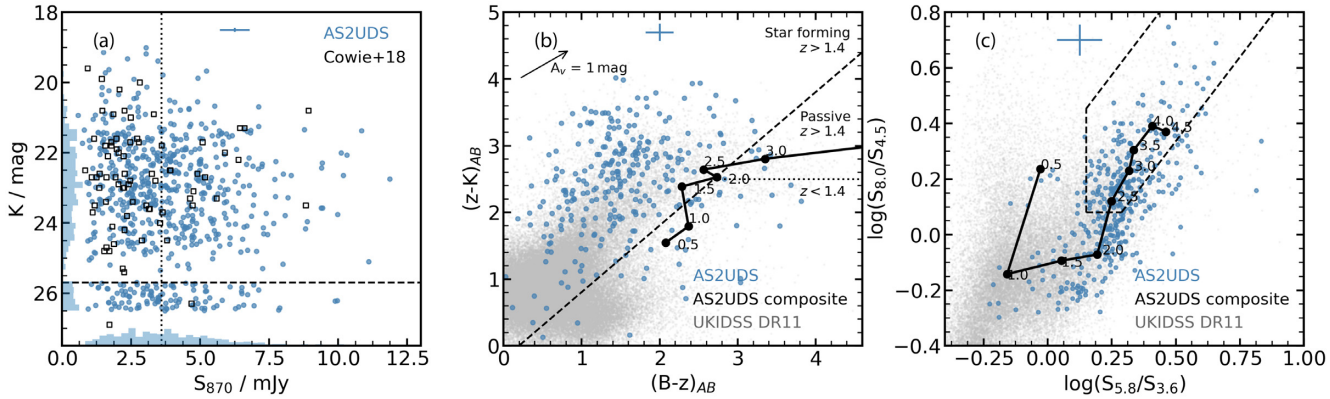


**Figure 2.** Distributions of observed magnitudes and colours of the SMGs from AS2UDS. **(a)** *K*-band magnitude versus $S_{870}$ flux density. The dashed line shows the *K*-band $3\sigma$ limit of $K = 25.7$ and the dotted line indicates the flux limit of the parent SCUBA-2 survey at $S_{870} = 3.6$ mJy. There are 526 *K*-band detections of SMGs and we plot the 108 limits scattered below the *K*-band limit. The histograms show the *K*-band magnitude distribution as the ordinate and $S_{870}$ flux density distribution as the abscissa. For comparison, we also show the Cowie et al. (2018) sample from CDFS, which covers a similar parameter range. No strong correlation of 870-$\mu$m flux density and *K*-band magnitude is observed, but we highlight that we see a two order of magnitude range in the *K*-band brightness at a fixed 870-$\mu$m flux density. **(b)** $(B - z)$ versus $(z - K)$ colour–colour diagram for 290 SMGs with detections in all three bands and the *BzK* classification regions. We stress that these are typically the brighter and bluer examples and so are not representative of the full population. The placement of the sources on the diagram suggests that the majority (253/290) of these SMGs are high-redshift star-forming galaxies, most of which are significantly redder than the field population. The reddening vector for one magnitude of extinction in the *V* band is plotted in the top left-hand panel. The solid line shows the track predicted by the composite SMG SED track at increasing redshift (labelled). We see that the average colours of SMGs lies close to the classification boundary and so it is likely that fainter and redder SMGs would be misclassified using the *BzK* colours. **(c)** IRAC colour–colour diagram for 388 SMGs detected in all four IRAC bands. The dashed line indicates the IRAC colour criteria for AGN selection (up to a redshift of $z \sim 2.5$) from Donley et al. (2012). The solid line shows the composite SED as a function of redshift (labelled). We see that a large fraction of SMGs have colours suggestive of AGN, but the majority of these lie at too high redshifts ( $z \gtrsim 2.5$) for the reliable application of this classification criterion – with their power law like IRAC colours resulting from the redshifting of the 1.6-$\mu$m bump longward of the 5.8-$\mu$m passband. The field galaxies are also plotted (in grey) and it is clear that SMGs have significantly redder colours, with the bulk of the field sample falling off the bottom left-hand corner of the plot. The average error is shown at the top of each panel.

the near-infrared, but with more limited detection rates in the bluer optical bands.

Before we discuss the multiwavelength SEDs, we first compare the optical and near-/mid-infrared colours of the SMGs and field galaxies in our sample. As this study makes use of a *K*-band selected catalogue, we investigate the distribution of *K*-band magnitudes compared to the ALMA $S_{870}$ fluxes Fig. 2(a).

Colour selection of galaxies can provide a simple method to identify high-redshift galaxies. For example, Daddi et al. (2004) suggested a criteria based on $(B - z)$ and $(z - K)$ (*BzK*) with $BzK = (z - K) - (B - z)$ to select star-forming galaxies at $z \simeq 1.4$–2.5. Although the SMGs are likely to be more strongly dust-obscured than typical star-forming galaxies at these redshifts, this diagnostic still provides a useful starting point to interpret the rest-frame UV/optical colours, and we show the SMGs in the $(z - K) - (B - z)$ colour space in Fig. 2(b). We see that compared to a field galaxy sample, as expected, the SMGs are significantly redder, likely due to their higher dust obscuration and higher redshifts. Nevertheless, for our sample of 290 AS2UDS SMGs with detections in all three *B*, *z*, and *K* bands, 87 per cent (253/290) of sources lie above $BzK = -0.2$, which is the suggested limit that separates star-forming galaxies from passive galaxies, indicating that the majority of these *BzK*-detected (hence bluer than average) SMGs have the colours expected for a star-forming population. However, we caution that 14 per cent of our sample of these *BzK*-detected highly dust-obscured star-forming galaxies are misclassified as 'passive'. Moreover, we note that the SMG subset shown on this *BzK* plot is strongly biased due to the large fraction of SMGs that are not shown because they are undetected in the optical bands, especially the *B* band. To highlight this, we overlay the track for our composite SED (see Section 4.2), which should more accurately represent the 'typical' SMG, as a function of increasing redshift. This indicates that at $z \simeq 1.5$–2.5 the average SMG has *BzK* colours, which lie on the border of the star-forming criterion, suggesting that a significant fraction of $z \lesssim 2.5$ SMGs would not be selected as star-forming systems based on their *BzK* colours, even if we had extremely deep *B*-band observations.

Given that the detection rate of ALMA SMGs is much higher in the mid-infrared IRAC bands, in Fig. 2(c), we show the $S_{5.8}/S_{3.6}$ versus $S_{8.0}/S_{4.5}$ colour–colour plot for 388 SMGs that are detected in all four IRAC bands. This colour–colour space has been used to identify high-redshift star-forming galaxies, as well as isolate candidate AGN at $z \lesssim 2.5$ from their power-law spectra (e.g. Donley et al. 2012). In this figure, on average, the IRAC-detected ALMA SMGs are again significantly redder than the field population (see also Stach et al. 2019). We overlay the track formed from the composite SED of our sample (see Section 4.2), which demonstrates that these IRAC-detected SMGs are likely to lie at $z \simeq 2$–3. Hence, although it might appear from Fig. 2(c) that many of the SMGs have mid-infrared colours suggestive of an AGN (power law like out to 8 $\mu$m), this is simply because many of these lie at $z > 2.5$ where sources cannot be reliably classified using this colour selection. Indeed, Stach et al. (2019) estimate a likely AGN fraction in AS2UDS based on X-ray detections of just $8 \pm 2$ per cent. As seen from the composite SED track, the sources in the AGN colour region are, on average, at higher redshifts ($z > 2.5$), where the 1.6-$\mu$m stellar 'bump' falls beyond the 5.8-$\mu$m band, and the Donley et al. (2012) AGN criteria breaks down.

In summary, the basic photometric properties of SMGs show them to be redder than average field galaxies across most of the UV/optical to the mid-infrared regime, likely due to a combination of their higher redshifts and higher dust obscuration. High-redshift SMGs are also fainter than the low-redshift SMGs in the optical

and near-infrared wavebands (Fig. 1), but with a large dispersion in properties at any redshift.

## 3 MAGPHYS: TESTING AND CALIBRATION

To constrain the physical properties of the AS2UDS SMGs, we employ MAGPHYS (da Cunha, Charlot & Elbaz 2008; da Cunha et al. 2015; Battisti et al. 2019) – a physically motivated model that consistently fits rest-frame SEDs from the optical to radio wavelengths. An energy balance technique is used to combine the attenuation of the stellar emission in the UV/optical and near-infrared by dust, and the reradiation of this energy in the far-infrared. The MAGPHYS model includes the energy absorbed by dust in stellar birth clouds and the diffuse ISM. This approach provides several significant advances compared to modelling the optical and infrared wavelengths separately (e.g. Simpson et al. 2014; Swinbank et al. 2014), allowing more control of the covariance between parameters and generally providing more robust constraints on the physical parameters (e.g. redshifts, stellar masses, and star-formation rates). However, we note that the modelling assumes that sub-millimetre and optical emission are coming from a region of comparable size, which is a simplification of the true system.

Before we apply MAGPHYS to the SMGs in our sample, we briefly review the most important aspects of the model that are likely to affect our conclusions and discuss a number of tests that we apply to validate our results. For a full description of MAGPHYS, see da Cunha et al. (2008; 2015) and Battisti et al. (2019).

MAGPHYS uses stellar population models from Bruzual & Charlot (2003), a Chabrier initial mass function (IMF) (Chabrier 2003) and metallicities that vary uniformly from 0.2 to 2 times solar. Star-formation histories are modelled as continuous delayed exponential functions (Lee et al. 2010) with the peak of star formation occurring in range of 0.7–13.3 Gyr after the onset of star formation. The age is drawn randomly in the range of 0.1–10 Gyrs. To model starbursts, MAGPHYS also superimposes bursts on top of the star-formation history. These bursts are added randomly, but with a 75 per cent probability that they occurred within the previous 2 Gyr. The duration of these bursts varies in the range of 30–300 Myr with a total mass formed in stars varying from 0.1 to 100 times the mass formed by the underlying continuous model. In this way, starbursts, as well as more quiescent galaxies, can be modelled. We note that the SFR returned from MAGPHYS for a given model is defined as the average of the star-formation history over the last 100 Myr.

The far-infrared emission from dust in MAGPHYS is determined self-consistently from the dust attenuated stellar emission. Dust attenuation is modelled using two components following Charlot & Fall (2000): a dust model for young stars that are still deeply embedded in their birth clouds; and a dust model for the intermediate/old stars in the diffuse ISM. The far-infrared luminosity we report is measured by integrating the SED in the rest-frame between 8 and1000 $\mu$m and is calculated through the sum of the birth cloud and ISM luminosities, which also include contributions from the PAHs, and mid-infrared continuum from hot, warm, and cold dust in thermal equilibrium. The dust mass is calculated using the far-infrared radiation and a wavelength-dependent dust mass coefficient. For a full description of how each parameter is modelled, see da Cunha et al. (2015) and Battisti et al. (2019).

For our analysis, we used the updated MAGPHYS code from da Cunha et al. (2015) and Battisti et al. (2019), which is optimised to fit SEDs of high redshift ( $z > 1$) star-forming galaxies. This code includes modifications such as extended prior distributions of star-formation history and dust optical depth effects, as well as the inclusion of intergalactic medium (IGM) absorption of UV photons. The updated version also includes photometric redshift as a variable.

To fit the photometry of a galaxy, MAGPHYS generates a library of SEDs for a grid of redshifts for each star-formation history considered. MAGPHYS identifies the models that best-fit the multiwavelength photometry by matching the model SEDs to the data using a $\chi^2$ test and returns the respective best-fitting parameters. In this study, we focus on eight of the derived parameters: photometric redshift ($z$); star-formation rate (SFR); stellar mass ($M_*$); mass-weighted age ($\mathrm{Age_m}$); dust temperature ($T_\mathrm{d}$); dust attenuation ($A_\mathrm{V}$); far-infrared luminosity ($L_\mathrm{IR}$); and dust mass ($M_\mathrm{d}$).

For each parameter, MAGPHYS returns the probability distribution function (PDF) from the best-fitting model. The derived parameters (e.g. photometric redshift, stellar mass, etc.) are taken as the median from the PDF, with uncertainties reflecting the 16–84th percentile values of this distribution (we note that if we instead adopted the peak value from the PDF, none of the conclusions below is significantly affected). In a small number of cases, the SEDs are overly constrained due to the finite sampling, and the PDFs are highly peaked, meaning the returned uncertainties are unrealistically low. In these cases, we take a conservative approach and adopt the median uncertainty from the full sample for that derived parameter. We flag the sources where this has occurred in the online catalogue (Table A1 in Appendix A).

A significant fraction of the SMGs in our sample are faint or undetected in one or more of the 22 wavebands that we employ in our analysis – most frequently this is at the bluest optical wavelengths (see Table 1) due to their high redshift and dusty natures. Thus, we first assess how the flux upper limits affect the model fitting.

As a first step, in any given waveband, we treat a source as detected if it has at least a $3\sigma$ detection. For non-detections, we conservatively adopt a flux of zero and a limit corresponding to $3\sigma$ in the UV-to-mid-infrared bands (i.e. up to 8 $\mu$m). This is motivated by a stacking analysis of ALMA SMGs in ALESS where the individually optically faint or undetected SMGs yielded no or only weak detections in the stacks (e.g. Simpson et al. 2014). In the far-infrared, most of the 'non-detections' occur in the *Herschel* maps, which are confusion-noise dominated. Stacking analysis of SMGs at 250–500 $\mu$m has demonstrated that the flux densities of ALMA SMGs at these wavelengths are often just marginally below the confusion noise (e.g. Simpson et al. 2014). To this end, for non-detected sources in the infrared (beyond 10 $\mu$m), we adopt a flux density of $1.5 \pm 1.0\sigma$. Other choices of limits were tested (e.g. $0 \pm 1\sigma$ for all wavebands, $0 \pm 1\sigma$ for optical/near-infrared and $1.5 \pm 1.0\sigma$ for infrared) with no significant changes found for any of the derived physical parameters.

We run MAGPHYS on all 707 ALMA SMGs in our sample, and in Fig. 3 we show the observed photometry and best-fit MAGPHYS model for four representative examples. All SED fits are shown online (Fig. A1 in Appendix A). These examples are selected to span the range in the number of photometric detections included in the SEDs: from sources that are detected in all of the available 22 photometric bands (37 per cent of sources have coverage in 22–16 bands), 16 bands (28 per cent have coverage in 16–11 bands), 11 bands (20 per cent have coverage in 11–5 bands), and down to 5 bands (15 per cent have coverage in 5 or less bands). We also plot the resulting photometric redshift PDF for each of these SMGs. This demonstrates that when the SED is well constrained (e.g. the galaxy is detected in a large fraction of the photometric bands), the range of possible photometric redshifts is narrow, e.g. with a median 16–84th percentile range of $\Delta z = 0.20$ for SMGs with detections in all 22 bands. However, as the number of detection decreases, this range

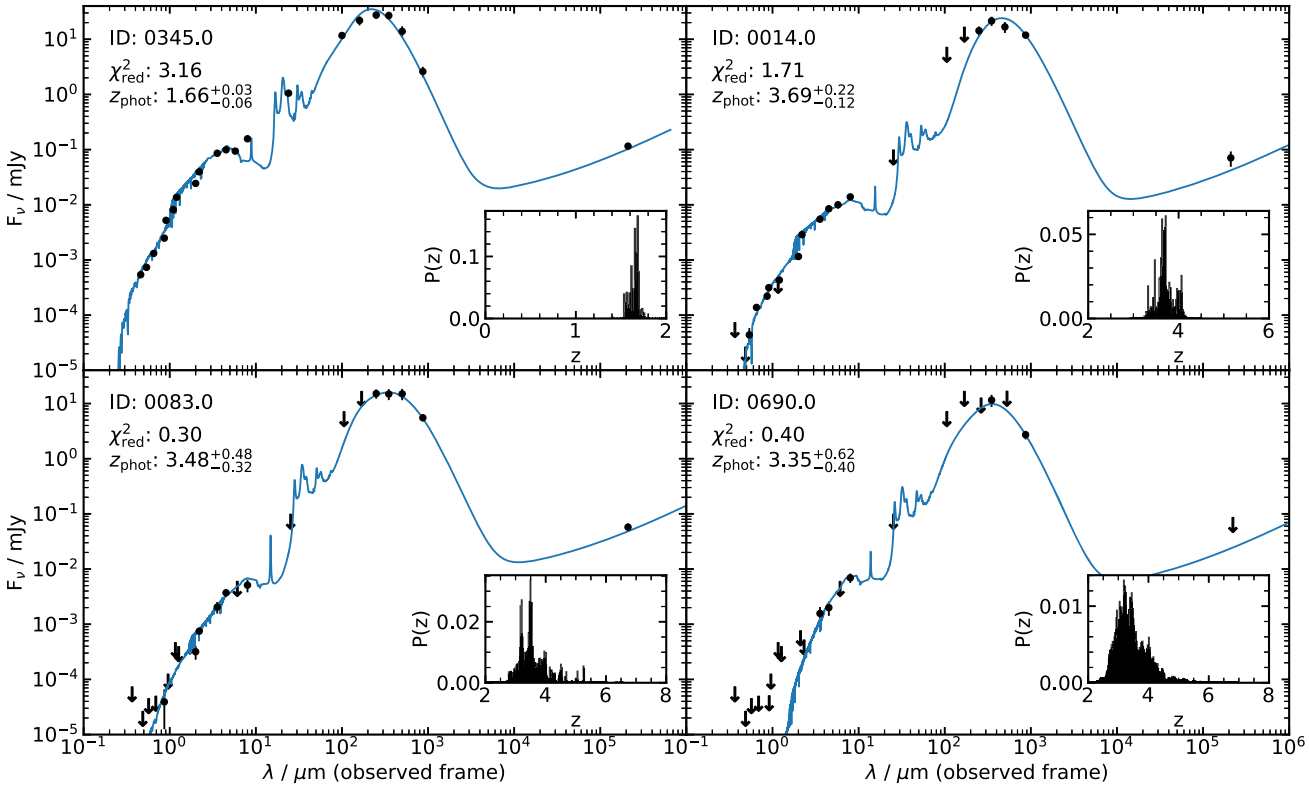


**Figure 3.** The observed-frame optical to radio SEDs of four example AS2UDS SMGs selected to have a decreasing number of photometric detections: 22/22 in the top left-hand panel; 16 in the top right panel; 11 in the bottom left panel; and 5 in the bottom right panel. Limits in the optical/near-infrared wavebands (*U*- band to IRAC 8 $\mu$m) were treated as $0 \pm 3\sigma$, while those beyond 10 $\mu$m (MIPS 24$\mu$m to Radio 1.4GHz) are set to $1.5\sigma \pm 1\sigma$. These limits are indicated as arrows. The solid line shows the predicted SED at the peak redshift of the best-fit PDF. The inset plots show the redshift probability distributions. As expected, as the number of photometric detections decreases, the redshift distribution becomes wider and the predicted photometric redshifts become more uncertain. For reference, of our 707 SMGs, 50 per cent have $\geq 11$ photometric detections, while 82 per cent have $\geq 5$ detections.

broadens. For our full sample of SMGs, the median number of bands that are detected is 12, which yields a median 16–84th percentile redshift range on any given SMG of $\Delta z = 0.50$. For reference, the median uncertainty for the 18 per cent of SMGs that are detected in $\leq$6 bands is $\Delta z = 0.86$. Note also that in some cases the reduced $\chi^2$ decreases as the number of detections decreases. This does not necessarily indicate a better fit, but rather often reflects the large uncertainties in non-detected wavebands.

Finally, before testing the accuracy of the photometric redshifts, we ensure that the energy balance technique is appropriate and the far-infrared photometry is not affecting the redshift prediction significantly. We run MAGPHYS on SMGs with *K*-band detections including only photometry up to 8 $\mu$m and compare the predicted photometric redshifts to the values derived using the full UV-to-radio photometry. We find that the scatter of photometric redshifts is within the error range as the median is $(z_{\rm full} - z_{\leq 8\,\mu{\rm m}})/(z^{84th}_{\rm full} - z^{16th}_{\rm full}) = 0.11$ with 68th percentile range of -1.0–0.95. Thus, coupling far-infrared information into the estimation of photometric redshifts is not introducing any significant biases.

### 3.1 Testing against spectroscopic redshifts

Before discussing the redshift distribution of our SMGs, we first confirm the reliability of MAGPHYS to measure photometric redshifts, and critically their uncertainties (see also Battisti et al. 2019) by comparing the photometric and spectroscopic redshifts for both the SMGs and the field galaxies in the UDS.

First, we run MAGPHYS on all 6719 *K*- band detected galaxies in the UKIDSS DR11 catalogue that have archival spectroscopic redshifts, and that have no photometric contamination flags (Smail et al. 2008; Almaini et al., in preparation; Hartley et al. in preparation). This includes 44 of the SMGs from our sample (including new spectroscopic redshifts from KMOS observations; Birkin et al. in preparation). We note that it is possible, and indeed probable, that given the wide variety of sources from which these redshifts were taken and the faintness of many of the target galaxies, that some of these spectroscopic redshifts are incorrect. As a result, we concentrate on the quality of the agreement achieved for the bulk of the sample, giving less emphasis to outliers. We also note that, given the heterogeneous sample selection, the sample contains a mix of populations, which is likely to include an increasing fraction of AGN hosts at higher redshifts, the SEDs for which are not reproduced by the current version of MAGPHYS.

We further isolate a sub-sample of all field galaxies with no photometric contamination flags above $z = 2$ and include 500 galaxies with spectroscopic redshifts below $z = 2$ to form a field sample biased towards higher-redshift/fainter sources that is more representative of the distribution of high-redshift SMGs. MAGPHYS run on this sub-sample yields a median offset between the spectroscopic and photometric redshifts of $\Delta z/(1 + z_{\rm spec}) = 0.004 \pm 0.001$, although with larger systematic offsets at redshift above $z \simeq 2.5$ ($\Delta z/(1 + z_{\rm spec}) = 0.040 \pm 0.003$). At these redshifts, the photometric redshift has sensitivity to the IGM opacity as the Lyman break (rest-frame 912–1215 Å) pass through the observed *B* band

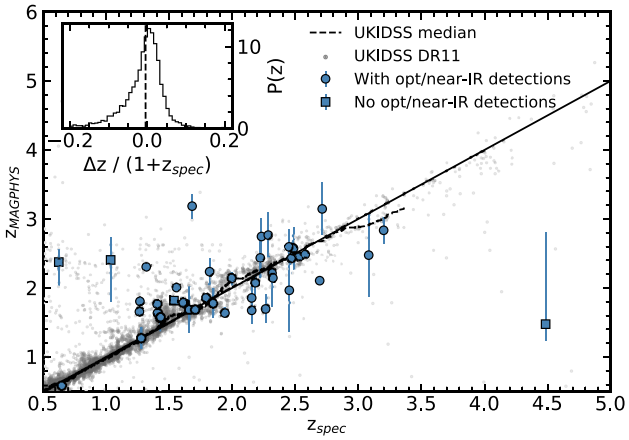


**Figure 4.** Comparison of MAGPHYS photometric redshifts versus spectroscopic redshifts. The 44 AS2UDS SMGs with spectroscopic redshifts are plotted, as well as field sample of 6,719 *K*-detected UDS galaxies with spectroscopic redshifts. The dashed line shows the running median for the field galaxies, which tracks the spectroscopic redshifts closely up to $z \sim 3.5$. For the SMGs, we identify the four that lack detections in the optical bands. The inset panel shows the fractional offset of photometric redshifts from spectroscopic values for the field sample. The median offset is $(z_{\rm spec} - z_{\rm phot})/(1 + z_{\rm spec}) = -0.005 \pm 0.003$ with a dispersion of 0.13.

for sources that are bright enough to be detectable. Adjusting the IGM absorption coefficient in the SED model can reduce this systematic $\Delta z$ offset (e.g. Wardlow et al. 2011). The IGM effective absorption optical depth of each model is drawn from a Gaussian distribution centred at the mean value given in Madau (1995), with a standard deviation of 0.5. We, therefore, rerun MAGPHYS for the spectroscopic sample with IGM absorption coefficients between 0.2 and 1.0 of each drawn model value. From this test, we find that tuning the IGM coefficient to 0.5 of the initially drawn value minimises the systematic offset between the spectroscopic and photometric redshifts above $z \sim 2$, whilst maintaining the closest match at lower redshift, thus we adopt it in any subsequent analysis. In Fig. 4, we show the comparison of the spectroscopic and photometric redshifts for the field galaxies and SMGs. We see that for the SMGs the three most extreme outliers are optically undetected, leading to uncertain estimation of their redshifts. The fourth outlier is a secondary ALMA source within a single SCUBA-2 map, where the optical photometry may have been mismatched. Over the full redshift range, the offsets between the spectroscopic and photometric redshifts for all 6,719 field galaxies is $\Delta z/(1 + z_{\rm spec}) = -0.005 \pm 0.003$, and $\Delta z/(1 + z_{\rm spec}) = -0.02 \pm 0.03$, with a $1\sigma$ scatter of $\Delta z/(1 + z_{\rm spec}) = 0.13$, if we just consider the 44 SMGs. The photometric redshift accuracy we obtain is comparable to that found for SMGs in the COSMOS field by Battisti et al. (2019).

We check what effect the error on the photometric redshift has on our inferred physical properties by running MAGPHYS on the AS2UDS sub-sample of 44 SMGs with spectroscopic redshifts at their fixed spectroscopic redshifts. We investigate whether the change in the derived value of the property at the spectroscopic redshift and the photometric redshift is encompassed by the quoted errors (at the photometric redshift and including the covariance due to the uncertainty in this value) by calculating the fractional difference, $X_{\rm spec}/X_{\rm phot}$, where $X$ is any given parameter. The change for all the predicted parameters was, on average, less than $\lesssim$15 per cent, which is less than the typical errors. Therefore, we confirm that the error uncertainty effect on any given parameter is captured in its error range and is not affecting final parameter distribution.

### 3.2 Modelling EAGLE galaxies with MAGPHYS – a comparison of simulated and MAGPHYS derived properties

As well as empirically testing the reliability of the predicted photometric redshifts from MAGPHYS, we also wish to test how well the other MAGPHYS-derived parameters are expected to track the corresponding physical quantities. This is more challenging, as we lack knowledge of the 'true' quantities (e.g. stellar mass or star-formation rate) for observed galaxies in our field and so we have to adopt a different approach. We, therefore, take advantage of the simulated galaxies from the Evolution and Assembly of GaLaxies and their Environments (EAGLE; Schaye et al. 2015; Crain et al. 2015) galaxy formation model to test how well MAGPHYS recovers the intrinsic properties of realistic model galaxies.

The EAGLE model is a smoothed-particle hydrodynamical simulation that incorporates processes such as accretion, radiative cooling, photoionization heating, star formation, stellar mass loss, stellar feedback, mergers, and feedback from black holes. The full description of the simulation as a whole can be found in Schaye et al. (2015) and the calibration strategy is described in Crain et al. (2015). The most recent post-processing analysis of the model galaxies in EAGLE includes dust reprocessing using the SKIRT radiative transfer code (Baes et al. 2011; Camps & Baes 2015). This yields predicted SEDs of model galaxies covering the rest-frame UV-to-radio wavelengths (e.g. Camps et al. 2018; McAlpine et al. 2019), and is calibrated against far-infrared observations from the Herschel Reference Survey (Boselli et al. 2010). Our primary goal here is to run MAGPHYS on the model photometry of EAGLE galaxies and so test whether the uncertainties on the derived quantities from MAGPHYS encompass the known physical properties of the model galaxies. This will provide us with a threshold that we can use to test the significance of any trends we observe in our real data in Section 4. We stress that MAGPHYS makes very different assumptions about the star-formation histories and dust properties of galaxies than are assumed in EAGLE and SKIRT and so this should provide a fair test of the robustness of the derived parameters from MAGPHYS for galaxies with complex star-formation histories and mixes of dust and stars.

To select a sample of galaxies from the EAGLE model, we use the largest volume in the simulation set – Ref-L0100N1504, which is a 100 cMpc on-a-side periodic box (total volume $10^6$ cMpc$^3$). However, we note that the volume of even the largest published EAGLE simulation contains only a modest number of high-redshift galaxies with star-formation rates (or predicted 870-$\mu$m flux densities) comparable to those seen in AS2UDS (McAlpine et al. 2019). As a result, to match the observations as closely as possible, but also provide a statistical sample for our comparison, we select all 9,431 galaxies from EAGLE with SFR $> 10\,{\rm M}_\odot\,{\rm yr}^{-1}$ and $z > 0.25$, but also isolate the 100 most strongly star-forming galaxies in the redshift range $z = 1.8$–$3.4$ (the 16–84th percentile redshift range of our survey). To be consistent with the observations, for each model galaxy, we extract the predicted photometry in the same photometric bands as our observations and run MAGPHYS to predict their physical properties.

We show the comparison of intrinsic EAGLE properties versus derived MAGPHYS properties for these 9,431 galaxies online (Fig. A2 in Appendix A). We concentrate our comparison on the stellar mass, SFR, mass-weighted age, dust temperature, and dust mass, since these are the quantities we will focus on in Section 4. We note

that there are systematic differences in the derived quantities from MAGPHYS compared to the expected values from EAGLE, although in all cases MAGPHYS provide remarkably linear correlations with the intrinsic values (see Fig. A2). The largest difference is in the stellar mass, where MAGPHYS predicts a stellar mass that is $0.46 \pm 0.10$ dex lower than the 'true' stellar mass in EAGLE, consistent with previous studies of systematic uncertainty in SMG masses (e.g. Hainline et al. 2011). This difference is likely to be attributed to variations in the adopted star-formation histories, dust model, and geometry between MAGPHYS and those in the radiative transfer code SKIRT. Accounting for these differences is beyond the scope of this work, and indeed, more critical for our analysis is the scatter around the line of best fit, since we can use this to further estimate the minimum uncertainty on a given parameter in our data (even if the PDF suggests the parameter is more highly constrained).

The stellar and dust masses have a scatter of 30 and 10 per cent around the best fit, respectively. The star-formation rates have a scatter of 15 per cent around the best fit, and the scatter in the ages is 50 per cent. The scatter in dust temperature is 9 per cent, and we note that dust temperatures are estimated using very different methods in the simulations and from the observations. Finally, we also use the quartile range of the scatter as a proxy to assess the significance of any trends we observe in Section 4 (i.e. we adopt a significance limit that any trend in these derived quantities seen in the SMGs must be greater than the quartile range of the scatter in Fig. A2). For the quantities in Fig. A1, these correspond to ratios of the $R = 75$th/25th quartile values of $R(T_{\rm d}) \simeq 1.2$, $R({\rm Age_m}) \simeq 4.2$, $R(M_{\rm d}) \simeq 2.7$, $R(M_*) \simeq 3.7$, and $R({\rm SFR}) \simeq 2.6$.

### 3.3 Comparing observed and MAGPHYS-derived quantities

Before we discuss any of the physical parameters for the SMG population and their evolution, we compare the derived quantities returned from MAGPHYS with those observables which they are empirically expected to correlate with (e.g. the dust mass is expected to correlate broadly with 870-$\mu$m flux density).

In Fig. 5, we plot the derived quantities returned from MAGPHYS against observed properties for the SMGs. For some quantities, we restrict the sample to the redshift range $z = 1.8$–$3.4$ (which represents the 16–84th percentile) to reduce the degeneracies with redshift. We first focus on those quantities that are most sensitive to the far-infrared part of the SED and see how these correlate with the far-infrared photometry. The main source of sub-millimetre radiation is the thermal continuum from dust grains – the rest-frame UV/optical radiation from young/hot stars is absorbed by dust and re-emitted at far-infrared wavelengths. Hence, observed 870-$\mu$m flux density should trace both the dust mass and SFR (e.g. Blain et al. 2002; Scoville et al. 2014). In Fig. 5(a), we, therefore, plot the 870-$\mu$m flux density versus estimated dust mass and star-formation rate. As this shows there is a strong correlation between 870-$\mu$m flux density and dust mass ($M_{\rm d}$), which follows $\log_{10}[M_{\rm d}(M_\odot)] = (1.20 \pm 0.03) \times \log_{10}[S_{870}({\rm mJy})] + 8.16 \pm 0.02$. This tight correlation suggests that, as expected, the 870-$\mu$m flux density tracks the cold dust mass (Scoville et al. 2014; Liang et al. 2018). The trend of 870-$\mu$m flux density with star-formation rate is also clear in Fig. 5(b). Fitting to the SMGs, the correlation between 870-$\mu$m flux density and star-formation rate has the form $\log_{10}[{\rm SFR}({\rm M_\odot yr^{-1}})] = (0.42 \pm 0.06) \log_{10}[S_{870}({\rm mJy})] + 2.19 \pm 0.03$. The trend observed with star-formation rate is weaker than that of dust mass and has more dispersion thus constraints from shorter rest-frame far-infrared wavelengths are needed to reliably measure the star-formation rate.

The predicted star-formation rates and far-infrared luminosities from MAGPHYS closely follow the Kennicutt (1998) relation with an offset of ${\rm SFR}/{\rm SFR_{K98}}(L_{\rm FIR}) = 0.87 \pm 0.01$ (where ${\rm SFR_{K98}}(L_{\rm FIR})$ is the predicted Kennicutt relation). In addition, the total far-infrared luminosity should correlate with the observed radio luminosity, although this is used in the SED fitting due to the far-infrared–radio correlation (van der Kruit 1971, 1973). As discussed in Section 2, the radio luminosity is expected to be dominated by synchrotron radiation from relativistic electrons that have been accelerated in supernovae remnants (Harwit & Pacini 1975). The far-infrared and radio luminosities are correlated since the supernovae remnants arise from the same population of massive stars that heat and ionize the H II regions, which, in turn, heats the obscuring dust. In Fig. 5(c), we therefore, plot the MAGPHYS far-infrared luminosity (integrated between 8 and 1000 $\mu$m) as a function of the observed 1.4-GHz flux density, again restricting the sample to a redshift range of $z = 1.8$–$3.4$ (to reduce the effects of the geometrical dimming). We overlay the far-infrared-radio correlation from Ivison et al. (2010) for the median redshift of our sample SMGs ($z = 2.61$) with $q_{\rm IR} = 2.17$ (Magnelli et al. 2010) and $\alpha = -0.8$ (Ivison et al. 2010), appropriate for high redshift, strongly star-forming galaxies (Magnelli et al. 2010), where $q_{\rm IR}$ is the logarithmic ratio of bolometric infrared and monochromatic radio flux and $\alpha$ is the radio spectral index. This shows a rough correlation between the predicted far-infrared luminosities and the observed radio luminosities, which is consistent in form and normalization with that derived for the AS2UDS sample. The scatter is mainly due to variations in redshift. A more detailed analysis of the far-infrared–radio correlation in AS2UDS is given in Algera et al. (in preparation).

Next, we turn to the optical and near-infrared wavelengths. The observed optical/near-infrared emission at $z \sim 2$ corresponds to rest-frame far-UV to the $R$ band, which traces the stellar-dominated SED around the Balmer (3646 Å) and 4000 Å breaks – the former is more prominent in star-forming galaxies, while the latter is more prominent in older, quiescent galaxies, giving an indication of the galaxy's recent star-formation history. To test how the derived quantities correlate with basic observables, in Fig. 5, we plot stellar mass, optical extinction, and redshift as a function of observed magnitudes and colours of the SMGs.

First, we note that the observed $K$-band magnitude increases with increasing redshift, as a result of positive $k$-correction (Smail et al. 2004). As a guide, we, therefore, overlay the average $K$-band magnitude expected as a function of redshift based on the composite SMG SED from our sample (see Section 4.2). We also overlay the ALMA-detected SMGs in the CDFS from Cowie et al. (2018), which show a similar trend. We note that there are 108 SMGs in our sample that are undetected in the $K$ band ($K > 25.7$). The MAGPHYS-derived redshifts for this sub-sample lie in the range $z = 1.5$–$6.5$ with a median of $z = 3.0 \pm 0.1$. We will discuss this population further in Section 4.

Next, we assess the $V$-band dust attenuation, $A_V$. The optical extinction returned from MAGPHYS reflects the stellar luminosity-weighted average across the source. At $z \sim 2$, the extinction is expected to correlate with the rest-frame optical colours. In Fig. 5(e), we, therefore, plot the $A_V$ versus $(J - K)$ colour (which corresponds approximately to rest-frame $(U - R)$ colour at these redshifts and so is indicative of the optical SED slope). We also overlay in Fig. 5(e) a track representing the expected rest-frame $(U - R)$ colours (corresponding to observed $(J - K)$ at the median redshift of AS2UDS) based on the Calzetti reddening law (Calzetti et al. 2000). This reproduces the trend we see and suggests that our estimates of $A_V$ for the SMGs from MAGPHYS are reliable. Reassuringly, the

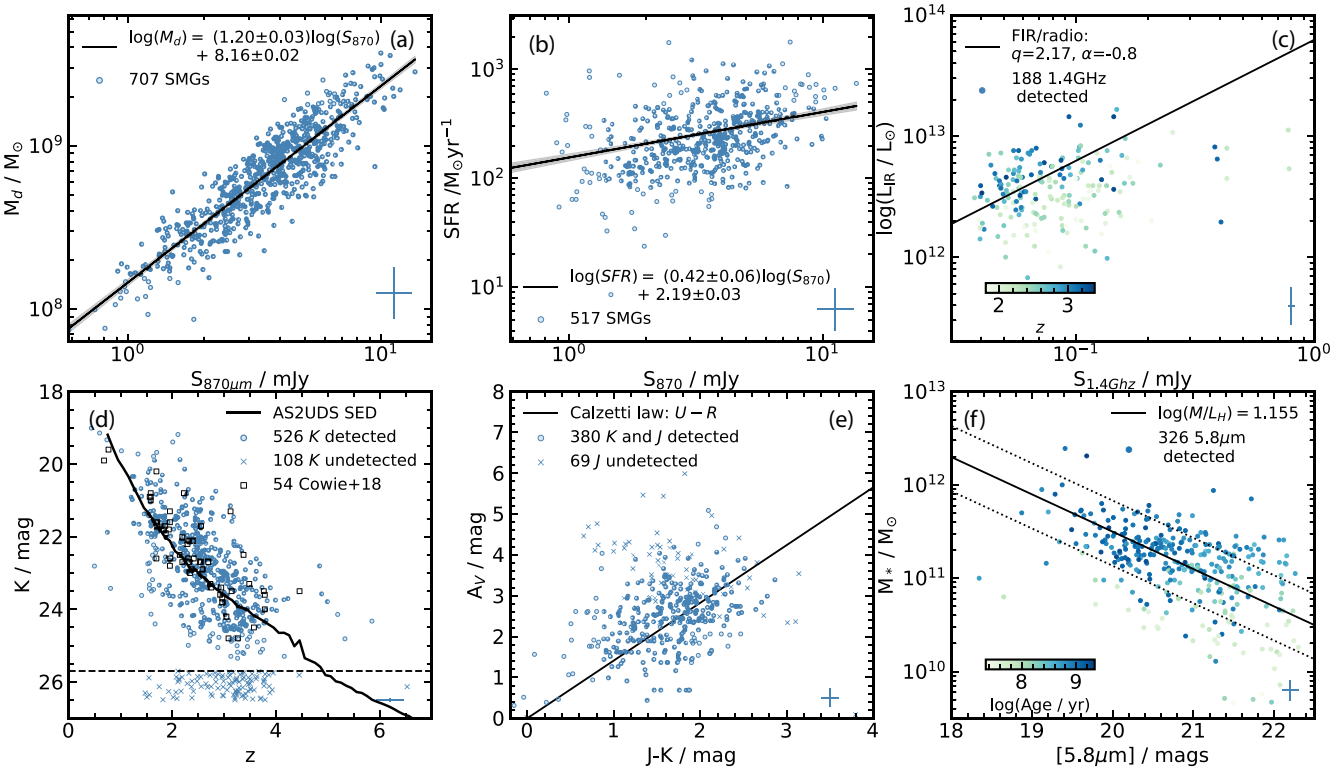


**Figure 5.** Observed photometry versus predicted physical parameters for the AS2UDS SMGs. Panels (a) and (d) include the full sample, while the other panels are for SMGs with $z = 1.8$–$3.4$. In all panels, circles indicate sources that are detected. The typical errors are shown in the bottom right of each panel. **(a)** Dust mass versus ALMA 870-$\mu$m flux for all 707 SMGs. The best-fit line has a slope of $1.20 \pm 0.03$ and the shaded region indicates the $\pm 1\,\sigma$ error range. The strong positive correlation between the observed 870-$\mu$m flux and dust mass indicates that the 870-$\mu$m emission has the most sensitivity to cold dust mass. **(b)** Star-formation rate versus ALMA 870-$\mu$m flux for 517 AS2UDS sources. We plot the best-fit line with a gradient of $0.42 \pm 0.06$ and $\pm 1\,\sigma$ errors shown as the shaded region. A positive correlation is observed, as expected for dusty SMGs, where the emission from young/hot starts is re-emitted at far-infrared wavelengths. **(c)** Far-infrared luminosity versus 1.4- GHz flux for the SMGs. The solid line shows the far-infrared–radio correlation with $q_{\rm IR} = 2.17$ at the median redshift of the AS2UDS sample. The radio-detected population are roughly consistent with the trends expected from the far-infrared–radio correlation with the scatter being mainly driven by redshift variation. **(d)** $K$ -band magnitude versus photometric redshift for 526 $K$-band detected SMGs. The 108 SMGs with no $K$-band detection are plotted below the $K$-band aperture-corrected magnitude limit of $K = 25.7$. We see a negative correlation due to the positive $k$-correction in the $K$ band. The fact that the $K$ band undetected SMGs have redshifts down to $z \sim 1.5$–$2.5$ highlights that some of the sources may be very obscured. The expected variation with redshift for the composite SED from our SMG sample is shown as a solid line. **(e)** $V$ -band dust attenuation versus $(J - K)$ colour. The solid line shows the predicted reddening from the Calzetti reddening law. As expected, the rest-frame $(U - R)$ colour (observed $(J - K)$ at the median redshift of AS2UDS) follows the predicted reddening law well, indicating that SMGs with redder colours are likely to be more dust-obscured. **(f)** Stellar mass versus IRAC 5.8-$\mu$m magnitude, coloured by estimated age. The solid line shows the track of the mass inferred from the median $H$-band mass-to-light ratio at the median redshift. The dashed lines indicate $H$-band mass-to-light ratios of $\log_{10}[M/L_{\rm H}(\mathrm{M}_\odot/L_\odot)] = 2.5$ and $\log_{10}[M/L_{\rm H}(\mathrm{M}_\odot/L_\odot)] = 0.5$. The rest-frame $H$ band (corresponding to $\sim$5.8 $\mu$m at the median redshift of the AS2UDS SMGs) correlates well with the predicted stellar mass. The scatter is mainly due to covariance of the mass with the mass-weighted age, as shown by the age trend at a given 5.8-$\mu$m magnitude.

majority of the 181 SMGs with no detection in either $J$ or $K$ band have a higher $A_V$, indicating that it is likely that their higher dust obscuration is responsible for their non-detection.

Finally, we turn to the stellar mass. It is expected that the dominant stellar population by mass in these galaxies arises from the lower mass stars, which can be better traced from the rest-frame $H$-band luminosity. At $z \sim 2$, this corresponds to the mid-infrared, around $\sim$6 $\mu$m and so in Fig. 5(f), we plot the MAGPHYS-derived stellar mass as a function of the observed-frame IRAC 5.8-$\mu$m magnitude. As expected, brighter 5.8-$\mu$m magnitudes correspond to higher stellar masses, and for SMGs in the range $z \sim 1.8$–$3.4$ we derive a correlation with $\log M_* = (-0.25 \pm 0.03)\, S_{5.8} + (16.4 \pm 0.6)$. We also overlay the prediction of mass for a median $H$-band mass-to-light ratio (1.155) for our sample SMGs and find that it follows the observed properties well. The correlation in Fig. 5(f) shows a scatter of 0.05 dex at fixed 5.8-$\mu$m magnitude on average. This scatter is due to variations in the star-formation history and dust extinction, but is also correlated with the predicted mass-weighted age of the stellar population in the sense that for a given observed 5.8-$\mu$m magnitude, the younger the inferred age of the galaxy the lower the stellar mass. We note that independent tests of the reliability of the MAGPHYS predictions for the reddening and stellar masses using the simulated EAGLE galaxies also provide mutual support for the reliability of the other parameter, given the strong covariance expected between these two quantities in any SED fit (see Fig. A2 in Appendix A).

### *3.3.1 Predicting the far-infrared properties of the field galaxies in UDS*

As we discussed in Section 2.4, we derive the physical properties of 205 910 $K$-band selected galaxies in the UDS field from the UKIDSS DR11 catalogue by applying MAGPHYS to their optical

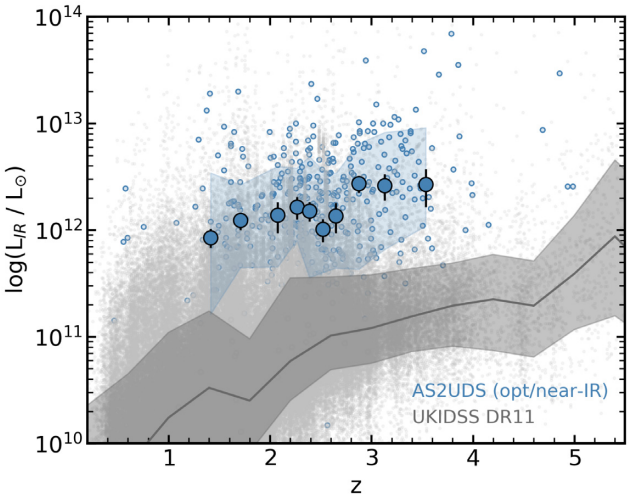


**Figure 6.** Predicted far-infrared luminosity as a function of redshift for a *K*-band selected field galaxy sample with the most reliable photometry based on a MAGPHYS analysis of just the photometry shortward of the IRAC 8.0-$\mu$m band. The solid line shows the running median and the shaded region indicates the interquartile range. We also plot the far-infrared luminosity derived for the 511 *K*-band detected SMGs, similarly limiting the model fit to photometry shortward of 8.0 $\mu$m. We indicate with filled circles the binned medians of samples of 50 SMGs ranked in redshift and the blue region shows the interquartile range. It is clear that even when MAGPHYS only has information on the optical/near-infrared SED, it still predicts AS2UDS SMGs to be significantly more far-infrared luminous than a typical field galaxy.

and near-infrared photometry (up to IRAC 8.0 $\mu$m) in an analogous way to our SMG sample. We will use this sample for a range of tests, but here we explicitly test the dust attenuation laws (and the degeneracies between age and reddening), by determining whether far-infrared luminosity can be predicted just using the optical/near-infrared part of the SED.

In Fig. 6, we plot predicted far-infrared luminosity versus redshift for the *K*-band selected field galaxy sample. We also plot those SMGs that are *K*- band detected and where we have similarly derived the predicted far-infrared luminosities based on MAGPHYS modelling of just their optical/near-infrared photometry up to 8.0 $\mu$m. Remarkably, on average, MAGPHYS is able to identify the SMGs as dusty and highly star-forming and thus far-infrared luminous using only the information shortward of $\sim$2 $\mu$m in the rest-frame. Indeed, for the *K*- band detected $S_{870} > 3.6$ mJy ALMA SMGs, the mean ratio of far-infrared luminosity from the $\leq$8-$\mu$m fit to that from the full SED, including far-infrared/sub-millimetre photometry is $L_{\rm IR}^{\leq 8\mu{\rm m}}/L_{\rm IR}^{\rm full} = 1.1 \pm 0.1$.

However, it is clear from Fig. 6 that MAGPHYS also predicts a population of $\sim$2,000 galaxies at $z \sim 1.5$–4, which are claimed to be far-infrared luminous, but which are not detected in the SCUBA-2 850-$\mu$m survey. We suspect that many of these faux-SMGs may be either sources with AGN contributions to their optical/near-infrared SEDs or hotter dust sources, missed by our 850-$\mu$m selection. Hence, while this test does confirm that the dust modelling and energy balance in MAGPHYS provides robust constrains on the far-infrared emission, it can only be used reliably if far-infrared photometric constraints are available; otherwise, the false-positive rate is high.

This comparison of derived parameters from MAGPHYS modelling of the complete SEDs of SMGs, compared to the results when restricted to only fitting photometry shortward of 8 $\mu$m, indicates a poor recovery of those parameters that are most sensitive to details of the dust SED, such as dust temperature or dust mass. However, it also suggests little change for this *K*-detected subset of the SMG population in the derived median: photometric redshifts, $(z^{\rm full} - z^{\leq 8\mu{\rm m}})/(1 + z^{\rm full}) = 0.008 \pm 0.004$ (with $1\sigma$ dispersion of 0.13); dust reddening, $(A_V^{\rm full} - A_V^{\leq 8\mu{\rm m}})/A_v^{\rm full} = 0.01 \pm 0.02$ (with $1\sigma$ dispersion of 0.30); or stellar mass, $(M_*^{\rm full} - M_*^{\leq 8\mu{\rm m}})/M_*^{\rm full} = -0.02 \pm 0.01$ (with $1\sigma$ dispersion of 0.68); and a modest bias towards younger ages when including the $> 10\,\mu$m photometry: $({\rm Age}_m^{\rm full} - {\rm Age}_m^{\leq 8\mu{\rm m}})/{\rm Age}_m^{\rm full} = -0.25 \pm 0.05$ (with $1\sigma$ dispersion of 1.85).

## 4 ANALYSIS AND RESULTS

### 4.1 Redshift distribution

The redshift distribution of SMGs can provide stringent constraints on galaxy formation models, and indeed, in some instances has forced changes in the way rapidly star-forming galaxies are modelled (e.g. Baugh et al. 2005). The early measurements of the redshift distribution of SMGs were hampered by incompleteness and errors in the identification of counterparts for single-dish sources (Chapman et al. 2005; Pope et al. 2006; Wardlow et al. 2011), although the results favoured a median redshift of $z \simeq 2.3$. More recent studies have overcome some of the weaknesses of the early work, both by unambiguously identifying the SMGs using sub-/millimetre interferometry with ALMA, and also by using a variety of methods to account for incompleteness in the estimation of redshift for the $\sim$10–20 per cent of SMGs that are too faint in the optical/near-infrared to locate multiwavelength counterparts (Simpson et al. 2014; da Cunha et al. 2015; Danielson et al. 2017; Miettinen et al. 2017; Cowie et al. 2018).

These studies suggest a slightly higher median redshift, $z \simeq 2.6$ (e.g. Simpson et al. 2014), for the SMG population at mJy-flux density limits. However, exploiting these samples to go beyond just a crude redshift distribution to investigate evolution in the properties of SMGs with redshift, have been hampered by the modest sample sizes available ($\lesssim$100 SMGs), which weakens our ability to statistically identify trends in the data (e.g. with 870-$\mu$m flux density, star-formation rate or mass). Here, our sample of 707 ALMA-identified SMGs, combined with the MAGPHYS analysis of their multiwavelength properties from deep ancillary data, provides both, complete redshift information and the large sample size necessary to simultaneously sub-divide the sample on the basis of, e.g. mass and star-formation rate to search for evolutionary trends (e.g. McAlpine et al. 2019).

We begin by deriving the redshift distribution of our SMG sample. We note that redshift prior in MAGPHYS has a broad peak at $z \sim 1.5$ (see Fig. 7a); thus, we have also tested the influence of the prior on the photometric redshifts by running MAGPHYS on all of the SMGs with a flat prior distribution (from $z = 0$–7). For the SMGs, the resulting change in the redshift distribution is negligible, with $\Delta z = 0.100 \pm 0.007$. Hence, we conclude that the prior does not have a significant effect on our estimate of the photometric redshift distribution.

With the reliability of the MAGPHYS photometric redshifts confirmed in Section 3, we derive a photometric redshift distribution for the SMGs and show this in Fig. 7(a). To capture the uncertainties in the redshifts (and the range of quality reflected in their PDFs) we stack the individual likelihood redshift distributions of all of the SMGs. For the complete sample of 707 870 $\mu$m selected SMGs, we determine a median redshift of $z = 2.61 \pm 0.08$. The quoted error

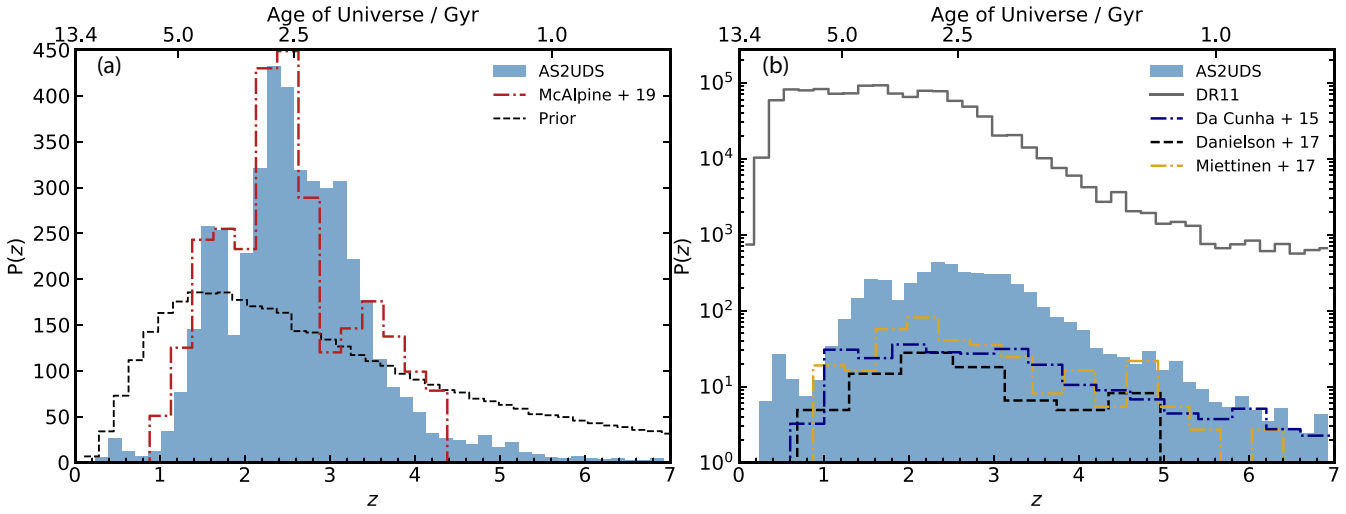


**Figure 7.** **(a)** The redshift distribution from summed likelihood distributions for our complete sample of 707 AS2UDS SMGs with a median of $z = 2.61 \pm 0.08$ (68th percentile range of $z = 1.8$–$3.4$ and 6 per cent at $z > 4$). The dashed line indicates the prior distribution. For comparison, we also overlay theoretical predictions for SMG type galaxies from McAlpine et al. (2019), who find a median redshift of $z = 2.4 \pm 0.1$. **(b)** Comparison of the AS2UDS redshift distribution to the equivalent distribution for the 99 ALESS SMGs from da Cunha et al. (2015), 52 spectroscopically identified ALESS SMGs from Danielson et al. (2017), and 124 spectroscopically identified SMGs from Brisbin et al. (2017). We also include a comparison to the field galaxies from our MAGPHYS-derived distribution for 205 910 *K*-band selected UKIDSS UDS sources with a median redshift of $z = 1.75 \pm 0.03$. The distributions are normalised by their survey area.

combines the systematic uncertainty derived from the comparison of the MAGPHYS redshifts to those for the 6719 *K*-band galaxies with spectroscopic redshifts in the UDS and the bootstrap error on the redshift distribution. The photometric redshift distribution is strongly peaked, with a 16–84th percentile range of $z = 1.8$–$3.4$ and just ∼6 per cent of SMGs at $z > 4$, while we find only five examples of SMGs at $z < 1$ even though this redshift range encompasses 57 per cent of the age of the Universe – underlining the identification of SMGs as a high-redshift population. Moreover, it is possible that some of these $z < 1$ systems are incorrectly identifications resulting from galaxy–galaxy lensing (e.g. Danielson et al. 2017; Simpson et al. 2017). In Fig. 7(a), we also overlay the predicted redshift distribution for SMGs with $S_{850} \geq 1$ mJy from the EAGLE simulation (McAlpine et al. 2019). The median redshift for the EAGLE SMGs is $z = 2.4 \pm 0.1$, with a sharp decrease above $z \sim 2.5$, driven in part by an increasing dust temperature in sources at higher redshifts. Therefore, this model distribution is a reasonable match to our observations.

In Fig. 7(b), we, next, compare our sample to the earlier study of 99 SMGs from ALESS (da Cunha et al. 2015). This sample has a single-dish 870-$\mu$m flux density limit of $S_{870} \geq 3.5$ mJy, similar to our survey and the photometric redshifts were also derived using MAGPHYS. da Cunha et al. (2015) estimate a median redshift of $z = 2.7 \pm 0.1$ for their sample, comparable to what we find, although the ALESS SMGs appear to have a shallower decline in number density beyond $z \gtrsim 3.5$–4, compared to AS2UDS. In Fig. 7(b), we also compare to the 1.1-mm selected sample of 124 SMGs in COSMOS from Miettinen et al. (2017), who have also used MAGPHYS to derive their properties. Miettinen et al. (2017) estimated a median redshift for their sample, which has a median equivalent 870-$\mu$m flux density of $4.2 \pm 0.2$ mJy (adopting $S_{870}/S_{1100} \sim 2.7$, Ikarashi et al. 2015), and a median redshift of $z = 2.30 \pm 0.13$, marginally lower than our measurement. The significance of this difference is only $\sim 2\sigma$, before considering cosmic variance or differences in the initial waveband selection, and so we conclude that the distributions are consistent.

We next compare our distribution to those from spectroscopic SMG samples. Danielson et al. (2017) provide spectroscopic redshifts for 52 ALMA-identified SMGs from ALESS with $S_{870} > 2$ mJy. This sample has a median redshift of $z = 2.4 \pm 0.1$ (see Fig. 7b), which is also similar to the median of the redshift distribution from the spectroscopic survey of radio-identified SMGs in Chapman et al. (2005). Both of these results are slightly lower than the median we derive, most likely due to a combination of selection effects: both the optical/near-infrared brightness of the counterparts (which aids spectroscopic identifications) and in the case of Chapman et al. (2005), radio biases. To assess the former bias, we note that the majority of spectroscopic SMGs in Danielson et al. (2017) have $K \lesssim 23.5$. Cutting our sample at $K \leq 23.5$ yields a median redshift of $z = 2.44 \pm 0.08$, in much better agreement to their result. Similarly, to demonstrate the potential influence of the radio identifications, if we limit our sample in AS2UDS to the 273 radio-detected SMGs then we obtain a median redshift of $z = 2.5 \pm 0.1$, which is within the uncertainty of the result from Chapman et al. (2005).

In addition, we have also run MAGPHYS on all 205 910 *K*-band selected galaxies in the field with no contamination flags to allow us to compare the properties of the ALMA SMGs directly to the less active field population in a consistent manner. The redshift distribution of the field sample is also shown in Fig. 7(b), where we derive a median redshift of $z = 1.75 \pm 0.08$.

One major benefit of the use of MAGPHYS in our analysis is the inclusion of the far-infrared and radio photometry in the SED modelling and the photometric redshift determination. Hence, we are able to investigate the redshift distribution of optical/near-infrared-faint and bright SMGs using redshifts derived in a consistent manner. The photometric redshift distribution for the SMGs which are undetected in the *K*-band ($17 \pm 1$ per cent), with $K > 25.7$ has a median redshift of $z = 3.0 \pm 0.1$, but exhibits a broad distribution with a 16–84th percentile range of $z = 2.0$–$3.8$ (see Fig. 5d). Thus, MAGPHYS predicts that the *K*-blank SMGs are typically at higher redshifts than the $K \leq 25.7$ subset (which

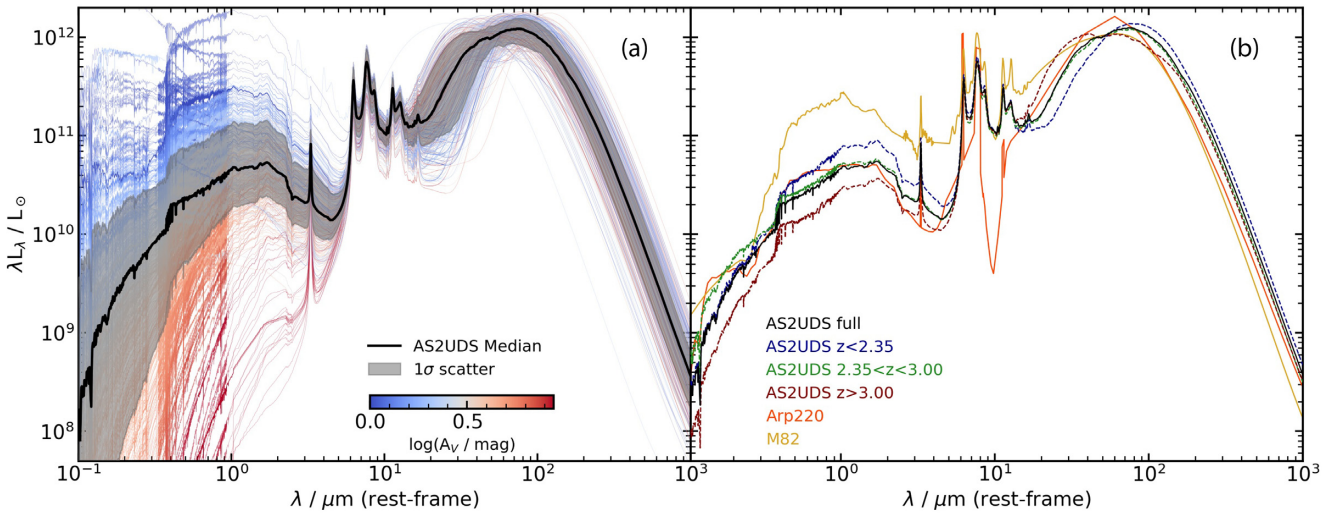


**Figure 8.** **(a)** The best-fit rest-frame SEDs of all 707 AS2UDS SMGs normalised to $L_{\rm IR} = 2 \times 10^{12}\,L_{\odot}$. The individual SEDs are coloured by their $V$-band dust attenuation. The dispersion in the flux between the SEDs in the far-infrared and sub-millimetre is ∼2–3 times, but this increases below ∼5 $\mu$m to several orders of magnitude at rest-frame wavelengths of $\lesssim$1 $\mu$m. The thick solid line shows the median composite SED from this sample and the shaded region indicates the 16–84th percentile region. We see that AS2UDS SMGs have a wide variety of colours and luminosities even in the rest-frame optical, thus it is very hard to construct a sample of star-forming galaxies, which is complete for even the most obscured examples based on the selection in the observed optical or even near-infrared wavelengths. **(b)** A comparison of AS2UDS composite to local galaxies. We plot the composite of the full sample and the SEDs for sub-samples split on redshift (dashed lines) into roughly equal-sized subsets: $z < 2.35$, $z = 2.35$–$3.00$, and $z > 3.00$. We see that high-redshift SMG's composite SED is more dust-obscured and peaks at shorter wavelength (i.e. hotter dust temperatures) than the lower-redshift composites. For comparison, we also plot the SEDs of the local galaxies M82 and Arp 220. The full AS2UDS composite appears to be much more dust obscured than M82, while it resembles Arp 220 quite closely at optical and near-/mid-infrared wavelengths. However, in the far-infrared Arp 220's SED peaks at shorter wavelengths (e.g. hotter characteristic dust temperature) than the majority of the SMGs at $z < 3$. Thus Arp 220 is a poor far-infrared template for typical SMGs, but can provide an appropriate match to the typically hotter sources seen at higher redshift ( $z > 2.5$).

have $z = 2.55 \pm 0.08$), although there is considerable overlap between the two redshift distributions and we particularly highlight that around ∼25 per cent of the near-infrared-blank SMGs lie at relatively low redshifts, $z \leq 2.5$. MAGPHYS indicates that the main reason for the difference in the $K$-band brightness of these two sub-samples is dust reddening: the $K$-detected SMGs have optical reddening of $A_V = 2.61 \pm 0.05$, but the $K$-blank SMGs exhibit much higher reddenings, $A_V = 5.33 \pm 0.18$ (and $A_V = 6.0 \pm 0.2$ for those $K$-blank SMGs at $z < 2.5$). Thus while higher redshifts is an explanation for the $K$-band faintness of many of these SMGs, that is not the case for all. As both sub-samples have similar dust mass values and far-infrared luminosities, the difference in the dust attenuation cannot be attributed to higher dust content in the $K$ band undetected SMGs. Instead, those $K$-band undetected SMGs at $z \lesssim 3$ must differ physically in the geometry of their dust and stars – either they have different viewing angles (disc-like systems viewed edge-on would result in higher dust attenuation) or these are more compact sources with higher dust column. In fact, from the sub-sample of AS2UDS SMGs with 870-$\mu$m sizes from Gullberg et al. (2019), $K$-band faint sources have smaller sizes of $R_{\rm e} = 1.60 \pm 0.10$ kpc, compared to those detected in the $K$-band, $R_{\rm e} = 1.98 \pm 0.10$ kpc (Gullberg et al. 2019). This suggests that the relative distribution of stars and dust may be the main factor in their near-infrared faintness.

### 4.2 SMG spectral energy distributions

In this section, we analyse the SEDs of the 707 ALMA SMGs in our sample in order to quantify the variation in SEDs within the SMG population, and to compare the overall properties of the SMGs to other populations, including local galaxies.

In Fig. 8(a), we plot the rest-frame SEDs of all the SMGs in our sample. We normalize the SEDs by their far-infrared luminosity (8–1000$\mu$m) to roughly the median of our sample, $L_{\rm IR} = 2 \times 10^{12}\,L_{\odot}$. Each of the SEDs is colour coded by the source's estimated $V$-band dust attenuation ($A_V$), which indicates that the galaxies with the reddest UV/optical SEDs are also the most highly obscured. Therefore, we derive a composite SED for our whole population by measuring the median value at each wavelength, and overlay this on to the individual spectra in Fig. 8(a). We also indicate the variation in the dispersion between the SEDs of SMGs as a function of wavelength. This highlights the wide variation in the rest-frame UV/optical luminosities for a far-infrared selected sample. In the wavelength range 0.1–5 $\mu$m (rest-frame UV/optical–near-infrared), the dispersion is ∼1–2 dex, with the full range of the population spanning five orders of magnitude. It should be stressed that this variety is for a population that has far-infrared luminosities in excess of $10^{12}\,L_{\odot}$ and typical stellar masses in the range $M_* \sim 10^{10}$–$10^{11}$ M$_{\odot}$. This highlights the difficulty in constructing complete samples of star-forming galaxies in the optical/near-/mid-infrared and how even near-infrared surveys are unable to identify fully mass-complete samples of strongly star-forming galaxies.

To search for evolution in the SEDs of SMGs, we split our sample into three redshift ranges containing roughly equal numbers of sources: $z < 2.35$, $z = 2.35$–$3.00$, and $z > 3.00$, with median redshifts of $z = 1.86 \pm 0.05$, $2.58 \pm 0.02$, and $3.35 \pm 0.04$, respectively. We determine the median SED of each sample and overlay these in Fig. 8(b). At $\lesssim 5\,\mu$m, we see a factor of ∼3–4 times variation in brightness of the composite SEDs between the different redshift ranges – with the lower redshift samples being consistently brighter in the rest-frame optical/near-infrared than those at higher redshifts (we see the same trend when we limit

our sample to the luminosity-selected SMGs, see Section 4.3.1). Looking at the derived median far-infrared luminosities, stellar masses, and dust reddening for the three subsets (see Section 4.3), this variation appears to be due primarily to higher far-infrared luminosities and dust temperatures at higher redshifts, along with slightly higher reddening and slightly lower stellar masses. There are few observational constraints on the shape of the SED at rest-frame $\sim$10 $\mu$m and perhaps, as a result, the three subsets show similar mid-infrared luminosities. At longer wavelengths, there is one notable difference between the SEDs, with the higher-redshift subsets peaking at progressively shorter wavelengths, indicating hotter characteristic dust temperatures (a similar trend was indicated by da Cunha et al. 2015, although sample size did not allow for confirmation), which are further discussed in Section 4.3.2.

For comparison to our SMG composites, we also show the SEDs of the local starburst galaxies M82 and Arp 220 (scaled to the same far-infrared luminosity) in Fig. 8(b). The full-sample AS2UDS SED (and all three subsets) differs significantly from M82, which is much brighter in the optical/infrared relative to the far-infrared than a typical SMG. The full SED of the SMGs is better matched to Arp 220 in the rest-frame optical/near-infrared. In the mid-infrared, Arp 220 has a strong silicate absorption feature at 9.8 $\mu$m, which falls in a poorly sampled part of our SED, where the predicted SED is dependent on the details of the model in MAGPHYS (as this wavelength is only sampled at $z < 1$ by our MIPS coverage where we have few SMGs). However, the limited mid-infrared spectroscopy available for SMGs indicates that most do not show silicate absorption as strong as seen in Arp 220 (Farrah et al. 2008; Menéndez-Delmestre et al. 2009). While in the far-infrared, the SED of Arp 220 peaks at a shorter wavelength ($\lambda_{\rm peak} \sim 60 \mu$m) than the full SMG SED, which peaks at $\lambda \sim 70$–$80 \mu$m, implying a hotter characteristic dust temperature in Arp 220. The far-infrared SED of Arp 220 is better matched to the higher redshift bins with $z > 2.5$ and the ratio $L_{\rm opt}/L_{\rm FIR}$ of Arp 220 is similar to $z \sim 2.5$ SMGs. Hence, Arp 220 template may be an appropriate template for SMG dust SED fitting in the high-redshift regime ($z > 2.5$), but is not well matched to the typical SMGs below $z \sim 2.5$.

### 4.3 Physical properties

The composite SEDs of our SMGs shown in Fig. 8 indicate potential differences between the properties of low- and high-redshift SMGs, suggesting evolutionary changes within the population (or the influence of sample selection). In the following, we investigate the physical properties of SMGs and the variation within the population, to search for evolutionary trends.

To quantify the typical properties of the SMGs we begin by constructing the stacked likelihood distributions of far-infrared luminosity ($L_{\rm IR}$), dust mass ($M_{\rm d}$), age, $V$-band dust attenuation ($A_V$), star-formation rate (SFR), stellar mass ($M_*$), and rest-frame $H$-band mass-to-light ratio ($M/L_H$), and show these in Fig. 9. We also include a histogram of the characteristic dust temperature from the modified blackbody fits ($T_{\rm d}^{\rm MBB}$), which is further explained in Section 4.3.2. By stacking the likelihood distributions, we include the uncertainties (and covariance) between the derived values, including the uncertainties in the photometric redshifts. Where applicable, in Fig. 9, we also overlay the MAGPHYS prior in order to illustrate their potential influence on our derived distributions. We note that the reliability of some of these derived quantities have been demonstrated by their correlation with the observables as discussed in Section 3.3, see also Fig. 5.

Before we discuss these derived quantities, we identify a comparison sample of local ULIRGs with which we can compare these distributions and average properties. For this purpose, we select ULIRGs from the analysis of the GAMA survey undertaken by Driver et al. (2018). They used MAGPHYS to model the multi-wavelength photometry of this sample from rest-frame UV–radio wavelengths, including both, *GALEX* far-UV and *Herschel*/SPIRE far-infrared photometry, which broadly matches the rest-frame wavelength coverage of the AS2UDS SMGs. This similarity in the multiwavelength coverage and the use of the same SED modelling code will minimize systematic uncertainties in any comparison of the properties of these local ULIRGs with high-redshift SMGs. The GAMA local ULIRG sample, we use comprises 353 galaxies that have spectroscopic redshifts of $z < 1$ (with a median of $z = 0.59$), are brighter than $r \leq 19.8$ (roughly equivalent to $H \sim 24$ at $z \sim 2.5$), have at least one PACS or SPIRE detection and have far-infrared luminosities $L_{\rm IR} > 10^{12}\,L_\odot$. For comparison, we plot the distributions of the available parameters for the local ULIRGs in Fig. 9. We similarly compare to previously published results on two high-redshift ULIRG samples from the MAGPHYS analyses of the 870-$\mu$m ALMA sample in ALESS (da Cunha et al. 2015) and a comparably sized 1.1-mm selected SMG sample in COSMOS studied with ALMA by Miettinen et al. (2017).

#### 4.3.1 *Far-infrared luminosity*

To investigate the dust properties of SMGs, we first determine their far-infrared luminosities, which is derived by integrating the rest-frame SED between 8–1000 $\mu$m. For our sample, the median far-infrared luminosity is $L_{\rm IR} = (2.88 \pm 0.09) \times 10^{12}\,L_\odot$, with a 16–84th percentile range of $L_{\rm IR} = (1.5$–$5.4) \times 10^{12}\,L_\odot$. The vast majority of our sample are classed as ULIRGs with $L_{\rm IR} = 1$–$10 \times 10^{12}\,L_\odot$, with 53 (7 per cent) being LIRGs with $L_{\rm IR} < 1 \times 10^{11}\,L_\odot$ typically at $z \sim 1.8$, and 14 (2 per cent) are HyLIRGs with $L_{\rm IR} > 1 \times 10^{13}\,L_\odot$ lying at $z \sim 3.5$. Comparison to local ULIRGs of Fig. 9(b) shows that local ULIRGs have considerably lower far-infrared luminosities with a median of $L_{\rm IR} = (1.41 \pm 0.03) \times 10^{12}\,L_\odot$ and a 16–84th percentile range of $L_{\rm IR} = (1.1$–$2.4) \times 10^{12}\,L_\odot$.

Restricting the sample at the original SCUBA-2 single-dish flux density limit of $S_{850} > 3.6$ mJy, yields 364 SMGs with a median of $L_{\rm IR} = (3.80 \pm 0.14) \times 10^{12}\,L_\odot$. In the following analysis, we also make use of a subset of our sample that is detected in at least one of the *Herschel* SPIRE bands, as these sources have more reliable measurements of their dust temperatures and hence their far-infrared luminosities. There are 475 SMGs in this SPIRE-detected subset with a median $L_{\rm IR} = (3.39 \pm 0.14) \times 10^{12}\,L_\odot$ and a 68th percentile range of $L_{\rm IR} = (1.7$–$5.9) \times 10^{12}\,L_\odot$ and lying at a median redshift of $z = 2.48 \pm 0.08$ (68th percentile range of $z = 1.8$–$3.2$).

The median far-infrared luminosity of our SMGs is comparable with that derived for the sample in ALESS $L_{\rm IR} = (3.7 \pm 0.1) \times 10^{12}\,L_\odot$ for a similar 870-$\mu$m flux density limit (da Cunha et al. 2015), and also comparable to the median far-infrared luminosity of the 1.1-mm selected SMG sample from Miettinen et al. (2017)[1], who derive a median of $L_{\rm IR} = (4.0 \pm 0.3) \times 10^{12}\,L_\odot$ for a sample with an equivalent 870-$\mu$m flux density range of 1.5–20 mJy (adopting $S_{870}/S_{1100} \sim 1.8$, equivalent to a $\nu^{-2.5}$ spectral index, based on the average flux ratio of AS2UDS SMGs

[1]Note that the errors on Miettinen's values are the 16–84th percentile ranges, rather than the uncertainty in the median value.

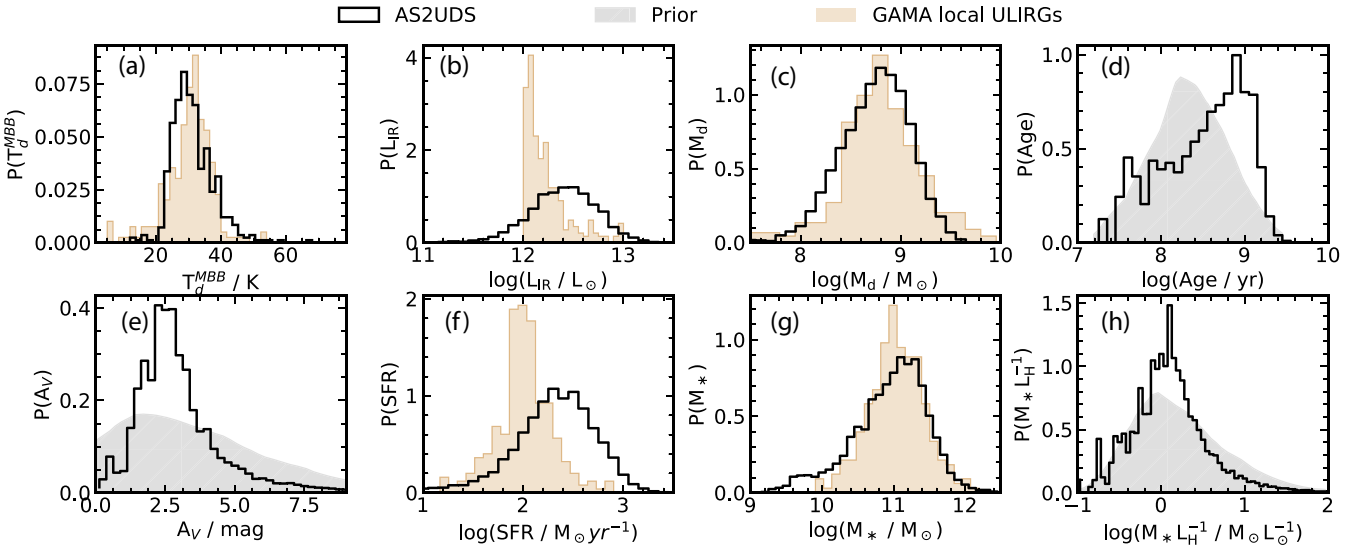


**Figure 9.** Distributions of the physical properties of the AS2UDS SMG population predicted by MAGPHYS or derived directly from the SEDs. To demonstrate that the posterior likelihood distributions are not affected by the model priors, we overlay them where applicable. For comparison, the available properties from a sample of local ULIRGs from the GAMA survey (Driver et al. 2018), selected to have $L_{\rm IR} > 10^{12}\,L_{\odot}$ and $z < 1$, is also shown. In each panel, we plot the median stacked likelihood distribution from combining the PDFs of the individual SMGs. From the top left the distributions show: **(a)** optically thin modified blackbody temperature ($T_{\rm d}$) for those galaxies that are detected in at least one SPIRE band; **(b)** far-infrared luminosity ($L_{\rm IR}$); **(c)** dust mass ($M_{\rm d}$); **(d)** mass-weighted age; **(e)** the $V$-band dust attenuation ($A_V$); **(f)** star-formation rate; **(g)** stellar mass ($M_*$); **(h)** rest-frame $H$-band mass-to-light ratio ($M/L_H$). We see broad similarities between the properties of the SMGs and the local ULIRGs, with the exception that the SMGs (which have much higher volume densities than the comparably luminous galaxies at $z < 1$) are typically more luminous in the far-infrared and have correspondingly higher star-formation rates.

with published 1.1-mm photometry from ALMA in Ikarashi et al. 2017).

To illustrate the evolution in our sample, we plot the variation of far-infrared luminosity with redshift for the AS2UDS SMGs in Fig. 10(a). We include in this plot only those SMGs which have at least one SPIRE detection. The SMGs show a trend in redshift for the brightest luminosities that is roughly reproduced by evolution of the form $L_{\rm IR} \propto (1+z)^{\gamma}$, with $\gamma \sim 4$, consistent with the behaviour previously claimed for luminous dusty galaxies at $z < 2$ (e.g. Béthermin et al. 2011). We also need to consider the influence of our sample selection on this trend and so we also show in Fig. 10(a) the far-infrared luminosity of a source with a dust SED modelled by a modified blackbody with a temperature of $T_{\rm d} = 32$ K (the median for this sample) and an 870-$\mu$m flux density $S_{870} = 1$ mJy, which is the typical completeness level of our ALMA maps. We see that due to the negative $k$-correction the resulting far-infrared luminosity limit is almost constant out to $z \sim 6$. In addition, we overlay a selection function for the same $T_{\rm d} = 32$ K model with the additional constraint that the SED must be detected in at least one SPIRE band at 250, 350, or 500 $\mu$m, which is the requirement placed on the subset of the AS2UDS sample we are plotting. We see that this selection results in an increasing far-infrared luminosity limit at higher redshifts, which reproduces the behaviour we see in our sample. Hence, the apparent deficit in Fig. 10(a) of lower luminosity sources (with $L_{\rm IR} \lesssim 2$–$3 \times 10^{12}\,L_{\odot}$) at $z \gtrsim 2.5$–3, can be accounted for by the sample selection. While the SPIRE-detected subset of our SMG sample is biased towards more luminous sources at higher redshifts, we retain this selection because these have more robust estimates of their far-infrared properties. However, to control for the resulting bias in far-infrared luminosity with redshift, and so assess evolutionary trends, we will also exploit our large sample to construct an unbiased sample of SMGs at $z = 1.5$–4, selected to lie in a narrow range of far-infrared luminosity [ $L_{\rm IR} = (4$–$7) \times 10^{12}\,L_{\odot}$], where our sample is complete with respect to the SPIRE detection limits (this selection is shown by the rectangle plotted in Fig. 10a).

### 4.3.2 *Characteristic dust temperature*

Although MAGPHYS can estimate a characteristic dust temperature, it is derived from a complex calculation involving five free parameters, which describe the temperature and luminosity contributions from the warm (birth cloud) and cold (diffuse ISM) components. The far-infrared SEDs of our sources are covered by at most six photometric bands, thus we choose to adopt a simpler, more conservative approach and fit modified blackbody functions to the available *Herschel* PACS and SPIRE, and ALMA 870-$\mu$m photometry. This approach also has an added advantage that the dust SEDs of the comparison samples can be fitted in a very similar way, allowing for more reliable comparison, free from systematic uncertainties resulting from the fitting procedures. We use a modified blackbody function of the form

$$S_{\nu_{\rm obs}} \propto (1 - {\rm e}^{-\tau_{\rm rest}}) \times B(\nu_{\rm rest}, T), \quad (1)$$

where $B(\nu_{\rm rest}, T)$ is the Planck function, $\tau_{\rm rest}$ is the frequency-dependent optical depth of the dust of the form $\tau_{\rm rest} = \left(\frac{\nu_{\rm rest}}{\nu_0}\right)^{\beta}$, $\nu_0$ is the frequency at which optical depth is equal to 1 and $\beta$ is the dust emissivity index. We adopt $\beta = 1.8$ as used in previous SMG studies and consistent with the finding for local star-forming galaxies (Planck Collaboration XIX 2011; Clemens et al. 2013; Smith et al. 2013). Making the assumption that the region from which the dust emission originates is optically thin, thus $\nu_0 \gg \nu_{\rm rest}$,

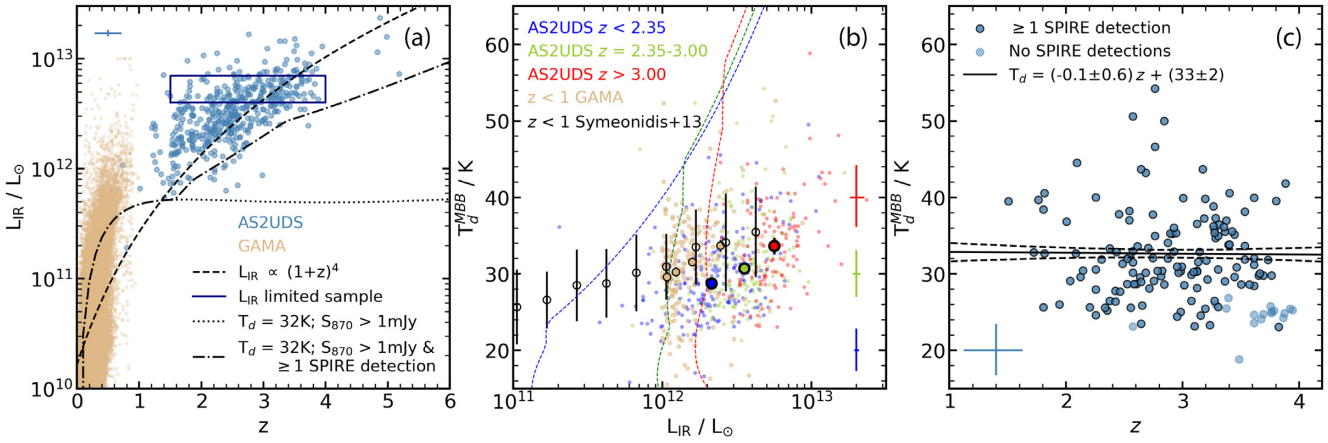


**Figure 10.** **(a)** The far-infrared luminosity of the AS2UDS SMGs as a function of redshift for those sources, which have at least one SPIRE detection. The dashed line shows the luminosity evolution according to $L_{\rm IR} \propto (1+z)^4$. The dotted line denotes the selection function of an $S_{870} \gtrsim 1$ mJy SMG for a modified blackbody dust SED with the median dust temperature of the sample, $T_{\rm d} = 32$K. While the dot–dashed line shows the selection including the requirement that the dust SED includes at least one detection above the flux limits of the available SPIRE observations at 250, 350, or 500 $\mu$m. We see that the latter model provides a reasonable description of the variation of the lower boundary in $L_{\rm IR}$ with redshift which we observe. The rectangle shows the limits of the unbiased, luminosity-limited subset we use below to test evolutionary trends. We also show the low-redshift ( $z < 1$) sample of far-infrared detected galaxies from the GAMA survey (Driver et al. 2018) and note that we compare to the $\geq 10^{12} L_\odot$ subset of these. **(b)** The temperature–luminosity relation of those AS2UDS SMGs with at least one SPIRE detection, split into three redshift bins: $z < 2.35$, $z = 2.35$–3.00, and $z > 3.00$. We highlight the median values of each of the redshift sub-samples with their associated uncertainties. The selection function of AS2UDS sources with at least one SPIRE detection and $S_{870} \geq 1$ mJy at redshifts of $z = 1$, 2.35, and 3.00 are plotted. We see an apparent evolution of the far-infrared luminosities and dust temperatures of the SMGs, which is roughly parallel to the trend seen within each redshift slice and does not appear to be influenced by the selection limits. For comparison, we plot the median values from local $z = 0$–1 SPIRE-selected LIRGs and ULIRGs from (Symeonidis et al. 2013) and the distribution with the median values derived for the ULIRGs from the GAMA survey. These show that the 870-$\mu$m selected SMGs are $3 \pm 1$ K cooler at fixed $L_{\rm IR}$ than far-infrared luminous galaxies at $z < 1$. **(c)** The variation in dust temperature with redshift for our complete luminosity-limited SMG sample, which lies within the rectangle plotted in panel (a) [ $L_{\rm IR} = (4$–$7) \times 10^{12}\, L_\odot$ and $z = 1.5$–4.0]. No evolution is seen in the dust temperature at fixed luminosity across this redshift range.

equation (1) simplifies to

$$S_{\nu_{\rm obs}} \propto \nu_{\rm rest}^{\beta} \times B(\nu_{\rm rest}, T). \quad (2)$$

The dust temperature derived using the optically-thin approximation does not represent the true temperature of the dust emission regions, as Riechers et al. (2013) and Simpson et al. (2017) and others have shown that the emission from SMGs is, on average, optically thick at $\lambda_0 \lesssim 75\ \mu$m (we explore this further in Section 4.3.6). Thus, this estimate is only a simplified model that we will refer to as the characteristic dust temperature. The best-fit temperature is acquired by fitting this modified blackbody function using a Markov Chain Monte Carlo sampler (see Simpson et al. 2017).

The resulting characteristic temperature distribution for our SPIRE-detected SMGs is shown in Fig. 9(a). Comparing the dust temperatures for the SMGs from the modified blackbody fits with the predicted characteristic dust temperature from MAGPHYS, we find a typical fractional difference of $(T_{\rm d}^{\rm MBB} - T_{\rm d}^{\rm MAGPHYS})/T_{\rm d}^{\rm MBB} = -0.28 \pm 0.01$. The median characteristic dust temperature for our ALMA SMGs with at least one SPIRE detection is $T_{\rm d}^{\rm MBB} = 30.4 \pm 0.3$ K with a 68th percentile range of $T_{\rm d}^{\rm MBB} = 25.7$–37.3 K, this is shown in Fig. 9(a). For comparison, the same method to derive characteristic dust temperature was applied to the local ULIRGs sample. The median temperature of the local ULIRGs sample is slightly higher but within error range to SMGs, with a median characteristic dust temperature of $T_{\rm d}^{\rm MBB} = 31.1 \pm 0.4$ K. However, we stress that the typical far-infrared luminosity of the GAMA ULIRGs is a factor of 2–3 times lower than the SMGs and, as we discuss below, when we compare $L_{\rm IR}$-matched samples then the local ULIRGs, on average, hotter than the SMGs.

Due to the similarities in their physical properties (e.g. stellar mass and dust mass, see Fig. 9), SMGs have been proposed to be analogues of the local ULIRGs. Indeed, as seen in Fig. 8(b), the SED for at least one archetypal ULIRG, Arp 220, shares some similarities with the higher-redshift SMGs. Local ULIRGs exhibit a dust temperature–luminosity relation, so we now investigate the correlation between far-infrared luminosity and characteristic dust temperature for the AS2UDS SMGs in Fig. 10(b). We find a positive correlation between far-infrared luminosity and dust temperature for the AS2UDS SMGs similar to previous SMG studies (e.g Magnelli et al. 2012; Symeonidis et al. 2013; Swinbank et al. 2014). Moreover, we see a correlation between luminosity and temperature within each of the three redshift subsets and a similar trend between the medians of the three subsets. We also show in Fig. 10(b) the selection functions for three redshifts that illustrate the selection of our 870-$\mu$m observations as a function of redshift, far-infrared luminosity, and dust temperature. Comparing these selection boundaries to our SPIRE-detected samples indicates that they should not be strongly influencing the correlations we observe. Indeed, when we look at the variation of $T_{\rm d}$ with $L_{\rm IR}$ for our unbiased luminosity-limited subsample, we find a similarly strong $L_{\rm IR}$–$T_{\rm d}$ trend, $\Delta T_{\rm d} \sim 12\ \Delta \log_{10}(L_{\rm IR})$.

Fig. 10(b) also shows the $L_{\rm IR}$–$T_{\rm d}$ distribution for $z = 0$–1 SPIRE-selected LIRGs and ULIRGs from Symeonidis et al. (2013) and the $z < 1$ ULIRGs from the GAMA survey. These show a significant offset in dust temperature at a fixed luminosity relative to the SMGs: $\Delta T_{\rm d} = 3 \pm 1$ K for samples with $L_{\rm IR} \sim 2$–$4 \times 10^{12}\, L_\odot$. This comparison ought not to be influenced by the selection limits on our SMG sample, although we have not modelled those for the local samples. We note, that the temperature difference between the samples is

comparable with the uncertainty derived from EAGLE comparison, however, this is a systematic offset at all luminosity bins. So we tentatively conclude that at a fixed luminosity the AS2UDS SMGs appear to show cooler median dust temperatures than the local samples, possibly due to more compact dust distribution in local ULIRGs (Iono et al. 2009; Wilson et al. 2014).

The median values at each redshift slice in Fig. 10(b) may suggest a trend of characteristic dust temperature with redshift. Thus, we select the unbiased luminosity-limited sample sources and plot the variation of their dust temperature with redshift in Fig. 10(c). No evolution in the dust temperature at a fixed luminosity is seen in this redshift range.

#### 4.3.3 Star-formation rate

Far-infrared luminosity traces dust-obscured star formation; thus, it is possible to infer star-formation rates using the conversion from $L_{\rm IR}$ given in Kennicutt (1998). Models in MAGPHYS, however, allow dust heating by old stellar populations and thus the model also estimates the star-formation rate in the optical regime after accounting for dust attenuation. Even though a wide range of model star-formation histories was included, we find a good correlation between the far-infrared and MAGPHYS derived star-formation rates for the SPIRE-detected subset, with a dispersion of $\sim$25 per cent estimated from the 16–84th percentile range. We determine a median star-formation rate of SFR $= 290 \pm 14\,{\rm M}_{\odot}\,{\rm yr}^{-1}$ with a 68th percentile range of SFR $= 124$–$578\,{\rm M}_{\odot}\,{\rm yr}^{-1}$ (based on the SPIRE-detected subsample) that is consistent with da Cunha et al. (2015), who found SFR $= 280 \pm 70\,{\rm M}_{\odot}\,{\rm yr}^{-1}$ for the ALESS sample. In comparison to the local ULIRG sample from GAMA, the typically higher far-infrared luminosities of our SMGs suggest higher star-formation rates, which is indeed the case, with the former having a median star-formation rate of $108 \pm 4\,{\rm M}_{\odot}\,{\rm yr}^{-1}$ (see Fig. 9f).

We investigate the evolution of star-formation rate in the SMGs with redshift in Fig. 11(a). We also include the local ULIRGs sample, and as noted earlier, we observe that local ULIRGs typically have lower star-formation rates than seen in the SMGs in our sample. The best-fit line with a gradient of d(log $_{10}$ (SFR))/d $z = 0.22 \pm 0.02$ indicates a significant $11\sigma$ trend. However, as seen in Section 4.3.1, our selection affects the trends seen with redshift. When we limit our sample to the unbiased luminosity-selected sample, we observe no significant SFR evolution with d(log $_{10}$ (SFR))/d $z = 0.05 \pm 0.03$, as seen in Fig. 11(a). We compare the star-formation rates of SMGs at different redshifts with the UKIDSS DR11 field sample. For this comparison, we select field galaxies that have stellar masses above the 16th percentile value of the AS2UDS sample ( $M_* > 3.5 \times 10^{10}\,{\rm M}_{\odot}$). The shaded regions show the 16–84th percentile ranges of the SMGs and the field sample in their respective colours. As seen in Fig. 11(a), the typical SMGs in our sample have significantly higher star-formation rates than a mass-selected sample at all redshifts probed.

#### 4.3.4 Stellar emission properties

Next, we look at the physical properties inferred from the stellar emission that typically dominates the rest-frame UV/optical/near-infrared region of the SED of galaxies. We investigate the derived stellar masses as it is one of the most fundamental properties of SMGs. Robust stellar masses can provide tests of the evolutionary links between the SMGs and field galaxies, such as determining the fraction of massive galaxies which may have evolved through an SMG-like phase.

The median stellar mass of the full AS2UDS sample is $M_* = (12.6 \pm 0.5) \times 10^{10}\,{\rm M}_{\odot}$ and we see no strong variation in this with redshift, as shown in Fig. 11(b). Our median stellar mass is in good agreement with the 1.1-mm selected sample from Miettinen et al. (2017), who find median a stellar mass of $M_* = 12^{+19}_{-9} \times 10^{10}\,{\rm M}_{\odot}$ and also see no evolution with redshift in their sample. However, our derived mass is higher than the $M_* = (8.9 \pm 0.1) \times 10^{10}\,{\rm M}_{\odot}$ found by da Cunha et al. (2015). Limiting both samples to the same 870-$\mu$m flux limit does not eliminate this disagreement, but we note that due to the broad distribution of $P(M_*)$ there is a wide range of acceptable stellar masses for our sample, the 16–84$^{\rm th}$ percentile range for AS2UDS being $5.9$–$22 \times 10^{10}\,{\rm M}_{\odot}$ (see Fig. 9g). This difference may, therefore, be due to either sampling statistics or cosmic variance.

When comparing with local ULIRGs (see Fig. 9g), we see no significant differences in the distributions of stellar mass, even though the Universe is roughly three times older at the epoch of the GAMA population than it was at the era when the SMGs peak. However, the $r = 19.2$ mag limit of GAMA is $\sim$1.5 mag brighter than our equivalent $H$-band limit (at $z \sim 2.5$), thus GAMA may be biased to higher stellar masses.

Next, we investigate the attenuation of stellar emission at UV to near-infrared wavelengths, which, in MAGPHYS, is estimated using a two-component model of Charlot & Fall (2000). The two components model the effective attenuation in the $V$-band from dust in both stellar birth clouds and in the diffuse ISM. The median $V$-band dust attenuation derived for the AS2UDS sample is $A_V = 2.89 \pm 0.04$ mag with a 68th percentile range of $A_V = 1.89$–$4.24$ mag. The posterior likelihood distribution is significantly more peaked than the prior (see Fig. 9e). Moreover, the prediction, shown in Fig. 6, that the vast majority of SMGs are indeed far-infrared luminous based solely on the MAGPHYS modelling of the $U-8.0\,\mu$m SEDs provides strong support that the derived $A_V$ have diagnostic power as this parameter is the main driver of that prediction. As expected, we find that optically brighter SMGs (those with more than three detections in the optical/near-infrared bands) have $A_V = 2.5 \pm 0.2$ mag, while the optically fainter examples (fewer than four detections) have $A_V = 3.6 \pm 0.2$ mag. We note that this estimate of reddening is an angle averaged dust attenuation, which is measured by the classical definition – comparing the intrinsic and obscured $V$-band magnitudes. Even though they are lower limits on the true total extinction (as they give lower weight to more extinct emission), they are still significant and underline the difficulty of constructing robust mass-limited samples of high-redshift galaxies in the face of the significant dust obscuration found in some of the most active and massive examples.

We compare our sample to the 99 ALESS SMGs from da Cunha et al. (2015), which yields a median $A_V = 1.9 \pm 0.2$ mag (restricting this analysis to the subset of 52 of these SMGs with spectroscopic redshifts from Danielson et al. 2017 does not change this estimate). This is significantly lower than the median reddening derived for the AS2UDS galaxies, although both distributions span a similar range in $A_V$. This difference does not seem to relate to differences in the 870-$\mu$m flux density limits, redshift distributions or stellar masses of the two samples. Instead, it appears to reflect a population of highly obscured, $A_V \gtrsim 3.5$, SMGs at $z \lesssim 3.0$, which are seen in AS2UDS, but are absent in ALESS.

Finally, to measure the overall age of a given source, MAGPHYS outputs a mass-weighted age, which depends strongly on the form of the star-formation history. We find a median age for our SMGs of

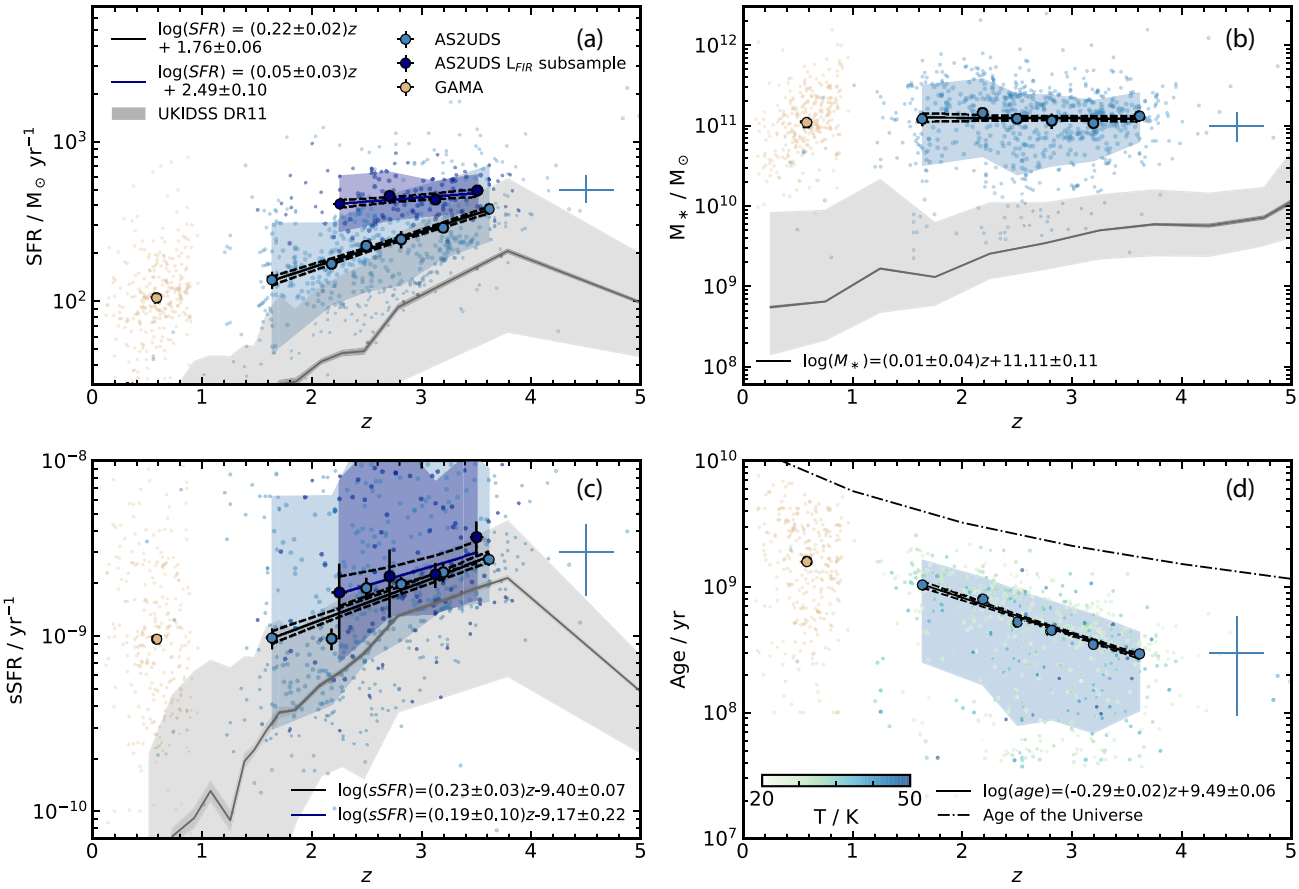


**Figure 11.** The evolution of the MAGPHYS stellar parameters with redshift. In each panel, the large circles show the median in bins with the equal number of sources. The sample of $z < 1$ ULIRGs from the GAMA survey and their median is similarly shown. The solid line shows the best-fit to the binned medians and the dashed lines show the associated uncertainty. The median error on any individual source is shown on the right-hand side of each panel. The 16–84th percentile range of the given property is shown in blue-shaded regions. In panels (a), (b), and (c), we plot the median trend derived from the UKIDSS DR11 field population with the error on the median in the grey-shaded region and their associated 16–84th percentile range indicated as the light shaded region. **(a)** Star-formation rate versus redshift for the SPIRE-detected SMG sample and the unbiased luminosity-selected sub-sample. As with the variation of $L_{\rm IR}$ with redshift shown earlier, there is a highly significant increase in median star-formation rate with redshift within our sample, however, when the sample is limited to the unbiased luminosity-selected sub-sample this trend disappears. In comparison to a *K*-selected sample, we again see those typical SMGs are significantly above the median trend seen in 'normal' star-forming field galaxies at all redshifts. **(b)** Stellar mass versus redshift for the AS2UDS SMGs. We see no strong variation in the estimated stellar mass of the SMGs with redshift, with this extending down to the $z < 1$ ULIRGs. In comparison to the *K*-band selected sample, SMGs have significantly higher stellar masses at all redshifts. **(c)** Specific star-formation rate versus redshift, which shows a 7.5 $\sigma$ trend of d(log $_{10}$ (sSFR))/d $z$ = 0.23 ± 0.03. This trend weakens as we limit the sample to the unbiased luminosity-selected subset. SMGs lie above the median of a *K*-band selected sample out to $z \sim$ 3–4. **(d)** Mass-weighted age versus redshift. The median derived age for the SMGs is (4.6 ± 0.2) × 10 $^{8}$ yr and the best-fit line has a gradient of d(log $_{10}$ (Age $_{\rm m}$))/d $z$ = -0.29 ± 0.02. The AS2UDS points are coloured by dust temperature, showing that the strength of this trend could be partly due to the model assigning younger ages to galaxies with higher dust temperatures (and far-infrared luminosities), which are typically found at higher redshifts. The dashed line shows the maximum formation redshift allowed by MAGPHYS, which corresponds to a cosmological lookback time of 13.4 Gyrs at $z \sim$0.

Age$_{\rm m}$ = (4.6 ± 0.2) × 10$^{8}$ yr. We note that the posterior likelihood distribution differs significantly from the prior shown in Fig. 9(d), suggesting the model is varying this parameter when fitting the SED. We return to compare the mass-weighted ages of the SMGs to other estimates of age from the derived physical properties in Section 5.1.1.

### *4.3.5 Comparison with the 'main sequence'*

We wish to relate the SMG population to the more numerous and less active and massive galaxies seen in the field population. One tool to do this is to assess the distribution of this population on the stellar mass versus star-formation rate plane, in particular, the relative position of the SMGs compared to the broad relation between star-formation rate and stellar mass exhibited by star-forming galaxies (the so-called 'main sequence', Daddi et al. 2007) – as assessed through their relative specific star-formation rates (sSFR = SFR/$M_*$). Specific star-formation rates significantly above the median trend of the field population have been argued to be a signature of starburst activity, potentially resulting from galaxy–galaxy mergers and interactions, which enhance the star-formation rates of galaxies and so increase their sSFR (Magnelli et al. 2012). Alternatively, it may be possible for galaxies to achieve high star-formation rates without such triggers, merely through significant gas accretion – enabling high SFR systems to inhabit the high-mass end of the sequence of normal star-forming galaxies (Davé et al. 2010). Alternatively, samples of highly star-forming

galaxies could represent a heterogeneous mix of these two classes of systems, encompassing both physical processes (e.g. Hayward et al. 2011; Narayanan et al. 2015; McAlpine et al. 2019).

In Fig. 11(c), we look at the variation with redshift in the sSFR estimates for the SMGs compared to the less-active field population (derived in the same manner with robustness tested in Section 3.3.1). We observe a modest positive correlation between specific star-formation rate and redshift for the SMGs. As shown in Fig. 11(a), we find no evolution of stellar mass with redshift for our SMG sample, thus this trend is set by the variation in the star-formation rate. However, as we showed before, the latter is due to selection effects on far-infrared luminosity. Indeed, when we limit our sample to the unbiased luminosity-selected sample, we find no significant trend in sSFR with redshift, with the SMG population, on average, spanning an order of magnitude in sSFR at all redshifts.

We compare the SMGs to the distribution from our MAGPHYS analysis of the *K*-band selected sample of galaxies in the UDS field, which we take to represent the 'main sequence' (consistent with Tasca et al. 2015). For a consistent comparison, we select field galaxies that have stellar masses above the 16th percentile of the AS2UDS sample ($M_* \gtrsim 3.5 \times 10^{10}\,\mathrm{M}_\odot$). Fig. 11(c) demonstrates that field population has lower median sSFR values at all redshifts, but the difference between two populations decreases with redshift and SMGs lie close to the evolved 'main sequence' at $z \gtrsim 3.5$, at which point the number density of SMGs in our sample is declining rapidly (see also da Cunha et al. 2015). This suggests that the bulk of the SMG population, we detect brighter than $S_{870} \sim 1$ mJy have specific star-formation rates which put them above the 'main sequence' at their respective redshifts. Indeed, using the sources in our 16–84th percentile range of $z = 1.8$–$3.4$, we find that $82 \pm 4$ per cent lie above the 'main sequence' defined by the *K*-band selected sample, with $34 \pm 3$ per cent lying more than a factor of four above it (the arbitrary definition of a 'starburst').

### 4.3.6 Dust and gas masses

We now investigate the properties of dust and gas in SMGs. Dust mass estimates, together with properties calculated from stellar emission, allow us to assess how efficient SMGs are at forming stars from gas, which, in turn, can provide a constraint on the lifespan of the sub-millimetre luminous phase in these systems.

We derive a median dust mass for the full AS2UDS sample of $M_\mathrm{d} = (6.8 \pm 0.3) \times 10^8\,\mathrm{M}_\odot$ with a 68th percentile range of $M_\mathrm{d} = (3.0$–$12.6) \times 10^8\,\mathrm{M}_\odot$, which broadly agrees with the median estimated for the ALESS sample: $M_\mathrm{d} = (5.6 \pm 0.1) \times 10^8\,\mathrm{M}_\odot$ (da Cunha et al. 2015). Similarly, Miettinen et al. (2017) estimate a median dust mass of $M_\mathrm{d} = 10^{+6}_{-5} \times 10^8\,\mathrm{M}_\odot$ for their 1.1-mm selected SMG sample, which again is similar to our measurement. It is expected that dust mass will be closely correlated with sub-/millimetre flux density, hence this agreement may simply reflect the roughly similar effective flux density limits of the single-dish surveys followed-up in these three ALMA studies.

Indeed, in Fig. 12(a) we see a relatively tight lower boundary to the distribution (for the $S_{870} \geq 3.6$-mJy sample this corresponds to $M_\mathrm{d} \geq 5 \times 10^8\,\mathrm{M}_\odot$), confirming that 870-$\mu$m flux density selection provides an approximately uniform dust mass selection across a wide redshift range. The ratio of dust mass to 870-$\mu$m flux density gives a simple conversion between the observable and the intrinsic property of $\log_{10}[M_\mathrm{d}(\mathrm{M}_\odot)] = (1.20 \pm 0.03) \times \log_{10}[S_{870}(\mathrm{mJy})] + 8.16 \pm 0.02$, with a $1\sigma$ dispersion of $\sim$30 per cent, within the error derived from EAGLE comparison. We also see only a moderate increase in dust mass with redshift in our sample, corresponding to $\sim$30 per cent across the redshift range $z = 1.8$–$3.4$. This is qualitatively consistent with the variation in median redshift with $S_{870}$ flux density found by Stach et al. (2019) – who demonstrated that SMGs from AS2UDS, which are brighter at 870 $\mu$m, on average, lie at higher redshifts. However, this trend weakens when we consider only the unbiased luminosity-selected sub-sample (see Fig. 12a).

We note that if the gas-to-dust ratio of this strongly star-forming population does not vary significantly over this redshift range, then our 870-$\mu$m selection will correspond to a similarly uniform selection in terms of molecular gas mass. The conversion factor from dust mass to molecular gas mass has been derived for a small sample of high-redshift SMGs with CO(1–0) observations, yielding a gas-to-dust ratio, $\delta_\mathrm{gdr}$, of $\sim$100 (Swinbank et al. 2014) similar to that estimated for Arp 220, which we adopt for our study. We note that the gas-to-dust ratio is expected to vary as a function of metallicity and hence potentially stellar mass and redshift. However, the lack of reliable gas-phase metallicities for SMGs means we choose to adopt a fixed ratio in our analysis.

We see an order-of-magnitude range in both $M_\mathrm{d}$ and $L_\mathrm{IR}$ across our sample in Fig. 12(b) with a weak correlation between these two parameters, although there is a clear variation across the distribution in terms of dust temperature. We also overlay on to the figure lines corresponding to constant gas depletion (or star-formation efficiency), which we estimate assuming half of the gas is available to form stars (the other half being expelled) (Pettini et al. 2002):

$$\tau_\mathrm{dep} \sim \frac{0.5 \times M_\mathrm{gas}}{\mathrm{SFR}}. \tag{3}$$

We see that the population spans a range of a factor of 6 in gas depletion timescale, from 50 to 300 Myr with a median of $146 \pm 5$ Myr. Hence, the estimated length of the SMG phase, assuming the sources are typically seen half-way through this period, is $\sim$300 Myr. We also observe that the SMGs with the hottest characteristic dust temperatures show the shortest gas depletion timescales (or equivalently the highest star-formation efficiencies).

As a corollary to the $L_\mathrm{IR}$–$M_\mathrm{d}$ plane, we also plot in Fig. 12(c) the ratio of $L_\mathrm{IR}$ (as a simple observable linked to star-formation rate) and $M_\mathrm{d}$ (as a proxy for gas mass) in our sample as a function of redshift. This ratio reflects the expected gas depletion timescale and we see that it declines by a factor of $\sim$2 between $z = 1.5$ and 4.0 from $\sim$200 to $\sim$50 Myrs (da Cunha et al. 2015 analysis of the ALESS sample shows very similar behaviour). However, as seen in Fig. 12(c), when we restrict our analysis to the unbiased, luminosity-limited subset this trend weakens, suggesting that it is driven primarily by the incompleteness in $L_\mathrm{IR}$, and thus star-formation rate, with redshift – rather than a fundamental variation in the gas depletion timescale with redshift.

We can also compare the estimates of the dust and stellar masses for the SMGs. For our full SMG sample, we derive a median dust to stellar mass ratio of $M_\mathrm{d}/M_* = (5.4 \pm 0.2) \times 10^{-3}$ with a 16–84th range of 0.0028–0.0131 and little change with redshift, while for the GAMA ULIRGs we estimate $M_\mathrm{d}/M_* = (11 \pm 2) \times 10^{-3}$. At the upper end of our observed range, these values are above the expected yields for dust from SNe and AGB stars (Calura et al. 2017) unless the IMF is biased to high-mass stars (Baugh et al. 2005; Zhang et al. 2018) or that much of the dust grain growth in these systems occurs in the ISM (Draine 2009; Burgarella et al. 2020), which might be a result of the high ISM densities found in

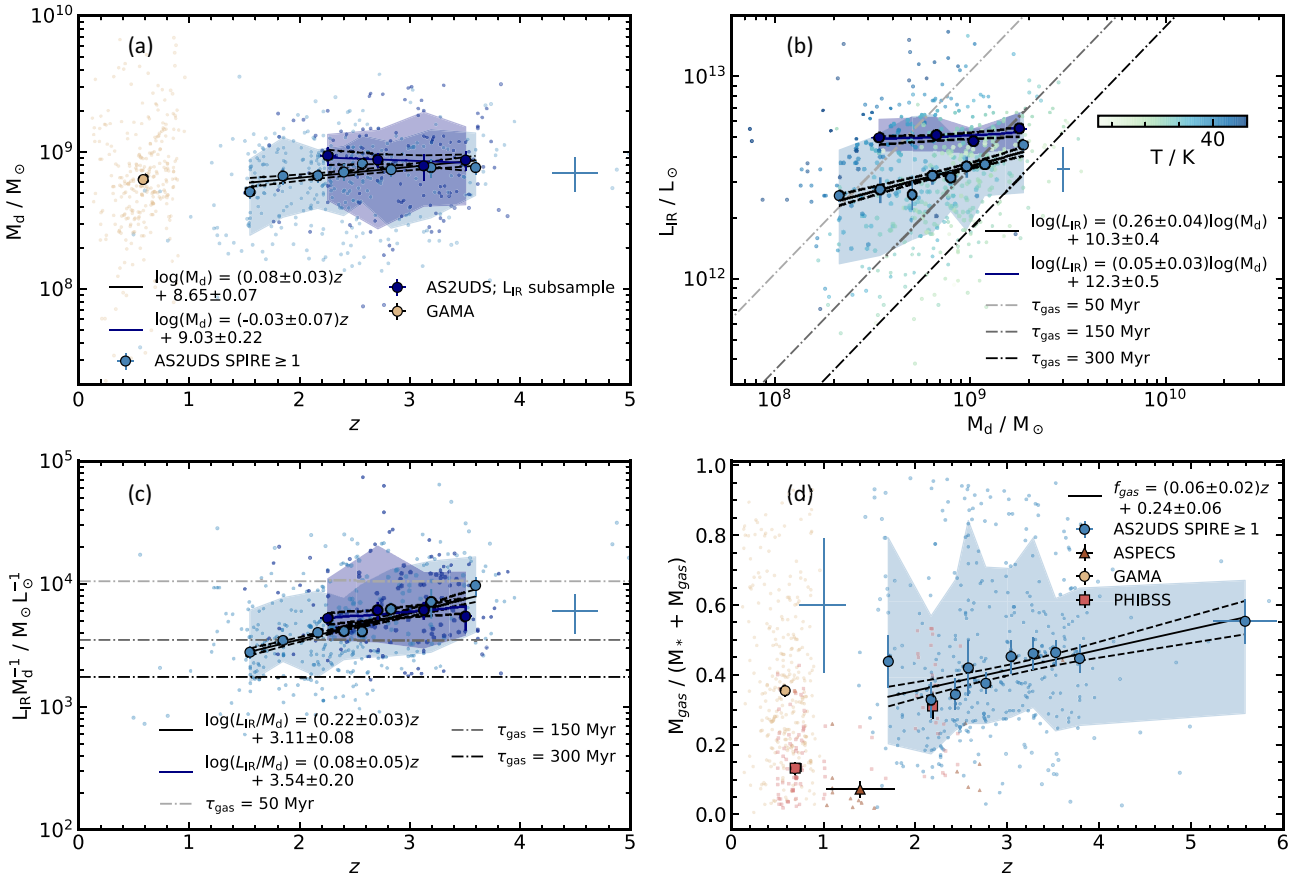


**Figure 12.** The redshift evolution of the MAGPHYS predicted dust properties for those AS2UDS SMGs detected in at least one SPIRE band and the unbiased luminosity-selected sub-sample of SMGs. In each panel, the large circles show the binned median in bins with equal numbers of sources, the solid line shows the best-fit line to the binned data, and the dashed lines show the associated uncertainty. The 16–84th percentile range of the given property is shown in blue-shaded regions. The sample of $z < 1$ ULIRGs from the GAMA survey and their median is similarly shown in panels (a) and (d). The median error on any individual AS2UDS source is shown in each panel. **(a)** Dust mass as a function of redshift. We see that the 870-$\mu$m selection of our joint S2CLS/ALMA survey yields a uniform selection in dust mass with redshift over the full redshift range probed by our study, with no evolution seen in the median dust mass with redshift. **(b)** Dust mass versus far-infrared luminosity. Our sample spans an order-of-magnitude range in both $L_{IR}$ and $M_d$ with a weak positive correlation with a slope of $0.26 \pm 0.04$. We note that the dispersion is driven in part by variations in dust temperature, whereby SMGs that have lower temperatures are observed to have higher dust masses for a given far-infrared luminosity. We also indicate lines of constant gas depletion. **(c)** The ratio of far-infrared luminosity to dust mass, a proxy for star-formation efficiency (or the inverse of gas depletion timescale), versus redshift. We again indicate lines of constant gas depletion. We see a strong increase in star-formation efficiency with increasing redshift within our SPIRE-detected sample with a gradient of $0.22 \pm 0.03$. However, this trend weakens significantly if we restrict our analysis to the unbiased, luminosity-limited subset suggesting that it is driven primarily by the variation in $L_{IR}$ or star-formation rate with redshift. **(d)** Gas fraction as a function of redshift. We derive a median gas mass fraction of $f_{gas} = 0.41 \pm 0.02$ with a 68th percentile range of $f_{gas} = 0.24$–$0.72$ and we see modest evolution of this quantity with redshift, with a gradient of $0.06 \pm 0.02$. For comparison, we overlay results from the ASPECS blind CO-survey from Aravena et al. (2019) and the CO-detected typical star-forming galaxies at $z \sim 1$–$3$ from Tacconi et al. (2018).

the SMGs (Swinbank et al. 2011; Simpson et al. 2017; Zhukovska, Henning & Dobbs 2018).

We also derive the gas fraction, the ratio of the molecular gas mass to the total baryonic mass of the galaxy, which is:

$$f_{\rm gas} = \frac{M_{\rm gas}}{M_{\rm gas} + M_*} \tag{4}$$

and show its variation with redshift in Fig. 12(d). We derive a median gas mass fraction of $f_{\rm gas} = 0.41 \pm 0.02$ with a 68th percentile range of $f_{\rm gas} = 0.24$–$0.72$, comparable to the median gas fraction of $f_{\rm gas} = 0.38 \pm 0.03$ for the local ULIRGs from the GAMA survey estimated in an identical manner. We see modest evolution of $f_{\rm gas}$ with redshift, with a gradient of $\mathrm{d}f_{\rm gas}/\mathrm{d}z = 0.06 \pm 0.02$. For comparison, we overlay the ASPECS blind CO-selected sample from Aravena et al. (2019) and the CO-detected 'main sequence' galaxies from the PHIBSS compilation of star-forming galaxies by Tacconi et al. (2018). Gas fraction of SMGs and 'main-sequence' galaxies at $z \gtrsim 2$ appears to be similar.

Finally, we estimate the dust obscuration to the source of far-infrared emission averaged along the line of sight. In order to estimate this dust obscuration, we first estimate the column density of hydrogen atoms for the 154 sources that have 870-$\mu$m sizes (Gullberg et al. 2019, further discussed in Section 5.5.2), assuming $\delta_{\rm gdr} = 100$ to convert dust mass into gas mass, and find a median of $N_{\rm H} = (1.66 \pm 0.14) \times 10^{24}\,{\rm cm}^{-2}$. Dust attenuation is related to hydrogen column density by, $N_{\rm H} = 2.21 \times 10^{21}\,A_V$, and thus we find a median line-of-sight dust attenuation of $A_V = 750 \pm 60$ mag. The result is within the error range of Simpson et al. (2017) (who found a median $A_V = 540^{+80}_{-40}$ mag) when

samples are selected in the same manner, having detections in all three SPIRE bands, resulting in a median $A_V = 700 \pm 90$ mag.

As the hydrogen column and dust attenuation results are suggesting dusty, highly obscured systems, we estimate the wavelength at which the optical depth, $\tau$, becomes optically thin, $\lambda_0$. We, first, derive the brightness temperature of the SMGs with 870-$\mu$m sizes using

$$B_{\nu_{\rm rest}}(T_{\rm B}) = 0.5 S_{\nu_{\rm rest}}(1+z)^3/\Omega_{\nu_{\rm obs}}, \quad (5)$$

where $B_{\nu_{\rm rest}}$ is the full Planck function and the solid angle subtended by the source is $\Omega_{\nu_{\rm obs}} = \pi R_\nu^2/D_{\rm A}^2$, where $R_\nu$ is the emission region size and $D_{\rm A}$ is the angular diameter distance. The factor of 0.5 is included as we are considering the emission within the half-light radius. Using equation (5), we estimate a median brightness temperature of $T_{\rm B} = 21 \pm 1$ K, with a 16–84th percentile range of 16–28 K. The brightness temperature can be related to the true dust temperature and optical depth by

$$\frac{1}{{\rm e}^{h\nu/kT_{\rm B}} - 1} = \frac{1 - {\rm e}^{-\tau_\nu}}{{\rm e}^{h\nu/kT_{\rm D}} - 1}. \quad (6)$$

As in Section 4.3.2, we used fixed dust emissivity index of $\beta = 1.8$ in the calculation of optical depth. We make the assumption that the emission region at 250, 350, and 500 $\mu$m is the same size as that measured at 870 $\mu$m. We note that, for a given source, the observed size of the emission varies with optical depth as it increases with frequency. Thus, our assumption overestimates the flux density within the 870-$\mu$m half-light radius for 250-, 350-, and 500-$\mu$m emission. Therefore, our estimated dust temperature and optical depth are the lower limits of the true values.

We use a sub-sample of 64 sources that have 870 $\mu$m sizes and detections in all three SPIRE bands to solve for both, dust temperature and optical depth, using Markov Chain Monte Carlo method. We estimate a median true dust temperature of $T_{\rm D} = 40 \pm 2$ K and a median optical depth of unity, $\lambda_0 = 106 \pm 6\,\mu$m and we note that both of these quantities are the lower limit estimates. The wavelength estimate is comparable to the results from Simpson et al. (2017), who found $\lambda_0 \gtrsim 75\,\mu$m for a small sub-sample of 14 UDS SMGs.

## 5 DISCUSSION

Having analysed the physical properties of SMGs and their evolution, in this section, we focus on combining these results to investigate three main aspects in detail: formation and evolution of SMGs, their relationship to the wider population of massive galaxies, and insights into the distribution of the star-forming regions within this population.

### 5.1 Evolution and lifetimes

It is expected to be challenging to reliably constrain the age of the stellar populations in SMGs due to their high obscuration and the influence of the intense recent star formation on the SED, as well as the degeneracies between age and other parameters such as redshift. Nevertheless, the analysis of the model SEDs of simulated strongly star-forming galaxies from EAGLE (described in Section 3.2) suggests that there is some diagnostic information in the derived ages from MAGPHYS, as there is a positive linear correlation between these and the mass-weighted stellar ages in the model (see Fig. A2). In Fig. A2 (see Appendix A), we see that the median scatter around the best-fit line is $\|({\rm Age}_{\rm MAGPHYS} - {\rm Age}_{\rm best-fit})\|/{\rm Age}_{\rm MAGPHYS} = 0.52$ for the sample. In comparison, the median fractional error on ages in the AS2UDS sample is 0.54. These errors are comparable, thus the systematic error is encompassed in the error returned from MAGPHYS. As such mass-weighted ages may be used to infer the typical formation epoch of the SMGs and to assess the evolution of properties of this population.

#### 5.1.1 Mass-weighted ages

We first compare the mass-weighted ages to estimates of ages of SMGs derived from other physical properties. We derive a median mass-weighted age of our sample of ${\rm Age_m} = (0.46 \pm 0.02)$ Gyr. We note that the posterior likelihood distribution differs significantly from the prior shown in Fig. 9(d), suggesting the model is varying this parameter when fitting the SED.

We have two other methods to estimate 'ages' for the SMGs. First, we can take the derived stellar mass and the current star-formation rate and ask how long it would take to form the observed mass? This age parameter, $M_*$/SFR, has a median ratio of $M_*/{\rm SFR} = 1.28 \pm 0.02$ Gyr, and correlates very closely with ${\rm Age_m}$ for ages $\lesssim$0.7 Gyr (corresponding to the bulk of the population at $z \gtrsim$ 2–3). Approximately 10 per cent of SMGs, mostly at $z \lesssim 2$ have $M_*$/SFR higher than ${\rm Age_m}$, indicating either a declining star-formation rate or significant previous stellar mass in these galaxies.

The second estimate we can obtain comes from the expected lifetime of the current star-formation event, given by the ratio of the estimated gas mass to the star-formation rate: $M_{\rm gas}$/SFR. This characteristic lifetime is also twice the gas depletion timescale as we assume to be observing the SMGs halfway through the burst. This was estimated in Section 4.3.6 as $146 \pm 5$ Myrs, yielding a lifetime of $292 \pm 10$ Myrs. This shows a weak correlation with ${\rm Age_m}$ with significant dispersion and around ∼20 per cent of the SMGs (covering the whole redshift range) have gas depletion timescales which are longer than their mass-weighted ages, suggesting that the current star-formation event may represent the first major star-formation episode. However, for the bulk of the population, it appears that there is a preexisting (older) stellar population in these systems.

In Fig. 11(d), we plot mass-weighted age as a function of redshift. We show the limit provided the age of the Universe at a given redshift. The best-fitting trend to the ${\rm Age_m}$–$z$ plot suggests a statistically significant evolutionary trend of age with redshift with a gradient of ${\rm d}(\log_{10}({\rm Age_m}))/{\rm d}z = -0.29 \pm 0.02$, so that higher-redshift SMGs are systematically younger. However, we caution that this may be a consequence of the code fitting younger ages to hotter dust components which are more prevalent at higher redshifts. For comparison, we overlay the local ULIRGs sample from the GAMA survey. We see that the median age from the local ULIRG sample agrees with the trend we observe at higher redshift, with these galaxies having overall older mass-weighted ages (as expected).

To assess the influence of the current star-formation activity on the evolution of the SMGs, we determine when the current star-formation is likely to cease. Again, using our estimate a median gas depletion timescale of $\tau_{\rm dep} = 146 \pm 5$ Myr with a 68th percentile range of $\tau_{\rm dep} = 53$–$321$ Myr for the SMGs at $z = 1.8$–$3.4$, this indicates that the star-formation activity in this population is expected to cease by $z \sim 2.5$, soon after their peak at $z = 2.6$. The stellar populations in these systems would then evolve to become red and quiescent by $z \sim 2$, in the absence of subsequent gas accretion and star formation. Similarly, assuming that, on average, we see the SMGs halfway through their most active phase, we can adopt this

depletion timescale as the likely age of the SMG-phase at the point we observe the SMG. Comparing this estimate to the median mass-weighted age of the $z = 1.8$–$3.4$ SMG sub-sample, $490 \pm 20$ Myr (68th percentile range of 97–960 Myr), suggests that the bulk of the population had some pre-existing stellar population before the onset of the current star-formation event. We can also consider the mass produced in the last ∼150 Myr (when the SMG-phase started) assuming a constant star-formation rate. We find a median fraction of $M_{150\mathrm{Myr}}/M_* \sim 0.3$. This means that, for an average SMG, ∼30 per cent of the current stellar mass was formed in the last 150 Myr, and by the end of the SMG-phase these systems would have roughly doubled their pre-existing stellar masses.

### 5.1.2 *Lifetimes of SMGs*

As seen in Fig. 7, the redshift distribution of our complete sample of 707 ALMA-identified AS2UDS SMGs has a median redshift of $z = 2.61 \pm 0.08$, with a 68th percentile range of $z = 1.8$–$3.4$. The rapid decline in the number density of SMGs, we see at both $z \lesssim 2$ and $z \gtrsim 3.5$ are striking. We stress that by virtue of employing full-SED modelling with MAGPHYS, the redshift distribution in Fig. 7 comprises the summed PDFs of all of the SMGs in our sample, not just the biased subset, which are detectable in the optical/near-infrared (e.g. Simpson et al. 2014) and without having to employ a heterogeneous mix of redshift estimators (e.g. Brisbin et al. 2017; Cowie et al. 2018). We find a highly peaked redshift distribution, which drops rapidly at higher redshifts, with ∼30 per cent of the SMGs lying at $z > 3$, and just ∼6 per cent at $z > 4$. Equally, we find only five examples of SMGs at $z < 1$, some of which may be unidentified weakly amplified galaxy–galaxy lenses (e.g. Simpson et al. 2017).

For the subsequent analysis, we use only the 364 ALMA SMGs with $S_{870} \geq 3.6$ mJy. This matches the flux density limit of the parent S2CLS survey (Geach et al. 2017), which covers an area of 0.96 deg$^2$ and so allows us to estimate the appropriate volume densities from the sample. We also correct our estimates for the incompleteness in SCUBA-2 850-$\mu$m sample in the UDS field (Geach et al. 2017). In Fig. 13(a), we recast our redshift distribution to illustrate the variation in volume density ($\phi$) of bright SMGs with cosmic time. Fig. 13 shows that the volume density of AS2UDS SMGs peaks around ∼2.4 Gyr after the big bang with a 16–84th percentile range of 1.8–4.5 Gyr. The distribution is log-normal, with a mean of $\mu = 0.97 \pm 0.03$ Gyr, a standard deviation of $\sigma = 0.32 \pm 0.04$ Gyr, and a normalization of $c = (1.7 \pm 0.2) \times 10^{-4}$ Mpc$^{-3}$Gyr$^{-1}$. We also combine the redshifts with the mass-weighted ages of each SMG (see Section 5.1.1) to predict the distribution of formation ages of the SMGs. This distribution also follows a log-normal shape with a median cosmic time at formation of ∼1.8 Gyr after the big bang, and log-normal parametrization of $\mu = 0.68 \pm 0.03$ Gyr, $\sigma = 0.30 \pm 0.03$ Gyr, and $c = (1.08 \pm 0.08) \times 10^{-4}$ Mpc$^{-3}$Gyr$^{-1}$. Fig. 13(a) shows that the SMGs begin to form in large numbers at a cosmic time of ∼1.8 Gyr, corresponding to $z \sim 3.5$. This confirms that the rapid rise in number density we see in the redshift distribution at $z \lesssim 3.5$ is being driven by the onset of this population.

### 5.1.3 *Formation of SMGs*

Previous measurements of the spatial clustering of SMGs imply dark matter halo masses for SMGs of $M_\mathrm{h} \sim 10^{13}$ M$_\odot$ (Hickox et al. 2012; Wilkinson et al. 2017). More crucially, Hickox et al. (2012) suggested that the SMG redshift distribution is related to the growth rate of cosmological structures. The basis of this model is the concept of a critical threshold mass for haloes, which has been developed to interpret the clustering evolution of QSOs (e.g. Overzier et al. 2003; Farrah et al. 2006). To investigate this further, we use the Millennium Simulation (Springel et al. 2005) to determine the growth rate of dark matter haloes as a function of redshift. Using the dark matter merger trees from this 500 $h^{-1}$ Mpc$^3$ simulation, we measure the volume density of dark matter haloes at each redshift that pass through mass thresholds of $M_\mathrm{h} = 10^{11}$–$10^{15}$ M$_\odot$ in steps of 0.05 dex. To account for the evolution of the molecular mass fraction within haloes, we convolve these volume densities with the molecular gas fraction evolution (e.g. Lagos et al. 2011) and derive the redshift at which these distributions peak. By matching the distributions predicted by this simple model to our observed redshift, we estimate a 'critical-mass' for haloes of bright SMGs with $S_{870} \gtrsim 3.6$ mJy of $\log_{10}(M_\mathrm{h}) \sim 12.8$ M$_\odot$. In Fig. 13(b), we plot volume density of bright SMGs in our sample, limiting the SMGs to those brighter than $S_{870\mu\mathrm{m}} = 3.6$ mJy (which represents the flux density limit of the parent survey) and overlay the redshift distribution of these dark matter haloes for a critical mass of $\log_{10}(M_\mathrm{h}) \sim 12.8$ M$_\odot$.

In this model, the rapid decrease in the number density of SMGs at $z \lesssim 1.5$–$2$ is explained by the decline in the molecular gas fraction in the haloes (Geach et al. 2011; Lagos et al. 2011; Tacconi et al. 2018), as well as the decrease in the number of dark matter haloes that transit above the mass threshold as the Universe expands. Fig. 13(b) shows that the shape of the redshift distribution of SMGs appears to be reasonably well described by this combination the cosmological growth of structure and the evolution of the molecular gas fraction in galaxies.

The halo mass of $\sim 6 \times 10^{12}$M$_\odot$, estimated from the SMG redshift distribution, is comparable to the clustering results for SMGs (Hickox et al. 2012; Chen et al. 2016; Wilkinson et al. 2017; Stach et al. in preparation), which suggest that they occupy haloes of $\sim 10^{13}$M$_\odot$ at $z > 2.5$. This halo mass is also similar to that estimated from clustering studies for $L^*$ QSOs at $z \sim 1$–$2$ (Ross et al. 2009), supporting the evolutionary association between SMG and QSOs suggested by Hickox et al. (2012) and others. Cosmological models of halo growth indicate that a dark matter halo mass of $M_\mathrm{h} \sim 6 \times 10^{12}$ M$_\odot$ at $z \sim 2.6$ corresponds to a median descendent halo mass at $z \sim 0$ of $\gtrsim 10^{13}$ $M_\odot$, which is consistent with the 2–4 $L^*$ ellipticals at the present day (Zehavi et al. 2011). Moreover, the characteristic halo mass we estimate agrees well with the theoretical prediction of the maximum halo mass where gas can cool and collapse within a dynamical time White & Rees (1978) and is thus also the halo mass associated with the highest star-formation efficiency (Gerhard et al. 2001; Behroozi, Wechsler & Conroy 2013).

This may suggest that SMGs represent efficient collapse occurring in the most massive, gas-rich haloes which can host such activity. This simple model provides a natural explanation for them representing the highest star-formation rate sources over the history of the Universe, as well as for the details of their redshift distribution (Fig. 13). Moreover, it offers a description of why their massive galaxy descendants at $z \sim 0$ have the highest stellar baryonic to halo mass ratios of any collapsed systems (Gerhard et al. 2001).

## 5.2 Evolution of the far-infrared luminosity and gas mass functions

Having determined the redshifts, far-infrared luminosities, and dust masses for our SMG sample, we can exploit the fact that our survey is derived from a uniformly selected sample of 850-$\mu$m SCUBA-2

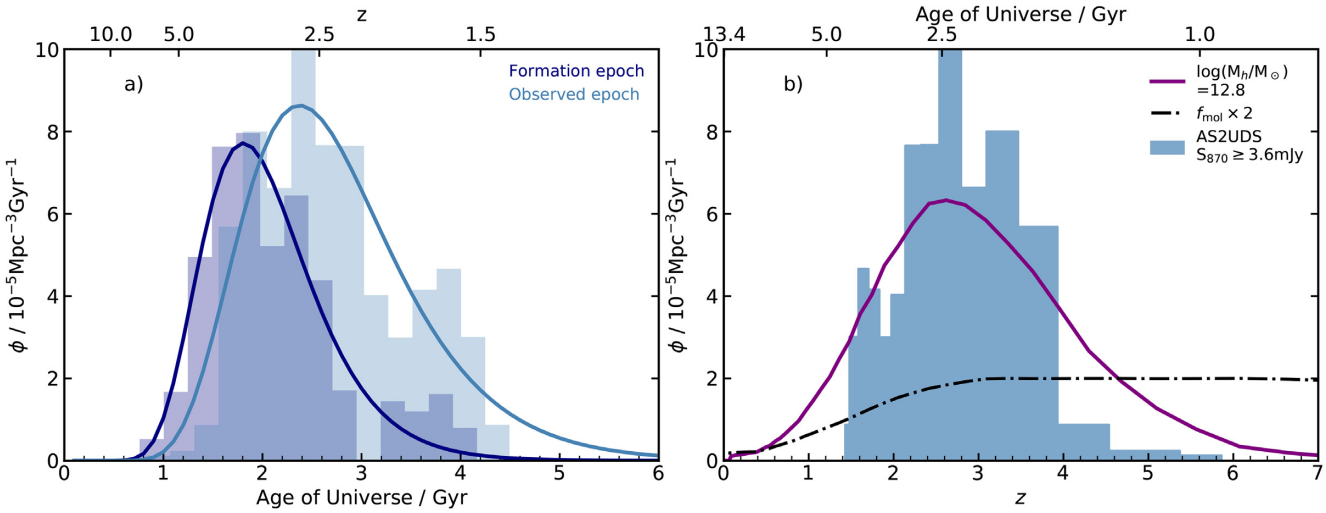


**Figure 13.** **(a)** The distribution of cosmic ages for the observed epochs of the AS2UDS SMGs and the inferred formation epochs for these galaxies (corrected for their estimated ages) corrected for incompleteness following (Geach et al. 2017). The solid lines show log-normal fits to the respective distributions. We see that the observed age distribution peaks at ∼2.4 Gyr, while the inferred formation-age distribution peaks at ∼1.8 Gyr ($z \sim 3.5$), with both well described by log-normal distributions. **(b)** The stacked likelihood redshift probability distribution of the sample of 364 AS2UDS SMGs that have $S_{870} \geq 3.6$ mJy corrected for incompleteness following (Geach et al. 2017). We overlay a simple analytic model assuming that SMGs reside in haloes whose mass crosses a characteristic threshold of $\sim 6 \times 10^{12}$ M$_\odot$ and accounting for the evolution of molecular gas fraction with redshift ($f_{\rm mol}$, scaled by a factor of 2, is shown by a dashed line) in the haloes. The model follows our distribution well as shown by the solid line. This normalization represents the duty cycle correction for the SMGs.

sources across a degree-scale field (Geach et al. 2017) to determine the luminosity and gas mass functions of SMGs and their evolution. We, therefore, use the subset of 364 ALMA SMGs brighter than the flux density limit of the SCUBA-2 catalogue, $S_{870} \geq 3.6$ mJy, and correct for incompleteness (∼20 per cent at $S_{870} = 3.6$ mJy, Geach et al. 2017) to obtain an 870-$\mu$m selected sample across the full UDS field. We note that ∼74 per cent of these SMGs are detected in at least one SPIRE band and hence have robust far-infrared luminosities.

### 5.2.1 *Far-infrared luminosity function*

We calculate the far-infrared luminosity function for the 870-$\mu$m selected AS2UDS sample within the accessible volume using $\phi(L_{\rm IR})\Delta L_{\rm IR} = \Sigma(1/V_i)$, where $\phi(L)\Delta L$ is the number density of sources with luminosities between $L$ and $L+\Delta L$ and $V_i$ is the co-moving volume within which the $i$th source would be detected in a given luminosity bin. We split the sample of the 364 AS2UDS SMGs brighter than $S_{870} = 3.6$ mJy into three redshift bins with similar number of galaxies in each: $z < 2.35$, $z = 2.35$–$3.00$, and $z > 3.00$. The resulting luminosity functions are shown in Fig. 14(a). Errors are estimated using a bootstrap method by re-sampling the photometric redshift and luminosity PDFs. We fit the luminosity functions using Schechter functions of the form, $\phi = (\phi^*/L^*)(L/L^*)^\alpha {\rm e}^{-L/L^*}$, where $\phi^*$ is the normalization density, $L^*$ is the characteristic luminosity, and $\alpha$ is the power-law slope at low luminosities (Schechter 1976). Clemens et al. (2013) derive $\alpha = -1.3$ for their *Planck* detections of a local volume-limited galaxy sample, while Dunne et al. (2011) derive $\alpha = -1.2^{+0.4}_{-0.6}$ for a SPIRE-selected sample out to $z \sim 0.5$, while other studies have yielded values ranging $\alpha = -1.0$ to $-1.7$ (Vlahakis, Dunne & Eales 2005; Dunne et al. 2011). As our sample covers only a relatively narrow range in far-infrared luminosity at each redshift, we are unable to constrain $\alpha$ directly and so instead we choose to fix it to $\alpha = -1.5$. The Schechter fits to each redshift slice are shown in Fig. 14.

To demonstrate the evolution of the ULIRG population across our survey volume, we also plot in Fig. 14(a) an estimate of the local far-infrared luminosity function from the sample derived from the GAMA survey from Driver et al. (2018) at $z \sim 0.6$. Examining the evolution in the luminosity function within our survey in Fig. 14(a), we see that the space density increases from the $z < 2.35$ to peak in the $z = 2.35$–$3.00$ bin (median redshift $z \sim 2.6$) and then declines at $z > 3.00$. Compared to local ULIRGs, we conclude that the AS2UDS SMGs have a space density that is a factor of ∼100 higher, similar to the findings for the smaller ALESS sample from Swinbank et al. (2014). In comparison to other estimates of the high-redshift far-infrared luminosity function, we find that our measurements for this rest-frame 200–300-$\mu$m-selected samples lie below those from the PEP survey from Gruppioni et al. (2013), which is based on 100- and 160-$\mu$m-selected samples. This is due to the fact that our 870-$\mu$m selection is sensitive to cooler sources, with $T_{\rm d} \lesssim 50$–$60$ K, out to $z \sim 4$, thus we are incomplete for the hottest sources (such as in Gruppioni et al. 2013, see also Symeonidis et al. 2011; Gruppioni & Pozzi 2019).

### 5.2.2 *Gas mass function*

In an equivalent manner as in Section 5.2.1, we have estimated the gas mass function for the SMG population and its variation with redshift in three broad redshift ranges, illustrated in Fig. 14(b).

Here, we compare estimates of the gas mass function derived from the ASPECS blind mid-$J$ CO survey from Decarli et al. (2019) to the space densities for our gas mass functions in Fig. 15(b). We note that for this comparison, we have converted the ASPECS gas masses, which are based on a conversion from CO luminosity to molecular gas mass adopting $\alpha_{\rm CO} = 3.6$, to agree with the gas masses derived from MAGPHYS dust masses with a gas-to-dust ratio of 100. Decarli et al. (2016) show that this translates to a reduction in their estimated gas masses of a factor of $5.3 \pm 0.8$ and so we apply this conversion to compare to our MAGPHYS-derived estimates.

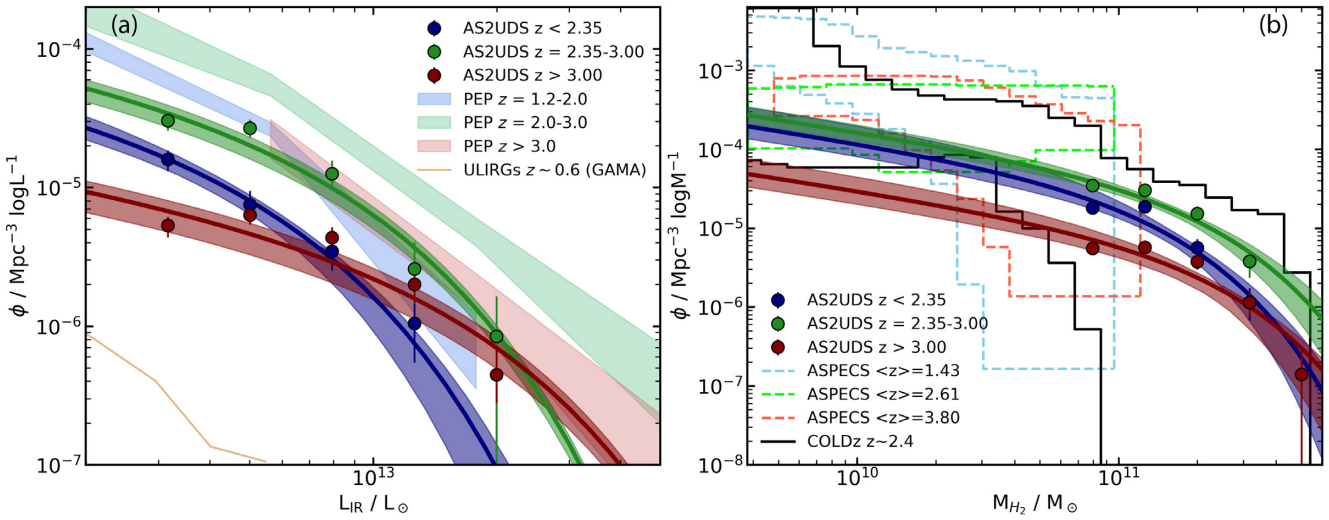


**Figure 14.** The evolution of the far-infrared luminosity function (left) and molecular gas mass function (right) from the flux-limited sample of $S_{870} \geq 3.6$ mJy AS2UDS SMGs corrected for incompleteness. These are both plotted for three independent redshift bins with a similar number of galaxies: $z < 2.35$, $z = 2.35$–3.0, and $z > 3.0$. Each of the bins is fitted with a Schechter function which is shown as the solid line in the respective colour. $1\sigma$ errors were obtained by resampling the luminosity or gas mass and redshift PDFs and the $1\sigma$ fitting error is shown as the shaded area. **(a)** We compare the AS2UDS far-infrared luminosity function to the PEP survey 100- and 160−$\mu$m selected samples from Gruppioni et al. ( 2013). We also compare to the local sample of ULIRGs ($z \sim 0.6$) from the GAMA survey. This demonstrates the roughly two orders of magnitude increase in space density of ULIRGs between $z \sim 0$ and $z \sim 2$–3, with the space density peaking at $z = 2.35$–3.00 and then declining at higher redshifts. **(b)** We compare the AS2UDS gas mass function to results from the ASPECS blind mid- *J* CO survey (Decarli et al. 2019) for three corresponding redshift ranges, where the ASPECS gas masses have been converted into the equivalent scale as our MAGPHYS estimates. We see good agreement between the mass functions from the two surveys across the three redshift slices at higher mass end. We also compare to results from the COLDz blind low-J CO survey (Riechers et al. 2019). We see good agreement between the $z$∼2.4 CO (1–0) sources and $z = 2.35$–3.00 SMGs luminosity functions.

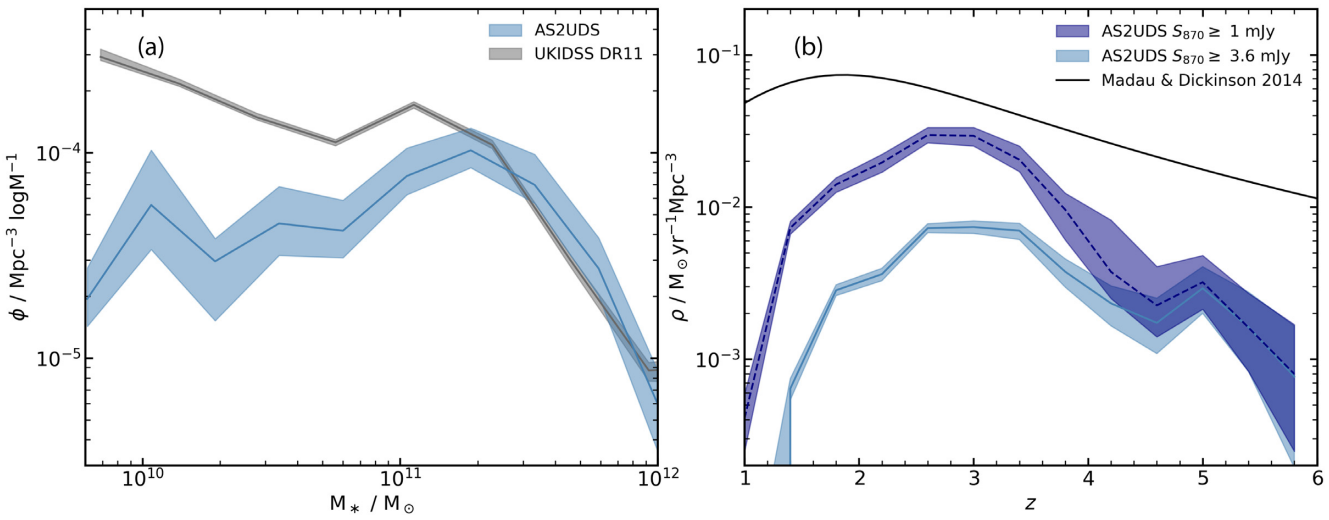


**Figure 15.** **(a)** Stellar mass function for $S_{870} \geq 3.6$ mJy SMGs at $z = 1.8$–3.4. The blue line shows the expected number density of galaxies, which had passed through an SMG-like phase, estimated from the distribution of the AS2UDS SMGs and corrected for duty cycle by a factor of 5.1 increase (see Section 5.3), with the respective $1\sigma$ error shown as the blue-shaded region. The grey line shows the stellar mass function of *K*-band selected galaxies in the UDS field with the $1\sigma$ error as the grey-shaded region. We see that the SMGs make an increasing contribution to the total mass density distribution at higher stellar masses. The corrected volume density of AS2UDS SMGs corresponds to ∼30 per cent of the total number density of galaxies above $M_* = 3 \times 10^{10}$ M⊙, but this fraction increases rapidly so that ∼100 per cent of galaxies at $M_* \gtrsim 3 \times 10^{11}$ M$_\odot$ are expected to have passed through an SMG-phase. **(b)** The co-moving cosmic star-formation density as a function of redshift. We show the contribution of AS2UDS sources for SMGs brighter than $S_{870} = 3.6$ mJy and also brighter than $S_{870} = 1$ mJy, where we correct the numbers of fainter sources using the 850-$\mu$m number counts (Geach et al. 2017) and 1.13-mm number counts (Hatsukade et al. 2018), adopting $S_{870}/S_{1130} = 1.8$. The shaded regions represent the $1\sigma$ error, which has been calculated by re-sampling the redshift probability distribution while taking into account the star formation–redshift correlation. This shows that the contribution from SMGs peak at higher redshift ($z \sim 3$) than the total star-formation rate density (Madau & Dickinson 2014) at which epoch SMGs with $S_{870} \geq 3.6$ mJy contribute ∼15 per cent to the total SFRD, and ∼60 per cent if we integrate down to the $S_{870} \geq 1$ mJy.

Our estimates of the gas mass function and those from ASPECS agree at the high gas mass end for all three redshifts (we show the corresponding 1 $\sigma$ confidence level measurements at $z = 1.4$, $z = 2.6$, and $z = 3.8$ from ASPECS), with the wide-field AS2UDS estimates adding information at the high gas mass end of the distribution, which is missing from ASPECS owing to its modest survey volume. We see that the extrapolated low-mass space densities from AS2UDS, based on our Schechter function fits with a low-mass slope of $\alpha = -1.5$, are broadly in agreement with the ASPECS samples down to masses of $\sim 10^{10}\,\mathrm{M}_{\odot}$, but fall below at lower masses, however, we note that these differences could be accounted for by the uncertainty in our adopted $\alpha$ value. We also compare our results to the gas mass function derived from the COLDz blind low- $J$ CO survey of Riechers et al. (2019) in Fig. 15(b) (converting from CO luminosity to molecular gas mass in an equivalent manner to ASPECS). The $z \sim 2.4$ CO (1–0) sources and $z = 2.35$–$3.00$ SMGs agree very well across the whole gas mass range. Thus, broadly, the evolution of the gas mass function from the combined AS2UDS + CO-selected samples appears to be best characterised by an increasing space density of galaxies at a fixed gas mass from $z \sim 3.5$ down to $z \sim 1.5$, with a hint that we may be seeing the space density of massive gas-rich systems beginning to decline at $z < 2.5$.

### 5.3 Stellar mass function

We next investigate what fraction of massive galaxies may have experienced a high star-formation rate phase, which would correspond to an SMG, and hence whether SMGs are a phase that all massive galaxies go through. For this comparison, we estimate the number density of massive galaxies using our MAGPHYS analysis of the $K$-band sample in the UDS field. This approach has the advantage that the stellar masses, redshifts, and survey volumes are estimated in an identical manner to those employed for the SMGs. We select those field galaxies that have redshifts lying in the 16–84th percentile range of the AS2UDS redshift distribution ($z = 1.8$–$3.4$). To ensure we have robust stellar mass estimates, we limit the field sample to galaxies with the best photometry and SED fits with a reduced $\chi^2 < 4$. We determine the influence of these cuts on the resulting sample size and increase the normalization of the field sample by a factor of 1.35 to correct for this. The UDS field catalogue is selected in the $K$-band, with a 3 $\sigma$ limit of $K = 25.7$ mag, which roughly corresponds to $M_* \sim 5 \times 10^9\,\mathrm{M}_{\odot}$ at $z \sim 3$ for typical star-formation histories. Therefore, for the field, we construct the stellar mass function above this stellar mass threshold to avoid incompleteness. We sum the number of galaxies in each stellar mass bin and divide by the volume defined by the span of their redshifts.

We calculate the SMG stellar mass function in an equivalent manner and then calculate the duty cycle of the SMGs by comparing the visibility time from Section 5.1.3 to the age spanning a given redshift slice ($\Delta T_z$): duty cycle correction as $\Delta T_z / T_{\mathrm{vis}}$. For the redshift range of $z = 1.8$–$3.4$, we find a median visibility time of $490 \pm 20$ Myrs and corresponding to a duty cycle correction factor of 5.1 times, which we apply to the SMG mass function. The uncertainties for both field and SMG stellar mass functions were obtained by re-sampling the stellar mass and redshift probability distributions and taking the 16–84th percentile range as the $1\sigma$ error.

Overlaying the corrected SMG mass function on the field in Fig. 15(a), we see that at lower stellar masses, galaxies that have passed through an SMG-phase would account for only a modest fraction of the total space density, e.g. ∼30 per cent of galaxies above $M_* = 3 \times 10^{10}\,\mathrm{M}_{\odot}$. This fraction increases to ∼100 per cent at $M_* \gtrsim 3 \times 10^{11}\,\mathrm{M}_{\odot}$, indicating that all of the galaxies above this mass are likely to have experienced an SMG-phase in the course of their evolution. The results from the EAGLE simulation presented in McAlpine et al. (2019) indicate that effectively all galaxies at $z \sim 0$ in the simulation with stellar masses above $M_* = 2 \times 10^{11}\,\mathrm{M}_{\odot}$ experienced a ULIRG-like phase where their star-formation rate exceeded $\sim 100\,\mathrm{M}_{\odot}\,\mathrm{yr}^{-1}$. This result is consistent with our finding as there is little evolution of the stellar mass function of these galaxies in this mass range since $z \lesssim 1.5$ (Kawinwanichakij et al. 2020).

### 5.4 Co-moving star-formation rate density

To investigate the contribution of SMGs to the total star-formation rate density as a function of redshift, we make use of the predicted star-formation rates of AS2UDS sources. We calculate the star-formation rate density for two subsets of our sample SMGs: those SMGs with $S_{870} \geq 3.6$ mJy (which is the limit of the parent survey) and those with $S_{870} \geq 1$ mJy SMGs. For the $S_{870} \geq 3.6$ mJy sub-sample, we correct for the incompleteness using the number counts from Geach et al. 2017. We also correct the estimated SFR of an SMG within its redshift PDF to account for the variation as a function of redshift in the inferred SFR. We correct the number of $S_{870} \geq 1$ mJy sources from our survey to match the expected number counts to this flux limit. We derive these using the ALMA 1.13-mm counts in the GOODS-S field from Hatsukade et al. (2018) and a factor of 1.8 to convert the 1.13-mm flux densities into 870 $\mu$m.

The resulting star-formation rate density of the AS2UDS SMGs is shown in Fig. 15(b). For comparison, we overlay the combined optical and infrared star-formation rate density from Madau & Dickinson (2014), this represents the total star-formation rate density in the Universe at $z \lesssim 3$, above which it is constrained only by surveys in the UV (unobscured sources). This comparison demonstrates that the activity of SMGs peaks at $z \sim 3$, higher than the peak of the Madau & Dickinson (2014) star-formation rate density at $z \sim 2$. This suggests that more massive and obscured galaxies are more active at earlier times. Fig. 15(b) also shows that contribution to the total star-formation rate density increases steeply from $z \sim 1$ with the peak contribution being ∼15 per cent at $z \sim 3$ for the $S_{870} \geq 3.6$ mJy sub-sample or ∼60 per cent for sources brighter than $S_{870} = 1$ mJy. This indicates that roughly half of the star-formation rate density at $z \sim 3$ arises in ULIRG-luminosity sources and this population appears to decline only slowly across the 1 Gyr from $z \sim 3$ to $z \sim 6$.

### 5.5 The scale of far-infrared emission in SMGs

Finally, we wish to investigate what we can learn about the conditions and structure of the star-forming regions of SMGs from our sample. For this, we will employ sizes for a subset of our SMGs that have been derived from the analysis of high-resolution dust continuum observations of 154 SMGs in A2SUDS by Gullberg et al. (2019). This work exploits the fact that the Cycle 3 observations for AS2UDS were obtained with ALMA in an extended configuration, which yielded a synthesised beam with an FWHM of 0.18 arcsec (∼ 1 kpc). Gullberg et al. (2019) undertook extensive testing and analysis of the constraints on the sizes, profiles, and shapes of SMGs provided by these high-resolution 870-$\mu$m maps. On the basis of these tests, they restricted their analysis to only the highest angular resolution data available and in addition, applied a further cut that the sources had to be detected in a 0.5 arcsec-tapered map

with an S/N > 8. This ensured that the resulting profile and shape measurements were unbiased and of sufficient quality to be useful. The resulting sizes have median errors of just 20 per cent for a sample of 154 SMGs broadly representative of the full population of AS2UDS SMGs. Gullberg et al. (2019) measure a number of profile, shape, and size parameters for the SMGs from fits to the *uv* amplitudes in Fourier space and also image-plane fits to the reconstructed maps. They show that dust emission from typical SMGs is well-fit by exponential profiles described by a Sersic model with $n \sim 1$ (see also Hodge et al. 2016, 2019; Simpson et al. 2017). In the analysis, here we make use of the circularised effective radii derived from fits to the *uv* amplitudes for the sources adopting $n = 1$ Sersic profiles. We then convert these angular sizes into physical units using the photometric redshifts determined for the individual sources. The median physical size, expressed as $R_e$, of the sample is $0.83 \pm 0.01$ kpc.

### 5.5.1 *Star-formation conditions in SMGs*

The high median star formation of the AS2UDS sources (see Fig. 9) may be a result of SMGs behaving as Eddington-limited starbursts (Andrews & Thompson 2011), where the radiation pressure from massive stars is sufficient to quench further activity. To test this, we plot the 870-$\mu$m physical sizes versus the star-formation rate for the SMGs in Fig. 16(a). For comparison, we overlay two other studies that employed similar S/N ALMA observations, but at lower resolution (0.3–0.7-arcsec FWHM), of samples of SMGs in the UDS field: 870-$\mu$m sizes from the AS2UDS-pilot study of bright SMGs by Simpson et al. (2015a), which have a median effective radius of $R_e = 0.79 \pm 0.05$ kpc, and a subset of AS2UDS SMGs detected using the AzTEC camera on the ASTE telescope and followed-up with ALMA at 1.1 mm by Ikarashi et al. (2017), which yield a median effective radius of $R_e = 1.1 \pm 0.1$ kpc. Even though these two samples use lower resolution observations, they recover similar distributions in terms of the physical sizes of the SMGs.

We observe no strong trend in size with star-formation rate and so we now test whether the star-formation activity in SMGs is affected by their approaching the Eddington luminosity limit for their observed sizes and star-formation rates. We follow Andrews & Thompson (2011), who demonstrated that the balance of radiation pressure from star formation, with self-gravity results in a maximum star-formation rate surface density (in units of $M_\odot\,yr^{-1}\,kpc^{-2}$) of

$$\mu_{SFR}^{max} = 11\, f_{gas}^{-0.5} \delta_{GDR}, \quad (7)$$

where $f_{gas}$ is the gas fraction in the star-forming region and $\delta_{GDR}$ is the gas-to-dust ratio (as mentioned in Section 4.3.6, we adopt 100). The equation assumes optically thick dust emission and no heating from an AGN. Our estimated galaxy-integrated gas fractions from Fig. 11(d) are $f_{gas} \sim 0.4$ and we see no significant variation in this with redshift. However, the available near-infrared imaging suggests that the stellar mass component, which is used to estimate $f_{gas}$, is likely to be more extended than the size of the dust continuum emission, potentially by a factor of ∼4 times (Simpson et al. 2017; Ikarashi et al. 2015; Lang et al. 2019; Gullberg et al. 2019). Due to uncertainty in the calculated gas fraction, we take a conservative approach and adopt a gas fraction of unity, which provides the lower limit of the star-formation rate surface density (for comparison, the Eddington limit assuming $f_{gas} = 0.4$ is shown in Fig. 16a).

The resulting maximum star-formation rate surface density predicted by the model is $1{,}100\,M_\odot yr^{-1}\,kpc^{-2}$ and we show this line in Fig. 16(a). Comparing the AS2UDS SMGs to this line, we see that very few have sizes, which are compact enough for them to approach the Eddington limit for their observed star-formation rates. On average, the AS2UDS have sizes around ten times larger than an Eddington-limited system with their same star-formation rate, indicating that averaged on kpc-scales the radiation pressure from the on-going star formation in these systems is not sufficient to quench their activity. However, if the star-forming region for a given galaxy is 'clumpy' on small scales (Danielson et al. 2011; Swinbank et al. 2011; Menéndez-Delmestre et al. 2013), then individual regions on sub-kpc scales may be Eddington limited.

### 5.5.2 *Structure of the far-infrared regions of SMGs*

We now turn to examine the possible structure of the far-infrared luminous component of the SMGs. As suggested in Section 5.5.1, the conditions of star formation are dependent on whether the far-infrared sources have a single homogeneous dust cloud structure or are 'clumpy' systems. We investigate this by comparing our results to an optically thick model from Scoville ( 2013).

As outlined in Scoville (2013), internally heated far-infrared sources are described by two properties: the luminosity of the central heating source and total dust mass in the surrounding envelope. Thus, this structure can be characterised by a single parameter: their luminosity-to-mass ratio. The FIR SEDs can be calculated for this using a temperature profile, which is estimated from a combination of optically thin dust emission at the inner region (where $T_d \propto r^{-0.42}$), optically thick (where $T_d \propto r^{-0.5}$ as the photons heating the grains and those that are emitted by the grains have similar wavelength distributions) at intermediate radii and optically thin again at larger radii (Scoville 2013). The inner radius is taken at 1 pc (where $T_d$=1000 K, close to the dust sublimation limit) and the outer radius is taken at 2 kpc, which is roughly appropriate for SMGs (Gullberg et al. 2019). In the plot, the effective radius of the model is defined as radius of the shell producing the largest fraction of the overall luminosity for each of the $L/M_{ISM}$ values, where $M_{ISM} = M_{HI} + M_{H_2}$. A full description can be found in Scoville (2013). In Fig. 16(b), we show results for an optically thick, radiative transfer modelling of the dust emission for a $r^{-1}$ dust density distribution (they found similar results were found with other reasonable power laws) from Scoville (2013). They set the luminosity as $10^{12}\,L_\odot$ and vary the total dust mass in the range of $10^7$–$10^9\,M_\odot$ (both appropriate for our sample) and calculate the effective radius as the radius of the shell producing the majority of the overall luminosity. In our analysis, we assume a dust-to-gas ratio of 100 to estimate the gas mass of SMGs, which is comparable to the $M_{ISM}$ definition of the model used in Scoville (2013), who adopt a ratio of ∼100.

As mentioned above, the model in Fig. 16(b) assumes SMGs are described by a single homogeneous optically thick dust cloud. In order to compare how the effective radius of SMGs varies with the luminosity-to-mass ratio, we overlay the results derived for the 122 AS2UDS sources which have 870$\mu$m size information and at least one SPIRE detection. We split the sources by radius into four bins to assess the broad trends. We see an overall trend of decreasing dust continuum size with increasing luminosity-to-mass ratio. The observations broadly agree with the ratio of size to $L/M_{ISM}$ in the Scoville (2013) model, suggesting that the dust emission from our SMG sample is, on average, consistent with a homogeneous and homologous population of centrally illuminated dust clouds. The scatter we observe could partly be due to the variation of profiles in the clouds.

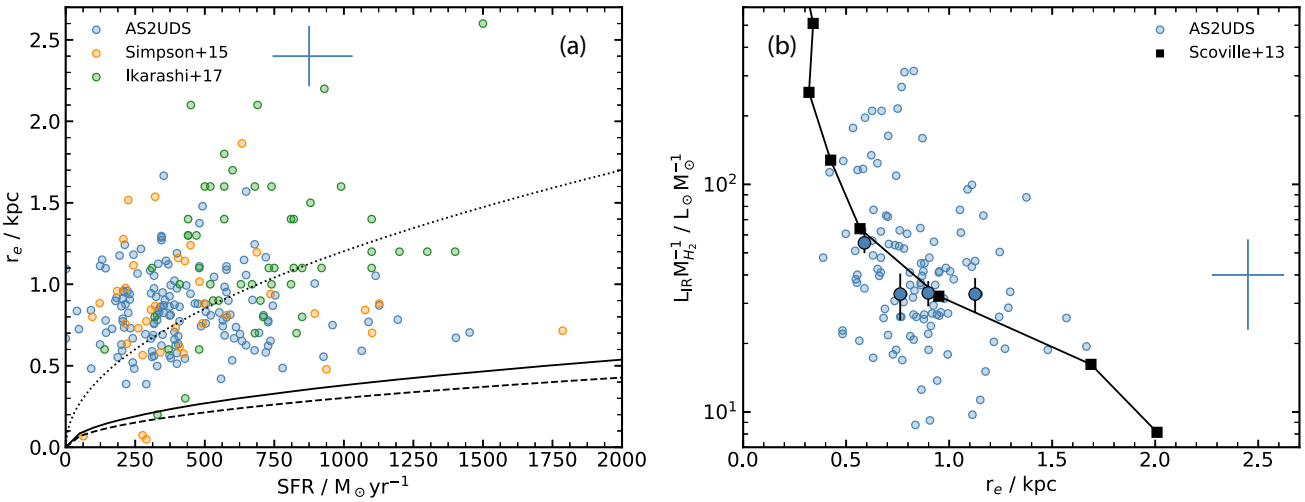


**Figure 16.** **(a)** The variation of 870-$\mu$m dust continuum size from Gullberg et al. (2019) with star-formation rate for the AS2UDS SMGs. We also plot the sizes derived from lower resolution ALMA continuum observations of samples of SMGs in the UDS field at 870 $\mu$m from Simpson et al. (2015b) and 1.1 mm by Ikarashi et al. (2017) (the star-formation rate for these are derived from our MAGPHYS analysis of these galaxies). We see a weak trend of increasing size at higher star-formation rates, with significant scatter. We compare this trend to the boundary expected from the estimated Eddington limit following Andrews & Thompson (2011) for $f_{\rm gas}=1$, which is shown as the solid line. The dotted line indicates the 0.1 times this Eddington limit, which roughly goes through the median of our sample. The dashed line indicates the Eddington limit for $f_{\rm gas}=0.4$. We see that very few of the SMGs have sizes which are compact enough for them to approach the Eddington limit at their star-formation rate. On average, the AS2UDS have sizes around ten times larger, and thus areas approaching two orders of magnitude larger than an Eddington-limited system with their star-formation rate, suggesting that this fundamental feedback process will not quench their activity. **(b)** 870-$\mu$m dust continuum size as a function of far-infrared luminosity-to-gas mass ratio for SMGs with at least one SPIRE detection. Large circles are the median values binned by radius of $\sim$30 sources and the median error for individual sources is indicated at the top of the panel. We overlay the model of an optically thick dust cloud from Scoville (2013). The AS2UDS SMGs have a similar trend to this model, however, with scatter below the model at low luminosity-to-mass ratios and above the prediction for high ratios. The overall agreement between model and AS2UDS sizes at a given radius indicates that SMGs are possibly homogeneous, and thus homologous, systems in the far-infrared, behaving as expected for a single dust cloud.

We note the structure of the dust clouds in SMGs did not necessarily have to follow this trend: some studies have claimed 'clumpy' structure of the star-forming regions in SMGs (Swinbank et al. 2011; Danielson et al. 2011; Menéndez-Delmestre et al. 2013). If the structure of dust clouds in the SMGs was indeed 'clumpy', the radial extent of the emission would be higher for a given luminosity-to-mass ratio. Thus, from their far-infrared emission, SMGs appear to, on average, behave as a sample of sources with very similar structures where the emission is consistent with a central source (starburst) illuminating a surrounding dust/gas reservoir with relatively similar sizes, densities and profiles.

## 6 CONCLUSIONS

In this study, we investigated the physical properties of 707 ALMA-identified sub-millimetre galaxies from the AS2UDS survey (Stach et al. 2019), with flux densities in the range $S_{870}$ = 0.6–13.6 mJy (with a median of 3.7 mJy). We fit spectral energy distribution models to the available photometry in 22 bands (from the UV to radio wavelengths) of each SMG using MAGPHYS, deriving physical properties such as their photometric redshifts, stellar and dust masses and far-infrared luminosities. Our homogeneously selected survey with uniform photometric coverage allows us to construct sub-samples (including an unbiased luminosity-selected sub-sample) to investigate the evolutionary behaviour of this population. Our main findings are:

(i) For a sample with a median 870-$\mu$m flux density of $S_{870}$ = 3.6 mJy, $\sim$80 per cent of the galaxies are detected in the extremely deep $K$-band data available for the UKIDSS UDS field ($3\sigma$ limit of $K$ = 25.7). This demonstrates that $\sim$20 per cent of SMGs are undetectable in very deep optical/near-infrared observations and hence, that there exists a significant population of strongly star-forming, but strongly dust-obscured galaxies missed by surveys in those wavebands.

(ii) The redshift distribution of our full sample of SMGs has a median of $z = 2.61 \pm 0.08$ with a 68th percentile range of $z = 1.8$–3.4, which is consistent with results for smaller samples of SMGs in other fields using photometric or spectroscopic redshifts. Those SMGs that are undetected in the $K$ band appear to preferentially lie at higher redshifts, with $z = 3.0 \pm 0.1$, while SMGs which are detected at 1.4 GHz lie at redshift comparable to the median of the whole SMG population, $z = 2.5 \pm 0.1$. The volume density of SMGs has a distribution, which is lognormal, peaking $\sim$2.4 Gyr after the big bang with the 16–84th percentile range of 1.8–4.5 Gyr. The inferred formation age distribution peaks at $\sim$1.8 Gyr ($z \sim 3.5$).

(iii) The SMG redshift distribution can be reproduced by a simple model describing the growth of haloes through a characteristic halo mass, of $\sim 6 \times 10^{12}$ M$_\odot$, combined with an increasing molecular gas fraction at higher redshifts. This model suggests that SMGs may represent efficient collapse occurring in the most massive haloes that can host such activity. For a dark matter halo mass of $6 \times 10^{12}$ M$_\odot$ at $z \sim 2.6$, the median descendent halo mass at $z \sim 0$ is $\gtrsim 10^{13}$ M$_\odot$, which is consistent with these galaxies evolving into 2–4 $L^*$ ellipticals at the present day.

(iv) Our 870-$\mu$m selected sample most closely resembles a sample selected on dust mass, with a ratio of dust mass in M$_\odot$ to 870-$\mu$m flux of $\log_{10}[M_{\rm d}({\rm M}_\odot)] = (1.20 \pm 0.03) \times \log_{10}[S_{870}({\rm mJy})] + 8.16 \pm 0.02$. There is a weaker correlation between 870-$\mu$m and far-infrared luminosity (or star-formation rate, with SFR $\propto S_{870}^{0.42 \pm 0.06}$). The median dust mass of our

sample is $M_{\rm d} = (6.8 \pm 0.3) \times 10^8\,{\rm M}_\odot$. Adopting a gas-to-dust ratio of $\delta_{\rm GDR} = 100$, this implies a median molecular mass of $M_{\rm H2} \sim 7 \times 10^{10}\,{\rm M}_\odot$. The median far-infrared luminosity of the SMGs in our sample is $L_{\rm IR} = (2.88 \pm 0.09) \times 10^{12}\,L_\odot$ and, with a median star-formation rate of ${\rm SFR} = 236 \pm 8\,{\rm M}_\odot\,{\rm yr}^{-1}$ (68th percentile range of ${\rm SFR} = 113$–$481\,{\rm M}_\odot\,{\rm yr}^{-1}$), suggests a gas depletion times of approximately 150 Myr (or an SMG-phase lifetime of ∼300 Myr assuming that, on average, we are witnessing the SMG halfway through its peak SFR phase). The characteristic gas depletion timescale declines by a factor of approximately two to three times across $z = 1$–4 the trend being driven by an increase in FIR luminosity with redshift in our sample as a result of selection effects.

(v) The average mass produced since the start of the SMG-phase (the last ∼150 Myr) assuming a constant star-formation rate compared to the total stellar mass has a median of $M_{\rm 150Myr}/M_* \sim 0.3$. Therefore, for an average SMG, ∼30 per cent of the current stellar mass was formed in the last 150 Myr, and by the end of the SMG-phase these systems are likely to roughly double their pre-existing stella r masses.

(vi) For SMGs with well-constrained far-infrared SEDs, we show that the median characteristic dust temperature for our sample is $T_{\rm d}^{\rm MBB} = 30.4 \pm 0.3$ K with a 68th percentile range of $T_{\rm d}^{\rm MBB} = 25.7$–37.3 K, with a trend of increasing temperature with luminosity. With an $L_{\rm IR}$-complete sample across $z = 1.5$–4, we are able to exclude the covariance with redshift. We see no evidence for a variation of dust temperature with redshift at fixed luminosity in this sub-sample, suggesting that previous claims of such behaviour are a result of luminosity evolution in the samples employed. However, we note that there is an apparent offset in dust temperature between our high-redshift sample and ULIRGs at $z < 1$, with the high-redshift SMGs being $3 \pm 1$K cooler at fixed $L_{\rm IR}$, but this comparison is complicated by the selection function of the local samples. We suggest the origin of this offset, if real, is likely to be due to the more compact dust distributions in the ULIRG population at $z < 1$.

(vii) We find that gas mass fraction of the SMGs evolves weakly from ∼30 per cent at $z \sim 1.5$ to ∼55 per cent at $z \sim 5$. These gas fractions are similar to those suggested for other high-redshift star-forming populations from mass and gas-selected samples. We note that the gas mass fraction of SMGs is similar to that estimated in an identical manner for *Herschel*-detected ULIRGs with comparable star-formation rate at $z < 1$ from the GAMA survey: ∼35 per cent. Thus, the primary differences we infer for ULIRGs at $z < 1$ is a much lower space density and more compact ISM distribution than those at $z \gg 1$.

(viii) We find that the median stellar mass of the SMGs is $M_* = (12.6 \pm 0.5) \times 10^{10}\,{\rm M}_\odot$ with a 16–68th percentile range of $M_* = (3.5$–$26.9) \times 10^{10}\,{\rm M}_\odot$. The typical mass does not evolve strongly with redshift, varying by < 10 per cent over the redshift range $z = 1$–4, although the star-formation rates for our sample increase by a factor of ∼3 over this same range (driven by the luminosity-redshift trend from the selection). In terms of the specific star-formation rate (SFR/ $M_*$), we see that, at $z \sim 1$, typical SMGs lie a factor of ∼6 above the 'main sequence' (defined by the field population modelled using MAGPHYS for consistency). By $z \sim 4$, SMGs lie a factor of 2 above the 'main sequence', due to the strong evolution of sSFR of the 'main sequence'.

(ix) By comparing to the stellar mass function of massive field galaxies, and accounting for the duty cycle of SMGs due to gas-depletion, we show that above a stellar mass of $M_* > 3 \times 10^{10}\,{\rm M}_\odot$, ∼30 per cent of all galaxies at $z \sim 1.8$–3.4 (the 16–84th percentile range of our sample) have gone through a sub-millimetre-luminous phase, rising to ∼100 per cent at $M_* \gtrsim 3 \times 10^{11}\,{\rm M}_\odot$. This is in good agreement with the predictions of simulations.

(x) We also show that the volume density of massive, gas-rich galaxies from our survey is $\sim 3 \times 10^{-4}\,{\rm Mpc}^{-3}$ for galaxies with $H_2$ masses of $\sim 10^{11}\,{\rm M}_\odot$ at $z \sim 2.6$ and that extrapolating to lower masses this broadly agrees with results from recent blind surveys for CO-emitters with ALMA and JVLA. Thus, panoramic sub-millimetre surveys provide an efficient route to identify and study the most massive gas-rich galaxies at high redshifts.

(xi) The contribution of 870 $\mu$m selected SMGs to the total star-formation rate density in the Universe increases steeply with redshift from $z \sim 1$, with the peak contribution being ∼15 per cent at $z \sim 3$ for the $S_{870} \geq 3.6$ mJy subsample and ∼60 per cent for SMGs brighter than $S_{870} = 1$ mJy. Thus, roughly half of the star-formation rate density at $z \sim 3$ arises in ULIRG-luminosity sources and the star formation contribution from this population appears to decline only slowly across the 1 Gyr from $z \sim 3$ to 6.

(xii) Finally, we investigate the scale of the rest-frame far-infrared emission in SMGs. We determine that the star-formation rate in the SMGs is significantly sub-Eddington, with a typical Eddington ratio of ∼0.1. We find that the far-infrared SEDs of SMGs are consistent with a modified blackbody model, which has an optical depth ($\tau$) of unity at $\lambda_0 \geq 100\,\mu$m, and the 870-$\mu$m sizes of SMGs are broadly consistent with them acting as a homologous population of centrally illuminated dust clouds.

Our analysis underlines the fundamental connection between the population of gas-rich, strongly star-forming galaxies at high redshifts, and the formation phase of the most massive galaxy populations over cosmic time. We suggest that the characteristics of these short-lived, but very active systems represent events where massive haloes (with characteristic total masses of $\sim 4 \times 10^{12}\,{\rm M}_\odot$) with high gas fractions transform their large gas reservoirs into stars on a few dynamical times. Analysis of the dust continuum morphologies of AS2UDS and ALMA observations of other SMG samples suggests that the continuum emission arises from bar-like structures with diameters of ∼2–3 kpc in more extended gas discs, which suggests that their strong evolution is likely driven by dynamical perturbations of marginally stable gas disks (Gullberg et al. 2019; Hodge et al. 2019).

## ACKNOWLEDGEMENTS

The authors thank the anonymous referee for their helpful and insightful comments, which have improved the paper. UD acknowledges the support of STFC studentship (ST/R504725/1). The Durham co-authors acknowledge support from STFC (ST/P000541/1). The authors thank John Helly and Lydia Heck for help with HPC. The ALMA data used in this paper were obtained under programs ADS/JAO.ALMA#2012.1.00090.S, #2015.1.01528.S, and #2016.1.00434.S. ALMA is a partnership of ESO (representing its member states), NSF (USA) and NINS (Japan), together with NRC (Canada) and NSC and ASIAA (Taiwan), in cooperation with the Republic of Chile. The Joint ALMA Observatory is operated by ESO, AUI/NRAO, and NAOJ. This work used the DiRAC@Durham facility managed by the Institute for Computational Cosmology on behalf of the STFC DiRAC HPC Facility (www.dirac.ac.uk). The equipment was funded by BEIS capital funding via STFC capital grants ST/K00042X/1, ST/P002293/1, ST/R002371/1, and ST/S002502/1, Durham University and STFC operations grant ST/R000832/1. DiRAC is part

of the National e-Infrastructure. We extend our gratitude to the staff at UKIRT for their tireless efforts in ensuring the success of the UKIDSS UDS project. EdC gratefully acknowledges the Australian Research Council as the recipient of a Future Fellowship (project FT150100079). JLW acknowledges support from an STFC Ernest Rutherford Fellowship (ST/P004784/1 and ST/P004784/2). All the data required for this project are available through the relevant archives.

## REFERENCES

Andrews B. H., Thompson T. A., 2011, ApJ, 727, 97
An F. X. et al., 2018, ApJ, 862, 101
Aravena M. et al., 2019, ApJ, 882, 136
Baes M., Verstappen J., De Looze I., Fritz J., Saftly W., Vidal Pérez E., Stalevski M., Valcke S., 2011, ApJS, 196, 22
Barger A. J., Cowie L. L., Sanders D. B., Fulton E., Taniguchi Y., Sato Y., Kawara K., Okuda H., 1998, Nature, 394, 248
Battisti A. J. et al., 2019, ApJ, 882, 61
Baugh C. M., Lacey C. G., Frenk C. S., Granato G. L., Silva L., Bressan A., Benson A. J., Cole S., 2005, MNRAS, 356, 1191
Behroozi P. S., Wechsler R. H., Conroy C., 2013, ApJ, 770, 57
Béthermin M., Dole H., Lagache G., Le Borgne D., Penin A., 2011, A&A, 529, A4
Biggs A. D. et al., 2011, MNRAS, 413, 2314
Blain A. W., Longair M. S., 1993, MNRAS, 264, 509
Blain A. W., Smail I., Ivison R. J., Kneib J.-P., Frayer D. T., 2002, Phys. Rep., 369, 111
Boselli A. et al., 2010, PASP, 122, 261
Bothwell M. S. et al., 2013, MNRAS, 429, 3047
Bourne N. et al., 2016, MNRAS, 462, 1714
Brisbin D. et al., 2017, A&A, 608, A15
Bruzual G., Charlot S., 2003, MNRAS, 344, 1000
Burgarella D., Nanni A., Hirashita H., Theule P., Inoue A. K., Takeuchi T. T., 2020, preprint (arXiv:2002.01858)
Calura F. et al., 2017, MNRAS, 465, 54
Calzetti D., Armus L., Bohlin R. C., Kinney A. L., Koornneef J., Storchi-Bergmann T., 2000, ApJ, 533, 682
Camps P. et al., 2018, ApJS, 234, 20
Camps P., Baes M., 2015, A&C, 9, 20
Casey C. M. et al., 2012, ApJ, 761, 140
Casey C. M., Narayanan D., Cooray A., 2014, Phys. Rep., 541, 45
Chabrier G., 2003, PASP, 115, 763
Chapman S. C., Blain A. W., Smail I., Ivison R. J., 2005, ApJ, 622, 772
Charlot S., Fall S. M., 2000, ApJ, 539, 718
Chen C.-C. et al., 2016, ApJ, 831, 91
Clemens M. S. et al., 2013, MNRAS, 433, 695
Clements D. L. et al., 2008, MNRAS, 387, 247
Clements D. L. et al., 2018, MNRAS, 475, 2097
Condon J. J., 1992, ARA&A, 30, 575
Coppin K. E. K. et al., 2009, MNRAS, 395, 1905
Cowie L. L., González-López J., Barger A. J., Bauer F. E., Hsu L.-Y., Wang W.-H., 2018, ApJ, 865, 106
Crain R. A. et al., 2015, MNRAS, 450, 1937
da Cunha E. et al., 2015, ApJ, 806, 110
da Cunha E., Charlot S., Elbaz D., 2008, MNRAS, 388, 1595
Daddi E. et al., 2007, ApJ, 670, 156
Daddi E., Cimatti A., Renzini A., Fontana A., Mignoli M., Pozzetti L., Tozzi P., Zamorani G., 2004, ApJ, 617, 746
Danielson A. L. R. et al., 2011, MNRAS, 410, 1687
Danielson A. L. R. et al., 2017, ApJ, 840, 78
Davé R., Finlator K., Oppenheimer B. D., Fardal M., Katz N., Kereš D., Weinberg D. H., 2010, MNRAS, 404, 1355
Decarli R. et al., 2016, ApJ, 833, 70
Decarli R. et al., 2019, ApJ, 882, 138
Donley J. L. et al., 2012, ApJ, 748, 142
Draine B. T., 2009, in Henning T., Grün E., Steinacker J., eds, ASP Conf. Ser. Vol. 414, Cosmic Dust – Near and Far. Astron. Soc. Pac., San Francisco, p. 453
Driver S. P. et al., 2018, MNRAS, 475, 2891
Dunlop J. S. et al., 2017, MNRAS, 466, 861
Dunlop J. S., 2011, in Wang W., Lu J., Luo Z., Yang Z., Hua H., Chen Z., eds, ASP Conf. Ser. Vol. 446, Galaxy Evolution: Infrared to Millimeter Wavelength Perspective. Astron. Soc. Pac., San Francisco, p. 209
Dunne L. et al., 2011, MNRAS, 417, 1510
Eales S., Lilly S., Gear W., Dunne L., Bond J. R., Hammer F., Le Fèvre O., Crampton D., 1999, ApJ, 515, 518
Farrah D. et al., 2006, ApJ, 641, L17
Farrah D. et al., 2008, ApJ, 677, 957
Franceschini A., Toffolatti L., Mazzei P., Danese L., de Zotti G., 1991, A&AS, 89, 285
Franco M. et al., 2018, A&A, 620, A152
Frayer D. T., Ivison R. J., Scoville N. Z., Yun M., Evans A. S., Smail I., Blain A. W., Kneib J.-P., 1998, ApJ, 506, L7
Geach J. E. et al., 2017, MNRAS, 465, 1789
Geach J. E., Smail I., Moran S. M., MacArthur L. A., Lagos C. del P., Edge A. C., 2011, ApJ, 730, L19
Gerhard O., Kronawitter A., Saglia R. P., Bender R., 2001, AJ, 121, 1936
Greve T. R. et al., 2005, MNRAS, 359, 1165
Gruppioni C. et al., 2013, MNRAS, 432, 23
Gruppioni C., Pozzi F., 2019, MNRAS, 483, 1993
Gullberg B. et al., 2019, MNRAS, 490, 4956
Hainline L. J., Blain A. W., Smail I., Alexand er D. M., Armus L., Chapman S. C., Ivison R. J., 2011, ApJ, 740, 96
Harwit M., Pacini F., 1975, ApJ, 200, L127
Hatsukade B. et al., 2016, PASJ, 68, 36
Hatsukade B. et al., 2018, PASJ, 70, 105
Hayward C. C., Kereš D., Jonsson P., Narayanan D., Cox T. J., Hernquist L., 2011, ApJ, 743, 159
Helou G., Soifer B. T., Rowan-Robinson M., 1985, ApJ, 298, L7
Hickox R. C. et al., 2012, MNRAS, 421, 284
Hodge J. A. et al., 2013, ApJ, 768, 91
Hodge J. A. et al., 2016, ApJ, 833, 103
Hodge J. A. et al., 2019, ApJ, 876, 130
Hughes D. H. et al., 1998, Nature, 394, 241
Ikarashi S. et al., 2011, MNRAS, 415, 3081
Ikarashi S. et al., 2015, ApJ, 810, 133
Ikarashi S. et al., 2017, ApJ, 849, L36
Iono D. et al., 2009, ApJ, 695, 1537
Ivison R. J. et al., 2002, MNRAS, 337, 1
Ivison R. J. et al., 2007, MNRAS, 380, 199
Ivison R. J. et al., 2010, MNRAS, 402, 245
Ivison R. J., Smail I., Le Borgne J.-F., Blain A. W., Kneib J.-P., Bezecourt J., Kerr T. H., Davies J. K., 1998, MNRAS, 298, 583
Karim A. et al., 2013, MNRAS, 432, 2
Kawinwanichakij L. et al., 2020,ApJ, 892, 7
Kennicutt Robert C. J., 1998, ARA&A, 36, 189
Lagos C. D. P., Baugh C. M., Lacey C. G., Benson A. J., Kim H.-S., Power C., 2011, MNRAS, 418, 1649
Laigle C. et al., 2016, ApJS, 224, 24
Lang P. et al., 2019, ApJ, 879, 54
Lawrence A. et al., 2007, MNRAS, 379, 1599
Lee S.-K., Ferguson H. C., Somerville R. S., Wiklind T., Giavalisco M., 2010, ApJ, 725, 1644
Liang L., Feldmann R., Faucher-Giguère C.-A., Kereš D., Hopkins P. F., Hayward C. C., Quataert E., Scoville N. Z., 2018, MNRAS, 478, L83
Lilly S. J., Eales S. A., Gear W. K. P., Hammer F., Le Fèvre O., Crampton D., Bond J. R., Dunne L., 1999, ApJ, 518, 641
Lindner R. R. et al., 2011, ApJ, 737, 83
McAlpine S. et al., 2019, MNRAS, 2440, 488
Madau P., 1995, ApJ, 441, 18
Madau P., Dickinson M., 2014, ARA&A, 52, 415
Magnelli B. et al., 2010, A&A, 518, L28

Magnelli B. et al., 2012, A&A, 539, A155
Magnelli B. et al., 2013, A&A, 553, A132
Menéndez-Delmestre K. et al., 2009, ApJ, 699, 667
Menéndez-Delmestre K., Blain A. W., Swinbank M., Smail I., Ivison R. J., Chapman S. C., Gonçalves T. S., 2013, ApJ, 767, 151
Miettinen O. et al., 2017, A&A, 606, A17
Muñoz Arancibia A. M. et al., 2018, A&A, 620, A125
Narayanan D. et al., 2015, Nature, 525, 496
Oliver S. J. et al., 2012, MNRAS, 424, 1614
Overzier R. A., Röttgering H. J. A., Rengelink R. B., Wilman R. J., 2003, A&A, 405, 53
Pettini M., Rix S. A., Steidel C. C., Adelberger K. L., Hunt M. P., Shapley A. E., 2002, ApJ, 569, 742
Planck Collaboration XIX, 2011, A&A, 536, A19
Pope A. et al., 2006, MNRAS, 370, 1185
Pope A. et al., 2008, ApJ, 689, 127
Puget J.-L., Abergel A., Bernard J.-P., Boulanger F., Burton W. B., Desert F.-X., Hartmann D., 1996, A&A, 308, L5
Riechers D. A. et al., 2013, Nature, 496, 329
Riechers D. A. et al., 2019, ApJ, 872, 7
Roseboom I. G. et al., 2012, MNRAS, 419, 2758
Ross N. P. et al., 2009, ApJ, 697, 1634
Sanders D. B., Mirabel I. F., 1996, ARA&A, 34, 749
Sanders D. B., Soifer B. T., Elias J. H., Neugebauer G., Matthews K., 1988, ApJ, 328, L35
Schaye J. et al., 2015, MNRAS, 446, 521
Schechter P., 1976, ApJ, 203, 297
Scoville N. et al., 2014, ApJ, 783, 84
Scoville N. Z., 2013, in Falcon-Barroso J., Knapen J. H., eds, Secular evolution of galaxies. Cambridge University Press, Cambridge, UK, p. 491
Simpson C., Westoby P., Arumugam V., Ivison R., Hartley W., Almaini O., 2013, MNRAS, 433, 2647
Simpson J. M. et al., 2012, MNRAS, 426, 3201
Simpson J. M. et al., 2014, ApJ, 788, 125
Simpson J. M. et al., 2015a, ApJ, 799, 81
Simpson J. M. et al., 2015b, ApJ, 807, 128
Simpson J. M. et al., 2017, ApJ, 839, 58
Smail I., Ivison R. J., Blain A. W., 1997, ApJ, 490, L5
Smail I., Ivison R. J., Kneib J. P., Cowie L. L., Blain A. W., Barger A. J., Owen F. N., Morrison G., 1999, MNRAS, 308, 1061
Smail I., Chapman S. C., Blain A. W., Ivison R. J., 2004, ApJ, 616, 71
Smail I., Sharp R., Swinbank A. M., Akiyama M., Ueda Y., Foucaud S., Almaini O., Croom S., 2008, MNRAS, 389, 407
Smith D. J. B. et al., 2013, MNRAS, 436, 2435
Springel V. et al., 2005, Nature, 435, 629
Stach S. M. et al., 2018, ApJ, 860, 161
Stach S. M. et al., 2019, MNRAS, 487, 4648
Strandet M. L. et al., 2016, ApJ, 822, 80
Swinbank A. M. et al., 2011, ApJ, 742, 11
Swinbank A. M. et al., 2012, MNRAS, 427, 1066
Swinbank A. M. et al., 2014, MNRAS, 438, 1267
Swinbank A. M., Chapman S. C., Smail I., Lindner C., Borys C., Blain A. W., Ivison R. J., Lewis G. F., 2006, MNRAS, 371, 465
Symeonidis M. et al., 2013, MNRAS, 431, 2317
Symeonidis M., Page M. J., Seymour N., 2011, MNRAS, 411, 983
Tacconi L. J. et al., 2018, ApJ, 853, 179
Tasca L. A. M. et al., 2015, A&A, 581, A54
Toft S. et al., 2014, ApJ, 782, 68
Umehata H. et al., 2018, PASJ, 70, 65
van der Kruit P. C., 1971, A&A, 15, 110
van der Kruit P. C., 1973, A&A, 29, 263
Vlahakis C., Dunne L., Eales S., 2005, MNRAS, 364, 1253
Vlahakis C., Eales S., Dunne L., 2007, MNRAS, 379, 1042
Wall J. V., Pope A., Scott D., 2008, MNRAS, 383, 435
Walter F. et al., 2016, ApJ, 833, 67
Wang S. X. et al., 2013, ApJ, 778, 179
Wardlow J. L. et al., 2011, MNRAS, 415, 1479
Weiß A. et al., 2009, ApJ, 707, 1201
Weiß A. et al., 2013, ApJ, 767, 88
Whitaker K. E., Kriek M., van Dokkum P. G., Bezanson R., Brammer G., Franx M., Labbé I., 2012, ApJ, 745, 179
White S. D. M., Rees M. J., 1978, MNRAS, 183, 341
Wilkinson A. et al., 2017, MNRAS, 464, 1380
Wilson C. D., Rangwala N., Glenn J., Maloney P. R., Spinoglio L., Pereira-Santaella M., 2014, ApJ, 789, L36
Yun M. S., Reddy N. A., Condon J. J., 2001, ApJ, 554, 803
Zehavi I. et al., 2011, ApJ, 736, 59
Zhang Z.-Y., Romano D., Ivison R. J., Papadopoulos P. P., Matteucci F., 2018, Nature, 558, 260
Zhukovska S., Henning T., Dobbs C., 2018, ApJ, 857, 94

## SUPPORTING INFORMATION

Supplementary data are available at *MNRAS* online.

**Table A1.** The AS2UDS catalogue containing the results for all 707 SMGs from this study. The catalogue includes all of the photometry used to fit the SEDs and the MAGPHYS outputs for each of the sources. This includes photometric redshift, stellar mass, star-formation rate, *V*-band dust attenuation, mass-weighted age, far-infrared luminosity, dust mass, modified blackbody temperatures, and their associated uncertainties (16–84th percentile range values).
**Fig. A1.** Figure showing the observed photometry and best-fitting MAGPHYS model SEDs for all 707 ALMA SMGs.
**Fig. A2.** Figure showing the results of a MAGPHYS analysis on EAGLE simulated galaxies, specifically stellar mass, star-formation rate, dust mass, dust temperature, and mass-weighted age.

Please note: Oxford University Press is not responsible for the content or functionality of any supporting materials supplied by the authors. Any queries (other than missing material) should be directed to the corresponding author for this paper.

[1]*Centre for Extragalactic Astronomy, Department of Physics, Durham University, South Road, Durham DH1 3LE, UK*
[2]*School of Physics and Astronomy, University of Nottingham, University Park, Nottingham NG7 2RD, UK*
[3]*International Centre for Radio Astronomy Research, University of Western Australia, 35 Stirling Hwy, Crawley, WA 6009, Australia*
[4]*Research School of Astronomy and Astrophysics, The Australian National University, Canberra, ACT 2611, Australia*
[5]*ARC Centre of Excellence for All Sky Astrophysics in 3 Dimensions (ASTRO 3D), Canberra, ACT2601, Australia*
[6]*Department of Physics and Astronomy, University of the Western Cape, Robert Sobukwe Road, Bellville 7535, South Africa*
[7]*Institut de Radioastronomie Millimétrique, 300 rue de la Piscine, Domaine Universitaire, F-38406 Saint Martin d'Hères, France*
[8]*Department of Physics and Astronomy, University of Leicester,University Road, Leicester LE1 7RH, UK*
[9]*Department of Physics and Atmospheric Science, Dalhousie University Halifax, Halifax, NS B3H 3J5, Canada*
[10]*European Southern Observatory, Karl Schwarzschild Strasse 2, D-85748 Garching, Germany*
[11]*Centre for Astrophysics Research, School of Physics, Astronomy and Mathematics, University of Hertfordshire, Hatfield AL10 9AB, UK*
[12]*Institute for Astronomy, University of Edinburgh, Royal Observatory, Blackford Hill, Edinburgh EH9 3HJ, UK*
[13]*Department of Physics and Astronomy, University of Hawaii, 2505 Correa Road, Honolulu, HI 96822, USA*
[14]*Institute for Astronomy, 2680 Woodlawn Drive, University of Hawaii, Honolulu, HI 96822, USA*

[15]*Department of Physics and Astronomy, University College London, Gower Street, London WC1E 6BT, UK*
[16]*Leiden Observatory, Leiden University, P.O. box 9513, NL-2300 RA Leiden, the Netherlands*
[17]*Department of Physics and Astronomy, University of British Columbia, 6224 Agricultural Road, Vancouver, BC V6T 1Z1, Canada*
[18]*Gemini Observatory, Hilo, HI 96720, USA*
[19]*The University of Manchester, Oxford Road, Manchester, M13 9PL, UK*
[20]*Max-Planck-Institut für Astronomy, Königstuhl 17, D-69117 Heidelberg, Germany*
[21]*Department of Physics, Lancaster University, Lancaster LA1 4YB, UK*
[22]*Max-Planck-Institut für Radioastronomie, Auf dem Hügel 69, D-53121 Bonn, Germany*

This paper has been typeset from a TEX/LATEX file prepared by the author.